SAPIENZA
UNIVERSITÀ DI ROMA

Faculty of Engineering
Department of Structural and Geotechnical engineering
Sapienza University of Rome

A thesis presented for the degree of
Doctor of Philosophy

Improvement of seismic isolation performances via negative stiffness and super-elastic hysteresis based damping

PhD Candidate: Andrea Salvatore

PhD Coordinator: Prof. Patrizia Trovalusci

...Alla mia famiglia e ad Agnese,
indispensabili sorgenti di forza e ispirazione

Abstract

Among the passive vibration control strategies, base isolation is definitely the most effective. This strategy consists in decoupling the motion of the structure from that of the substructure/soil by introducing a layer of highly flexible elements between them. The high flexibility of the isolation layer interposed between the foundation and the structure causes an increase of the modal periods of the latter, which produces a dual effect: a strong reduction of the accelerations transmissibility and an increase of the displacement transmissibility. The last effect is usually contrasted by the introduction of auxiliary damping devices. A recently explored concept is the amplification of the damping of a structure by the parallel application of negative stiffness devices, i.e., devices that exert a force in the same direction of displacement. The main advantages that a negative stiffness mechanism can provide to a seismic isolation system are the possibility of reaching levels of flexibility of the isolation layer over the limit represented by the deformability of the material of the bearing devices, i.e. the possibility of obtaining acceleration transmissibility reductions otherwise not achievable with the existing devices and the opportunities to introduce high levels of hysteretic damping without performance losses caused by the initial stiffness increase, since this increase is cancelled by the negative stiffness properly tuned. In the light of the above, the intention is to exploit the characteristics of bistable mechanisms together with super-elastic hysteresis to obtain an ideal seismic isolation system, with high static stiffness, low dynamic stiffnesses and self-recentering capabilities. The research objectives are, therefore, the study of the effects and limits of applying mechanisms with negative stiffness and super-elastic hysteresis to seismic isolated systems and the design of a new multidirectional and compact damper with negative stiffness and super-elastic hysteresis. The performance of the proposed isolation system has been evaluated by studying the response of a one-degree-of-freedom oscillator having as restoring force the sum of the contributions given by the elastomeric isolators, the bistable mechanism and the super-elastic hysteresis, described by appropriate hysteretic models. The investigation first involved the static characterization of the response of the dimensionless system in terms of stability, stiffness and equivalent damping, highlighting the presence of different types of stability in the space of the design parameters and the possibility of obtaining almost zero stiffness together with amplifications of the damping up to overdamped responses. The second phase of the investigation involved the dynamic response under impulsive and harmonic excitation and the search in the space of the design parameters of the optimal configurations in terms of reduction of the forces transmissibility, revealing the possibility of obtaining strong

improvements of the seismic isolation performances. These regions of optimal design parameters have been validated through the study of the dynamic response of a MDOF system, representative of a seismic isolated building, under seismic forcing. Finally, the performances obtained by NS-SMA damping are compared with the ones exhibited by the baseline isolation system equipped with classic auxiliary damping devices. The last phase of the study was dedicated to the development of a rheological device which would allow to achieve the dynamic response of the proposed isolation system . Starting from the main weaknesses of the existing negative stiffness dampers, i.e. the large size given by the prestressed element, the monodirectional response or the dependence of the response on the weight of the mass to be isolated, a new compact multidirectional damper with super-elastic hysteresis has been designed. Finally, the analytical equations of the force-displacement law of the device were derived and validated by comparison with the response provided by a three-dimensional numerical model developed on the software Abaqus.

Contents

Chapter 1

Introduction

1.1 Seismic isolation

Base isolation is a seismic demand reduction technique consisting of decoupling the motion of the structure from that of the substructure/soil by introducing a layer of highly flexible elements between them. The most used seismic isolation devices are:

- Elastomeric bearings: without lead core (Low and High Damping Rubber Bearing LDRB, HDRB) and with lead core (Lead Rubber Bearing LRB). While the first ones allow a lower stiffness and therefore a higher reduction of the accelerations, the second ones allow, through the hysteresis of the lead core, a higher damping.

- Sliding bearings: with flat or concave sliding surface (FSS or CSS, respectively). The former allow almost zero stiffness post-activation and therefore great reductions in input accelerations. On the other hand, these devices exhibit almost zero re-centring capacity. This aspect is partly solved in devices with a curved surface, where the curvature of the sliding surface causes that the normal force acting on it produces a horizontal restoring force inversely proportional to the radius of curvature of the surface.

In Tab.1.1 advantages and disadvantages of most common isolation bearing devices are summarised. The high flexibility of the the isolator layer interposed between the foundation and the structure causes an increase of the modal periods of the latter, which produces a dual effect:

- strong reduction of the transmissibility in terms of accelerations;

- increase of the transmissibility in terms of displacement.

The last effect is usually contrasted by the introduction of auxiliary damping devices. Several studies in the literature show the effects of damping in seismic isolation and different methods to optimize this contribution. In general, there exists an optimum damping point that can be introduced, beyond which, there is an increase in transmissibility in accelerations, due to the stiffening effect of damping, and thus a loss of performance from the motion decoupling point of view [1]-[29].

Bearing devices	Advantages	Disadvantages
LDRB	Cost effective, self re-centering, low stiffness	Low damping capacities (5-10%)
HDRB	Self re-centering, low stiffness, discrete damping (10-15%)	Aging effect, expensive
LRB	High damping capacities (30-45%)	Residual displacements, high initial stiffness
FSS	Very high damping capacities (60%), very low stiffness	Zero re-centering capacity, friction could cause inactivation and increase of transmissibility for high frequencies
CSS	High damping capacities (20-30%), low stiffness	Residual displacements, friction could cause inactivation and increase of transmissibility for high frequencies

Table 1.1: Advantages and disadvantages of most common isolation bearing devices.

1.1.1 Damping techniques and devices in seismic isolation

There are different damping techniques and systems that can be grouped into three macro-families depending on the type of operating principle:

- Dependent on velocity (VD): All devices that exploit a viscous type of damping (viscoelastic materials, viscous fluids). The advantages of such systems are the recentering capability and the no plasticization of internal parts, the disadvantages are the high cost and the dependence of the response on the velocity and therefore on the frequency content of the seismic event. This problem is usually solved by using devices with non-linear viscous damping (Fluid-Viscous Damper) which can exhibit a more homogeneous response as function of the velocity of the load.

- Dependent on the sign of the velocity (FRD): All devices that dissipate through friction between components. The main advantage of this type of device is the possibility to set a maximum force limit thanks to a rigid-plastic response. On the other hand, the high pre-slip stiffness, exhibited by

the mechanism at the moment of activation and at each inversion of the sign of the speed in the cyclic response, may lead to an amplification of the accelerations within the structure. Another problem, of technological nature, is the potential oxidation over time of the sliding parts, which results in an increase in friction and consequent inactivation of the sliding mechanism.

- Dependent on displacement (HYD, SMAD): All devices that dissipate through hysteretic damping i. e. through the plasticization of ductile elements. The advantages of these systems are their low cost and the high damping capability, while the main disadvantages are the presence of residual displacement and high initial pre-plasticization stiffness. In particular, the latter produces an increase in the transmissibility of accelerations in the low-amplitude displacement range and a consequent loss of performance for smaller and more frequent seismic events. Residual displacement can be cancelled using elements exhibiting super-elastic hysteresis, such as Shape Memory Alloy spring.

Another technique used for displacement reduction in base isolated systems is the use of a Tuned Mass Damper (TMD) on the ground floor of the building. This device is promising in reducing both the displacements and the maximum accelerations of the structure. In Tab.1.2 advantages and disadvantages of the described damping techniques are summarised.

Damping techniques	Advantages	Disadvantages
VD	Self-recentering	Damping function of the velocity, increase of transmissibility for high frequencies
HYD	Stable damping	Residual displacements, high initial stiffness
SMAD	Self-recentering, stable damping	High initial stiffness
FRD	Cost effective, stable damping	Residual displacements, high initial stiffness, increase of transmissibility for high frequencies
TMD	High damping capacities	First impulse not well governed

Table 1.2: Advantages and disadvantages of classic damping techniques.

Recent developments of research on vibration absorption devices are:

- The Inerter: this device allows the amplification of the control force provided by the secondary mass through the flywheel effect provided by a gear

mechanism. This results in a greater inertial mass with the same gravitational mass and therefore a strong reduction in the mass required for optimal control.

- Non-linear Energy Sink (NES): This device exploits the cubic stiffness, which cannot be linearised, and the high initial deformability in order to achieve a larger activation frequency band. The device is used, unlike the TMD, not to provide a control force opposite to the motion of the structure, but to dissipate energy through the motion of the secondary mass, which must be therefore the most excitable possible.

For all the devices that exploit the contribution of a secondary mass, the phasing of the secondary mass delays the activation of the device, thus allowing the first seismic waves to reach the structure. This phenomenon, especially in the presence of near-fault seismic events, where the first waves have the highest energy content, can lead to a reduction in the performance of the isolation system [30]-[49]]. In order to obtain a recentering and dissipative system, research has recently turned towards mechanisms that can produce Flag-Shape hysteretic cycles. This type of hysteretic behaviour is usually achieved through the parallel application of a bilinear elastic system to an elastoplastic one. Another way to achieve these hysteretic cycles is through the use of shape memory alloys (SMA). These alloys, most commonly made of Nickel and Titanium in approximately equal parts (NiTiNol), exhibit superelastic hysteresis, i.e. with deformation recovery, thanks to the austenitic-martensitic phase transformation of the alloy. There are several examples in the literature of the application of devices based on shape memory alloys in parallel with seismic isolation systems. In all these examples, as well as in all cases where hysteretic damping is employed, there is, due to the parallel addition of the damping element, an increase in initial stiffness, which leads to a loss of isolation performance, especially for low intensity earthquakes [50]-[71].

1.1.2 Negative stiffness

A recently explored concept is the amplification of the damping of a structure by the parallel application of negative stiffness devices, i.e., devices that exert a force in the same direction of displacement [72]-[81]. A necessary condition for the existence of negative stiffness response branches is the negativity of the second derivative of the potential energy of the mechanism, i.e. the existence of an unstable equilibrium position. Mechanisms known in the literature that exhibit negative stiffness are bistable mechanisms. These are deformable mechanisms, whose response is therefore governed by geometric non-linearities, which exhibit an unstable equilibrium position enclosed between two stable equilibrium positions. The best known example of this type of mechanism is the Von Mises truss.

This structure exhibits the characteristic snap-through response of bistable mechanisms, namely a transition between the two stable equilibrium positions that occurs through a negative stiffness response. Assuming to place this mechanism in the unstable position, it will manifest a nonlinear behaviour well approximated by a negative stiffness duffing oscillator, that is a negative linear stiffness in parallel with a positive cubic stiffness. These mechanisms, when applied in parallel to a structure, produce a double effect:

- Reduction of the stiffness and therefore of the accelerations and loads induced in the system;
- Amplification of the equivalent damping achieved through the reduction of stiffness with the same damping element.

A wide range of applications for bistable mechanisms has been proposed in recent years, in the fields of energy harvesting, vibration control, dynamic monitoring and actuation device. Most of the bistable mechanisms developed today are based on the use of pre-stressed (springs) or pre-buckled (beam) deformable elements. Other ways to achieve negative stiffness responses can be the use of reverse curvature sliding surfaces or magnetorheological devices with linear voltage decay [82]- [88].

1.2 State of art of QZS isolation

One of the first examples of the application of negative stiffness mechanisms in structural control are the works of Reinhorn, Pasala, Nagarajaiah et al. [89]-[97], where a mechanism with negative stiffness plus an initial activation gap is introduced in parallel to a structure to produce an apparent plasticization of this one. In particular, a bilinear spring is used in parallel with negative stiffness element to achieve an initial gap in the restoring force of the device. The structure, for low amplitudes, reacts with its stiffness thanks to the presence of the initial gap. For larger amplitudes, negative stiffness is involved, thus emulating the plasticization of the structure, i.e. a reduction in stiffness and therefore in the input loads, without any real structural damage. There are several developments of this concept applied to seismic isolation that show promising results in terms of reduction of both accelerations and displacements transmissibilities [98, 99]. In [100]-[120] a linear vertical isolation system was enhanced by introducing a negative stiffness correction to obtain a high preload stiffness and a Quasi-Zero-Stiffness (QZS) in the equilibrium position.
The nonlinear isolator response is usually described by a Duffing oscillator with a vanishing linear stiffness. Donmez et al. [121] studied the dynamic response of

a dry-friction QZS isolator, showing that the hysteretic damping ensures a better performance than viscous damping in the out-of-resonance frequency range. In all of these works, negative stiffness correction is used to achieve zero stiffness in the equilibrium position, but as known, in typical civil applications dealing with seismic horizontal isolation, this is undesirable because of the need of a wind restraint. By delaying the negative stiffness contribution through an initial gap, the wind restraint is preserved, and transmissibility reduction can be achieved.
Liu et al. [122] proposed a novel isolation system composed by Shape Memory Alloy (SMA) wires providing the superelastic effect and a prestressed spring. The stiffness of the SMA wires overcomes the negative stiffness exhibited by the prestressed spring until phase transformations occur. For larger displacements, the stiffness of SMA wires vanishes and the overall stiffness becomes quasi zero. The transmissibility of a SDOF with the proposed response was analytically evaluated using a piece-wise linear constitutive law for the SMA response and a linear elastic law for the negative stiffness contribution.

1.3 State of art of negative stiffness damper

The state of the art for mechanical devices with negative stiffness is the result of progress over the last three decades. In 1992, Platus studied and patented several negative-stiffness mechanisms [123] made by assembling pre-compressed springs and pre-buckled beam in the context of vibration isolation of small masses (machinery, telescopes, etc.). Subsequently, a large development of these devices has been observed, and they can be divided into two macro-families. The first macro-family includes all the devices that develop negative stiffness through the introduction of two pre-compressed springs orthogonal to the controlled direction. If the springs deviate from this direction, they will exert a force in the same direction as the displacement, due to their pre-compression. Examples of such a mechanism are the device proposed by Avshalom Suissa [124] in 2013 for improving the performance of vehicle suspensions and the device presented by Zhou Peng [125] in 2017 for controlling cable vibrations. In particular, in the latter device, the structure composed of the pre-compressed spring pair, responsible for the negative stiffness elastic contribution, is coupled to a viscous or hysteretic damping device. A further development was proposed in 2020 by Yuhong [126], who placed, in parallel to the pair of pre-compressed springs, shape memory alloy wires to exploit their superelastic hysteresis. Another application close to this macro-family of devices is the damper proposed by Constantinou in 2013 [127]. This device is the first negative stiffness damper designed for vibration control on a civil scale. A common limitation of these applications is the device's monodirectionality, i.e. the ability to exert the desired rheological behaviour in just one

direction. The second macro-family of mechanical dampers with negative stiffness is composed of all those devices that exploit the reverse curvature of two surfaces, which are compressed together and relatively sliding. Examples of this type of damper are the devices proposed by Sanxiu in 2006 [128] and by Iemura in 2013 [129], where the compression between the two spherical caps is provided by the weight of the mass to isolate, for which the damper acts as an auxiliary support. The main advantage of this application is the multi-directionality of the mechanism, while the limitation is the dependence of the device response, both in terms of stiffness and damping, from the weight of the structure to be controlled. This dependence, together with a difficulty in the design of the device, also results in a sensitivity of the global response to vertical accelerations, which, modifying the weight force acting on the caps, consequently modify in a random way the response of the device. Other limiting aspects of the above-mentioned devices are the absence of a tunable auxiliary damping body and of a stiffening for large displacements (beneficial in order to slow down the mass in correspondence of the last allowed displacement). These last two aspects are solved by the device proposed by Cao Sa Sa in 2019 [130], where shape memory alloy wires are inserted between the two caps in vertical configuration in order to limit large displacements. On the other hand, the dependence of the response on the weight of the structure persists.

1.4 Objectives

The main advantages that a negative stiffness mechanism can provide to a seismic isolation system are:

- The possibility of reaching levels of flexibility of the isolation layer over the limit represented by the deformability of the material of the bearing devices, i.e. the possibility of obtaining acceleration transmissibility reductions otherwise not achievable with the existing devices;
- The possibility to introduce high levels of hysteretic damping without performance losses caused by the initial stiffness increase, since this increase is cancelled by the negative stiffness properly tuned.

In the light of the above, the intention is to exploit the characteristics of bistable mechanisms to obtain an ideal isolation system, which meets the following requirements:

- High static stiffness that prevents excessive deformations for low excitations and at the same time realizes a wind restraint,

- Low dynamic stiffness to reduce accelerations,
- High end run stiffness to slow down the building and thus prevent the pounding phenomenon
- Self recentering capability against residual displacements that can be detrimental particularly in case of aftershock events.

The proposal is to obtain this response by introducing in parallel to the most economic isolation system, the elastomeric one, a damping system based on negative stiffness (provided by bistable mechanisms) and superelastic hysteresis provided by shape memory alloy elements. The research objectives are:

- The study of the effects and of the limits of the application of bistable mechanisms to seismically isolated systems;
- The optimization of the negative stiffness and of the superelastic hysteresis in order to achieve the best performance in terms of transmissibility and dynamic stability;
- The design and the optimization of a new multidirectional damper with negative stiffness and superelastic hysteresis.

Chapter 2

Negative stiffness-SMA damper for seismic isolation

In previous works, a bilinear spring is used in parallel with the negative stiffness in order to achieve an initial gap in the ensuing restoring force of the device. This gap allows to maintain the virgin isolation stiffness for low amplitudes and to realize a wind restraint. In this work, a superelastic spring is used instead of the bilinear spring in order to realize the initial gap and, at the same time, to deliver hysteretic damping to the system. The total restoring force f of the proposed isolation system is the summation of the force f_i provided by traditional seismic elastomeric isolators, the superelastic force f_s and the force f_n provided by the negative stiffness mechanism. It reads

$$f = f_i + (f_n + f_s) = f_i + f_{ns}, \tag{2.1}$$

where $f_{ns} = f_n + f_s$ is the overall force of the proposed rheological device. For displacements below the gap amplitude, the stiffness of the superelastic element is equal to the negative stiffness, hence the response is governed by the elastomeric element. For displacements larger than the gap, corresponding to the superelastic transition (i.e., where the stiffness drops), the negative stiffness strongly reduces the total force and stiffness. For larger displacements, the cubic term tends to overcome the negative stiffness contribution and the overall response returns to follow the baseline backbone response of the elastomeric bearings (see Fig. 2.1). In the subsequent sections, 3 types of isolated SDOF systems are studied and compared. The baseline elastomeric isolation system (EIS) is referred to as S_1 and the associated restoring force is $f = f_i$. S_2 denotes the baseline isolation system together with the superelastic spring alone whose associated restoring force is $f = f_i + f_s$. Finally, S_3 indicates the compound isolation system constituted by the NS-SMA damper arranged in parallel with the elastomeric bearings and the associated total restoring force is $f = f_i + f_s + f_n$ (see Fig. 2.2).

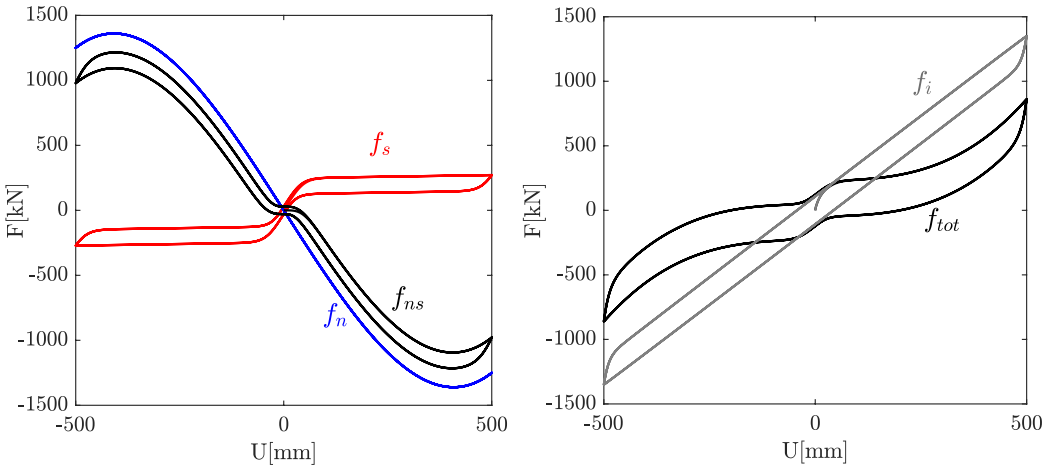

Figure 2.1: Force-displacement cycles associated with (left) damper force f_{ns} (black line) ensuing from f_s (red line indicating the superelastic element) plus f_n (blue line indicating the negative stiffness element) and with (right) the overall system response with and without damper (black and gray lines, respectively).

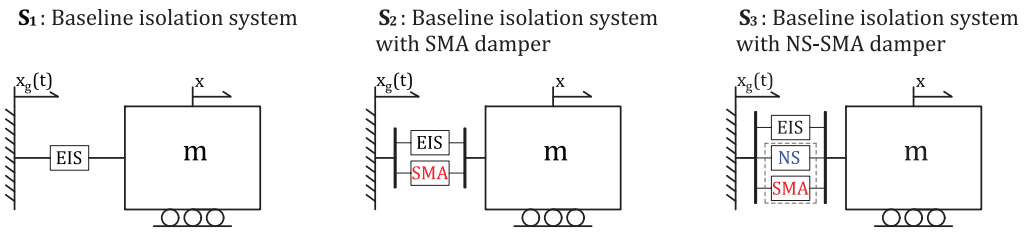

Figure 2.2: Schematic representation of the 3 different isolated systems referred to as S_1, S_2 and S_3, respectively.

2.1 Rheological models

2.1.1 Elastomeric isolators

Elastomeric isolation systems are usually described by the Bouc-Wen model of hysteresis [131, 132] together with a linear viscous damping term. Therefore, the adopted model is the direct summation of a viscous damping force, an elastic force and a hysteretic force,

$$f_i = c\dot{x} + \alpha K_i x + (1-\alpha)K_i z, \tag{2.2}$$

where the hysteretic force z is governed by

$$\dot{z} = \dot{x}[1-(\gamma+\beta\,\mathrm{sign}(z\dot{x})]|z|^n. \tag{2.3}$$

The term c is the viscous damping coefficient, α is the ratio between the post-elastic and the stiffness K_i at the origin, γ and β control the shape of the hysteresis loops, n regulates the smoothness of transition between the initial elastic and post-elastic stiffness. The upper and lower bounds of z are given by $z_m = \pm\sqrt[n]{(1-\alpha)K_i/(\gamma+\beta)}$. In the present study, $\gamma+\beta$ is restricted to be positive in order to have a softening behaviour and n is set to 1 (Fig. 2.3).

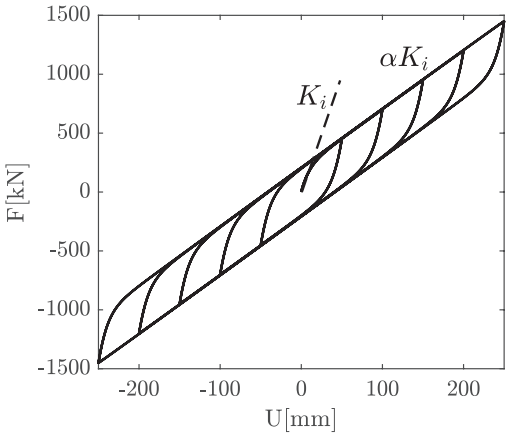

Isolation system parameters

K_i	Initial stiffness
α	0.2
γ	0.01
β	0.09
n	1
c	0.1

Figure 2.3: Force-displacement cycles of isolation devices where K_i indicates the stiffness at the origin and αK_i denotes the post-elastic stiffness.

2.1.2 Negative stiffness mechanism

In most passive bi-stable mechanisms, the negative stiffness is produced by geometric nonlinearities within a given displacement range while out of this, the stiffness returns to be positive. In this work, the force exhibited over the displacement amplitude x_f, for which the force vanishes, is cancelled by means of a step function. Its expression reads

$$f_n = (-K_n x + K_3 x^3)\frac{(1+\text{sign}(x_f - |x|))}{2} \tag{2.4}$$

where K_n is the negative linear stiffness, K_3 is the positive cubic stiffness, and x_f is the displacement corresponding to a vanishing force and is equal to $x_f = \sqrt{K_n/K_3}$. Another characteristic displacement is that leading to the maximum negative force and is given by $x_n = \sqrt{K_n/3K_3}$ (see Fig. 2.4).

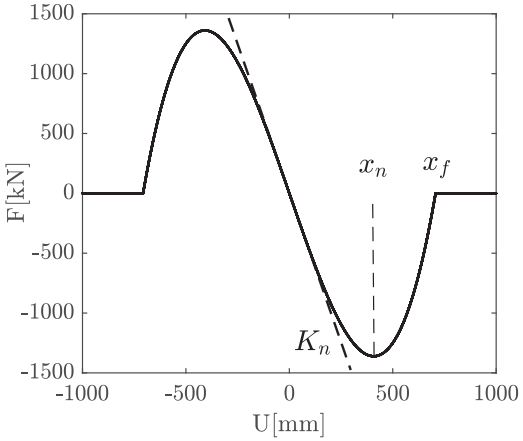

Negative stiffness parameters	
K_n	Negative stiffness
x_f	Limit displacement
K_3	K_n/x_f^2

Figure 2.4: Force-displacement cycles provided by the negative stiffness force where K_n indicates the negative stiffness while x_f and x_n denote the displacements for which the force vanishes or achieves the maximum negative value, respectively.

2.1.3 Superelastic spring

The superelastic response is modelled according to the phenomenological superelastic model proposed by Charalampakis [133] given in rate form as:

$$\dot{f}_s = (1-s)K_s[\dot{x} - |\dot{x}|\text{sign}(f_s-\beta_s)(\tfrac{|f_s-\beta_s|}{Y})^{n_s}] + sK_m\dot{x}, \tag{2.5}$$

$$\beta_s = K_s\alpha_s[x - \tfrac{f_s}{K_s} + f_t\tanh(a_s x)[\tfrac{1+\text{sign}(-x\dot{x})}{2}]], \tag{2.6}$$

$$s = \tfrac{\tanh[c_s(|x|-x_m)]+1}{2}, \tag{2.7}$$

where K_s is the initial stiffness during the austenitic phase, Y is the yielding force and α_s controls the post-elastic stiffness. The parameter n_s regulates the smoothness of transition from the initial elastic to the post-elastic phase while f_t and a_s controls the twinning hysteresis and super-elasticity and the pinching around the origin along the cycle, respectively. Finally, K_m indicates the stiffness during the fully martensitic phase, x_m is the displacement at which the transition from the post-elastic to the fully martensitic phase occurs and c_s controls the smoothness of this transition (see Fig. 2.5).
Because of the large variability and dependence of f_t and a_s on the remaining parameters, two new parameters with a more straightforward physical interpretation, y_s and $\tilde{a}_s$, are introduced. In terms of these parameters, f_t and a_s are expressed as:

$$f_t = (2Y - y_s Y)/(\alpha_s K_s), \tag{2.8}$$

$$a_s = \tanh^{-1}(\tilde{a}_s K_s)/(Y - y_s Y). \tag{2.9}$$

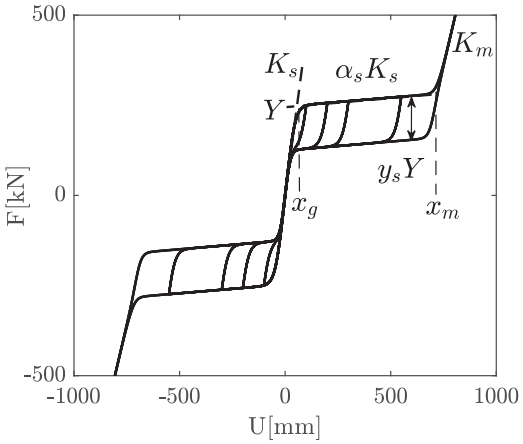

SMA wires parameters	
Y	Yielding force
x_g	Gap displ.
K_s	Y/x_g
α_s	0.01
f_t	6000
n_s	3
a_s	0.06
K_m	0.5 K_s
c_s	0.02
x_m	Martensitic displ.

Figure 2.5: Force-displacement cycles of the superelastic element.

The first parameter indicates the difference between the loading and unloading forces and it is expressed as percentage of Y. The second allows to set the residual displacement to a fixed value varying the other parameters (see Fig. 2.6). In particular, $\tilde{a}_s$ indicates the value assumed by $\tanh(a_s x)$ where x is the displacement at which the unloading branch with stiffness $\alpha_s K_s$ intersects the elastic loading branch.

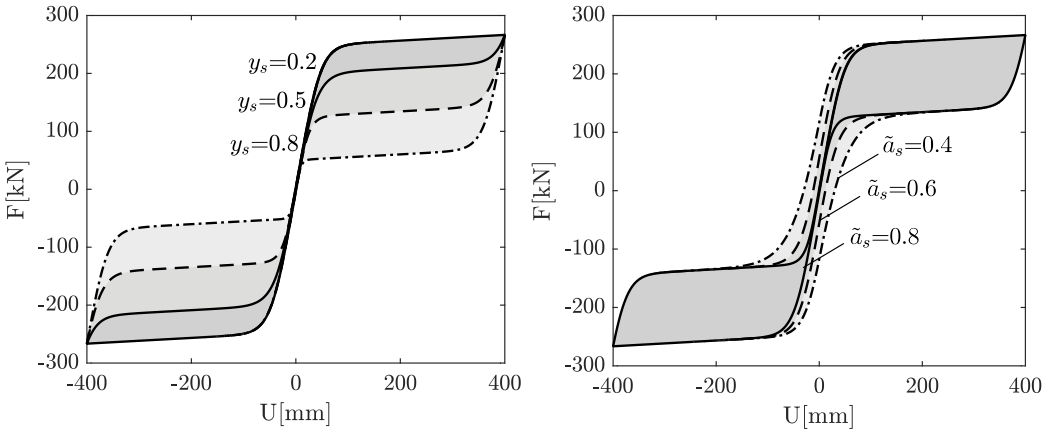

Figure 2.6: Variation of the superelastic force-displacement cycles with the nondimensional parameters y_s (left) and $\tilde{a}_s$ (right).

2.2 Design parameters

The main goal is to investigate the effects of the NS-SMA device in parallel with traditional elastomeric devices. Thus, the stiffness K_i of the isolation system, the gap displacement $x_g = F_w/K_i$, (with F_w indicating the maximum expected wind load) and the maximum allowed displacement x_u are assumed as input parameters (see Fig. 2.7). In this study, x_g is set to $0.05x_u$. On the other hand, K_n, K_3, Y and y_s are the design parameters. All the remaining parameters are set to fixed values ($c = 0.1$, $\alpha = 0.2$, $\beta = 0.09$, $\gamma = 0.01$, $n = 1$, $\alpha_s = 0.01$, $n_s = 3$, $\tilde{a}_s = 0.6$, $c_s = 0.02$) or determined according to the following expressions: $x_m = x_f$, $K_s = Y/x_g$, $f_t = (2Y - y_sY)/(\alpha_sK_s)$, $a_s = \tanh^{-1}(\tilde{a}_sK_s)/(Y - y_sY)$, and $K_m = 0.5K_s$.

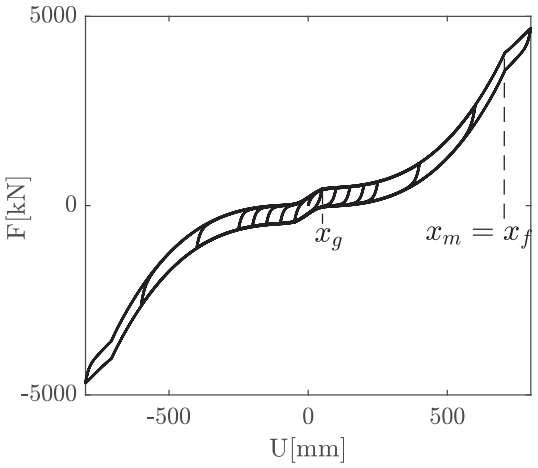

Input parameters	
K_i	Initial stiffness
x_g	Gap displacement
x_u	Maximum displacement
Design parameters	
K_n	Negative stiffness
K_3	Cubic stiffness
Y	Yielding force
y_s	Hysteretic ratio

Figure 2.7: Overall force-displacement cycles provided by S_3 where the gap displacement x_g and the martensitic displacement x_m are indicated.

2.3 Nondimensional equation of motion

The equation of motion of a SDOF mass m subject to the hysteretic restoring force given by Eq. (1) reads:

$$m\ddot{x} + c\dot{x} + \alpha K_i x + (1-\alpha)K_i z + (-K_n x + K_3 x^3)\frac{(1+\text{sign}(x_f - |x|))}{2} + f_s = P(t). \tag{2.10}$$

By choosing a characteristic displacement $x_0 = x_u$ and a characteristic stiffness K_i (i.e., the initial stiffness of the isolation system, equal to the initial stiffness of the Bouc-Wen model), the following nondimensional variables are introduced $\tilde{x} = x/x_0$, $\tilde{t} = \omega t$, where $\omega = \sqrt{K_i/m}$ while the characteristic force is $N_0 = K_i x_0$.

By dividing the equation of motion by N_0, the following nondimensional equation of motion is obtained:

$$\ddot{\tilde{x}}+\zeta\dot{\tilde{x}}+\alpha\tilde{x}+(1-\alpha)\tilde{z}+(-\tilde{K}_n\tilde{x}+\tilde{K}_3\tilde{x}^3)\frac{(1+\text{sign}(\tilde{x}_f-|\tilde{x}|))}{2}+\tilde{f}_s=\tilde{P}(\tilde{t}), \quad (2.11)$$

with $\tilde{P}=P/N_0$, $\tilde{\Omega}_g=\Omega_g/\omega$. Consequently, the nondimensional elastomeric isolators force becomes

$$\tilde{f}_i=\frac{f_i}{N_0}=\zeta\dot{\tilde{x}}+\alpha\tilde{x}+(1-\alpha)\tilde{z}, \quad (2.12)$$

where $\zeta=c\omega/K_i$. Equation (3) can be rewritten in nondimensional form as

$$\dot{\tilde{z}}=\frac{\dot{z}}{x_0\omega}=\dot{\tilde{x}}[1-(\tilde{\gamma}+\tilde{\beta}\text{sign}(\tilde{z}\dot{\tilde{x}}))|\tilde{z}|^n], \quad (2.13)$$

where $\tilde{z}=\frac{z}{x_0}, \tilde{\gamma}=\gamma x_0^n, \tilde{\beta}=\beta x_0^n$.The nondimensional form of equation (4) becomes

$$\tilde{f}_n=\frac{f_n}{N_0}=(-\tilde{K}_n\tilde{x}+\tilde{K}_3\tilde{x}^3)\frac{(1+\text{sign}(\tilde{x}_f-|\tilde{x}|))}{2}, \quad (2.14)$$

with $\tilde{K}_n=\frac{K_n}{K_i}, \tilde{K}_3=\frac{K_3x_0^2}{K_i}, \tilde{x}_f=\frac{x_f}{x_0}$. Finally, also Eqs. (5), (6) and (7) are rendered nondimensional as follows:

$$\dot{\tilde{f}}_s=(1-\tilde{s})\tilde{K}_s[\dot{\tilde{x}}-|\dot{\tilde{x}}|\text{sign}(\tilde{f}_s-\tilde{\beta}_s)(\frac{|\tilde{f}_s-\tilde{\beta}_s|}{\tilde{Y}})^{n_s}]+\tilde{s}\tilde{K}_m\dot{\tilde{x}}, \quad (2.15)$$

$$\tilde{\beta}_s=\tilde{K}_s\alpha_s[\tilde{x}-\frac{\tilde{f}_s}{\tilde{K}_s}+\tilde{f}_t\tanh(\tilde{a}_s\tilde{x})[\frac{1+\text{sign}(-\tilde{x}\dot{\tilde{x}})}{2}]], \quad (2.16)$$

$$\tilde{s}=\frac{\tanh[\tilde{c}_s(|\tilde{x}|-\tilde{x}_m)]+1}{2}, \quad (2.17)$$

after introducing the following nondimensional parameters:
$\tilde{K}_s=\frac{K_s}{K_i}, \tilde{K}_m=\frac{K_m}{K_i}, \tilde{Y}=\frac{Y}{N_0}, \tilde{f}_t=\frac{f_t}{x_0}, \tilde{a}_s=a_sx_0, \tilde{c}_s=a_sx_0, \tilde{x}_m=\frac{x_m}{x_0}$.

The nondimensional equations of motion (2.11), (2.13) and (2.15) can be written in the state space formulation introducing the state space variable $\tilde{y}$ defined as:

$$\tilde{y}=\begin{pmatrix}\tilde{x}\\ \dot{\tilde{x}}\\ \tilde{z}\\ \tilde{f}_s\end{pmatrix} \quad (2.18)$$

The equations of motion in the form

$$\dot{\tilde{y}}=f(\tilde{y},t) \quad (2.19)$$

becomes

$$\dot{\tilde{y}}_1 = \tilde{y}_2, \tag{2.20}$$

$$\dot{\tilde{y}}_2 = \tilde{P}(\tilde{t}) - (\zeta\dot{\tilde{x}} + \alpha\tilde{x} + (1-\alpha)\tilde{z} + (-\tilde{K}_n\tilde{x} + \tilde{K}_3\tilde{x}^3)\tfrac{(1+\mathrm{sign}(\tilde{x}_f - |\tilde{x}|))}{2} + \tilde{f}_s), \tag{2.21}$$

$$\dot{\tilde{y}}_3 = \dot{\tilde{x}}[1 - (\tilde{\gamma} + \tilde{\beta}\,\mathrm{sign}(\tilde{z}\dot{\tilde{x}}))|\tilde{z}|^n], \tag{2.22}$$

$$\dot{\tilde{y}}_4 = (1-\tilde{s})\tilde{K}_s[\dot{\tilde{x}} - |\dot{\tilde{x}}|\mathrm{sign}(\tilde{f}_s - \tilde{\beta}_s)(\tfrac{|\tilde{f}_s - \tilde{\beta}_s|}{\tilde{Y}})^{n_s}] + \tilde{s}\tilde{K}_m\dot{\tilde{x}}. \tag{2.23}$$

Chapter 3

Static analysis

3.1 Analytical equilibrium response

In order to investigate the stability characteristics of the system, the hysteretic response of the system can be thought of as the sum of the equilibrium response without dissipative effects, the underlying conservative system, and the hysteresis providing dissipation. With this assumption, the underlying conservative response can be identified with the median force of the hysteretic cycle. Although the force-displacement laws are first-order differential equations, the equilibrium response can be properly described in closed-form by a piece-wise analytical equation. In particular, the response is described by $\tilde{f}_{e1}(\tilde{x})$ for $\tilde{x} < \tilde{x}_{gapm} = \tilde{Y}(2-y_s)/(2\tilde{K}_s)$, by $\tilde{f}_{e2}(\tilde{x})$ for $\tilde{x}_{gapm} < \tilde{x} < \tilde{x}_f$ and by $\tilde{f}_{e3}(\tilde{x})$ for $\tilde{x} > \tilde{x}_f$ where

$$\tilde{f}_{e1}(\tilde{x}) = (\alpha + \tilde{K}_s + \tilde{K}_n)\tilde{x} + \tilde{K}_3\tilde{x}^3 \tag{3.1}$$

$$\tilde{f}_{e2}(\tilde{x}) = (\alpha + \tilde{K}_n)\tilde{x} + \alpha_s\tilde{K}_s(\tilde{x} - \tilde{x}_{gapm}) + \tilde{K}_s\tilde{x}_{gapm} + \tilde{K}_3\tilde{x}^3 \tag{3.2}$$

$$\tilde{f}_{e3}(\tilde{x}) = \alpha\tilde{x} + \alpha_s\tilde{K}_s(\tilde{x} - \tilde{x}_{gapm}) + \tilde{K}_s\tilde{x}_{gapm} + \tilde{K}_m(\tilde{x} - \tilde{x}_f). \tag{3.3}$$

Integrating and differentiating the three equations, the potential energy and the tangent stiffness for each branch are, respectively, obtained as

$$\tilde{W}_1(\tilde{x}) = \tfrac{1}{2}\tilde{x}^2\left(\alpha + \tilde{K}_s + \tilde{K}_n\right) + \tfrac{1}{4}\tilde{K}_3\tilde{x}^4, \tag{3.4}$$

$$\tilde{W}_2(\tilde{x}) = \tfrac{1}{2}\tilde{x}^2\left(\alpha + \alpha_s\tilde{K}_s + \tilde{K}_n\right) + \tfrac{1}{4}\tilde{K}_3\tilde{x}^4 + \tilde{x}(1-\alpha_s)\tilde{x}_{\mathrm{gapm}}\tilde{K}_s - \\ -\tfrac{1}{2}(1-\alpha_s)\tilde{x}^2_{\mathrm{gapm}}\tilde{K}_s, \tag{3.5}$$

$$\tilde{W}_3(\tilde{x}) = \tfrac{1}{2}\tilde{x}^2\left(\alpha + \alpha_s\tilde{K}_s + \tilde{K}_m\right) + \tfrac{1}{4}\tilde{K}_3\tilde{u}_f^4 + \tfrac{1}{2}\tilde{u}_f^2\left(\tilde{K}_m + \tilde{K}_n\right) - \tilde{x}\tilde{u}_f\tilde{K}_m - \\ -\tfrac{1}{2}(1-\alpha_s)\tilde{x}^2_{gapm}\tilde{K}_s + \tilde{x}(1-\alpha_s)\tilde{x}_{gapm}\tilde{K}_s. \tag{3.6}$$

while the piece-wise tangent stiffness for each branch is given by

$$\tilde{K}_{t1}(\tilde{x}) = \alpha + \tilde{K}_s + \tilde{K}_n + 3\tilde{K}_3\tilde{x}^2, \tag{3.7}$$

$$\tilde{K}_{t2}(\tilde{x}) = \alpha + \alpha_s\tilde{K}_s + \tilde{K}_n + 3\tilde{K}_3\tilde{x}^2, \tag{3.8}$$

$$\tilde{K}_{t3}(\tilde{x}) = \alpha + \tilde{K}_m. \tag{3.9}$$

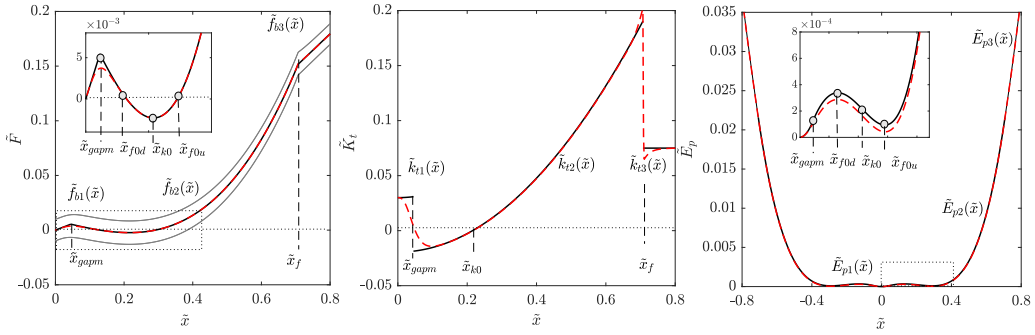

Figure 3.1: Analytical vs. numerical (in black and red dashed lines, respectively) equilibrium response, tangent stiffness and energy profile. Gray lines indicate the branches of the hysteresis loop.

Comparing the numerical results with the analytical ones a good match is found (see Fig. 3.1). A small gap between the two results exists across the discontinuity $\tilde{x}_{gapm}$ and $\tilde{x}_f$ because of the smoothness of the numerical response. Along the second branch, in addition to $\tilde{x}_{gapm}$, three characteristic displacements exist $\tilde{x}_{k0}$, $\tilde{x}_{f0d}$ and $\tilde{x}_{f0u}$. For a displacements equal to $\tilde{x}_{gapm}$ and to $\tilde{x}_{k0}$ tangent stiffness vanishes and the restoring force has the local maximum and the minimum values, respectively. In the potential energy profile, these two points correspond to flexion points. The points $\tilde{x}_{f0d}$ and $\tilde{x}_{f0u}$ denote the displacements where the force is equal to zero and correspond, respectively, to the biased unstable and stable equilibria. Solving $\tilde{k}_{t1}(\tilde{x}) = 0$ and $\tilde{f}_{e1}(\tilde{x}) = 0$ the formulas furnishing $\tilde{x}_{k0}$, $\tilde{x}_{f0d}$ and $\tilde{x}_{f0u}$ are obtained as

$$\tilde{x}_{k0} = \sqrt{\frac{\alpha+\alpha_s\tilde{K}_s+\tilde{K}_n}{3\tilde{K}_3}} \tag{3.10}$$

$$\tilde{x}_{f0d} = \frac{2}{\sqrt{3}}\sqrt{-\frac{\tilde{K}_n+\alpha_s\tilde{K}_s+\alpha}{\tilde{K}_3}}\sin\left[\frac{1}{3}\sin^{-1}\left(\frac{3\sqrt{3}\tilde{x}_{\mathrm{gapm}}\left(\tilde{K}_s-\alpha_s\tilde{K}_s\right)}{2\tilde{K}_3\left(-\frac{\tilde{K}_n+\alpha_s\tilde{K}_s+\alpha}{\tilde{K}_3}\right)^{3/2}}\right)\right] \tag{3.11}$$

$$\tilde{x}_{f0u} = \frac{2}{\sqrt{3}}\sqrt{-\frac{\tilde{K}_n+\alpha_s\tilde{K}_s+\alpha}{\tilde{K}_3}}\cos\left[\frac{1}{3}\sin^{-1}\left(\frac{3\sqrt{3}\tilde{x}_{\mathrm{gapm}}\left(\tilde{K}_s-\alpha_s\tilde{K}_s\right)}{2\tilde{K}_3\left(-\frac{\tilde{K}_n+\alpha_s\tilde{K}_s+\alpha}{\tilde{K}_3}\right)^{3/2}}\right)+\frac{\pi}{6}\right] \tag{3.12}$$

Using these equations, it is possible to track the locations of the characteristic points upon variation of the main design parameters, $\tilde{K}_n$ and $\tilde{K}_3$, and obtain useful information about the stability of the response.

3.1.1 Effects of $\tilde{K}_n$ on stability

Firstly, the effects of parameter $\tilde{K}_n$ on stability are studied. Figure 3.2 shows the evolution of the characteristic points versus $\tilde{K}_n$.

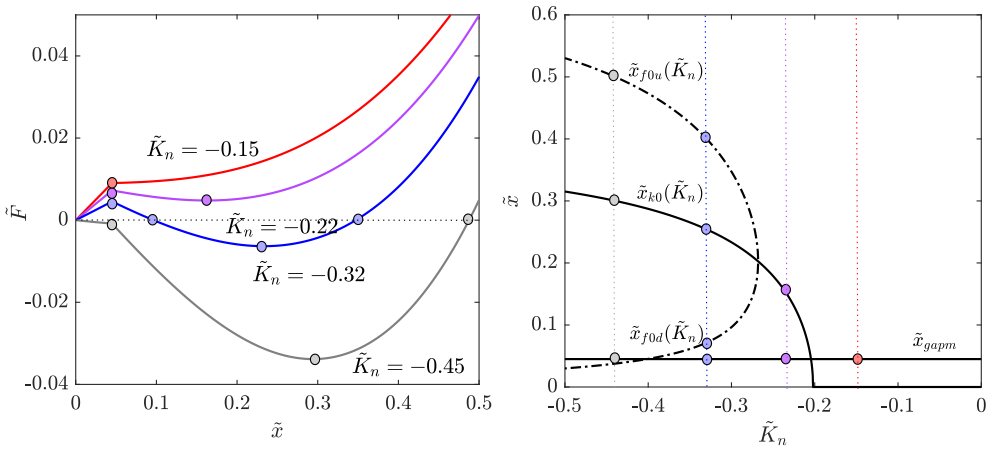

Figure 3.2: (left) Elastic equilibrium response of the system with $\tilde{K}_n = (-0.15, -0.22, -0.32, -0.45)$ and $\tilde{K}_3 = -2e^{-06}\tilde{K}_n$ (red, violet, blue and gray lines, respectively). (right) Analytically obtained $\tilde{x}_{k0}$, $\tilde{x}_{f0d}$ and $\tilde{x}_{f0u}$ vs. negative stiffness coefficient $\tilde{K}_n$.

For low levels of negative stiffness, $\tilde{K}_n = -0.15$, only the local maximum point exists at $\tilde{x}_{gapm}$, the tangent stiffness is positive and the equilibrium is unique. This type of response is a mono-stable response (MSr). For larger levels of negative stiffness, $\tilde{K}_n = -0.22$, a local minimum appears at $\tilde{x}_{k0}$. This implies the existence of branches of negative tangent stiffness that cause snap-through phenomena. This type of response is a snap-through response (STr). With $\tilde{K}_n = -0.32$ two lateral equilibrium positions are born, hence the system is tri-stable (TSr). Finally increasing further $\tilde{K}_n = -0.45$ the stiffness at the origin becomes negative so the trivial equilibrium loses stability and the system become bi-stable (BSr). Therefore, four different types of response exist (MSr, STr, TSr and BSr) and the transition values of $\tilde{K}_n$ between the different types of response is predictable in an analytical fashion (see Fig. 3.3). In particular, the intersection between the curves $\tilde{x}_{k0}(\tilde{K}_n)$ and $\tilde{x}_{gapm}(\tilde{K}_n)$ determines the finish of the mono-stable region and the

beginning of the snap-through region, the point of intersection between $\tilde{x}_{k0}(\tilde{K}_n)$, $\tilde{x}_{f0d}(\tilde{K}_n)$ and $\tilde{x}_{f0u}(\tilde{K}_n)$ determines the onset of the tri-stable region and finally the intersection between $\tilde{x}_{gapm}(\tilde{K}_n)$ and $\tilde{x}_{f0d}(\tilde{K}_n)$ identifies the onset of the bi-stable region.

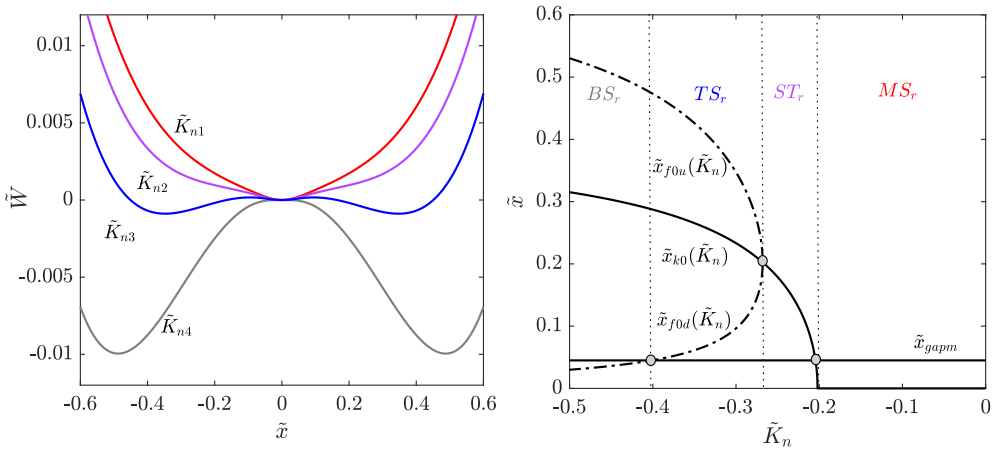

Figure 3.3: (left) Potential energy profile of the system with $\tilde{K}_n = (-0.15, -0.22, -0.32, -0.45)$ and $\tilde{K}_3 = -2e^{-06}\tilde{K}_n$ (red, violet, blue and gray lines, respectively). (right) Analytically obtained $\tilde{x}_{k0}$, $\tilde{x}_{f0d}$ and $\tilde{x}_{f0u}$ vs negative stiffness coefficient $\tilde{K}_n$ and bounding values between stability types.

3.1.2 Effects of $\tilde{K}_3$ on stability

By fixing the negative stiffness coefficient $\tilde{K}_n$ and changing the ratio $\tilde{K}_3/\tilde{K}_n$, the effects of $\tilde{K}_3$ on stability are investigated next. Depending on the value of $\tilde{K}_n$ upon changing $\tilde{K}_3$, three different types of response can be obtained, namely, MSr, STr and TSr (see Fig. 3.4).

3.1.3 Type of stability in the ($\tilde{K}_n$, $\tilde{K}_3$, $\tilde{K}_s$) 3D space

By imposing ad hoc conditions on the tangent stiffness, transition values between the four response types (MSr, STr, TSr and BSr) are analytically obtained.
Transition value between MSr and STr

$$\begin{aligned} min(\tilde{K}_t(\tilde{x})) = 0 \Rightarrow \tilde{K}_{t2}(\tilde{x}_{gapm}) = 0 \\ \tilde{K}_{n\,MS\to ST} = -\alpha - \alpha_s\tilde{K}_s - 3\tilde{K}_3\tilde{x}^2_{gapm} \end{aligned} \tag{3.13}$$

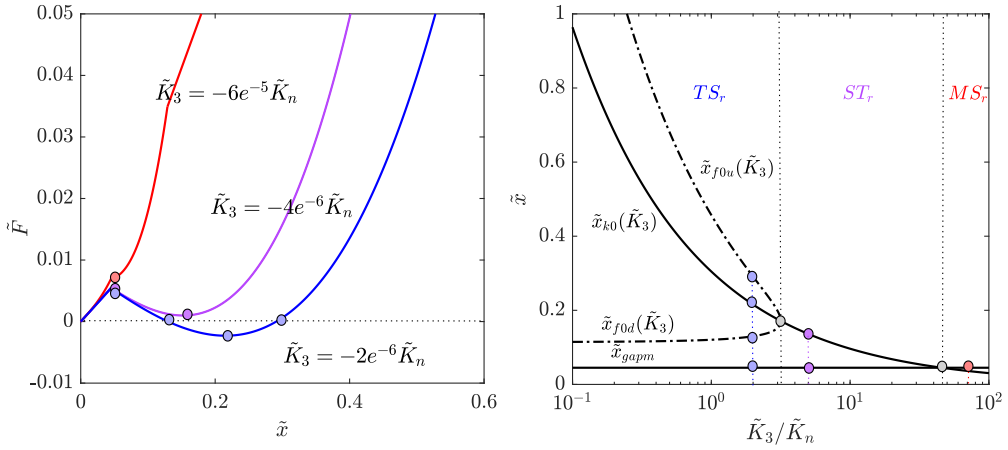

Figure 3.4: (left) Equilibrium response for the system with $\tilde{K}_3 = -(2,4,60)\tilde{K}_n$ and $\tilde{K}_n = -0.32$ (red, violet, blue and gray lines, respectively). (right) Analytically obtained $\tilde{x}_{k0}$, $\tilde{x}_{f0d}$ and $\tilde{x}_{f0u}$ as function of negative stiffness coefficient $\tilde{K}_n$.

Transition value between STr and TSr

$$min(\tilde{f}_{b2}(\tilde{x})) = 0 \Rightarrow \tilde{f}_{b2}(\tilde{x}_{02}) = 0 \; with \; \tilde{x}_{02} : \tilde{K}_{t2}(\tilde{x}_{02}) = 0$$
$$\tilde{K}_{n\ ST\rightarrow TS} = -\alpha - \alpha_s\tilde{K}_s - 3\sqrt[3]{\frac{(-1+\alpha_s)^2\tilde{K}_3\tilde{K}_s^2\tilde{x}_{gapm}^2}{4}} \tag{3.14}$$

Transition value between TSr and BSr

$$\tilde{K}_{t1}(0) = 0$$
$$\tilde{K}_{n\ TS\rightarrow BS} = -\alpha - \tilde{K}_s \tag{3.15}$$

In the design parameters ($\tilde{K}_n$, $\tilde{K}_3$, $\tilde{K}_s$) 3D space these equations represent three surfaces, that divide the latter in four regions corresponding to the different stability behaviours (MSr, STr, TSr and BSr). In Fig. 3.5 are reported analytically obtained transition surfaces, together with their traces with a ($\tilde{K}_n$, $\tilde{K}_3$) plane and a ($\tilde{K}_n$, $\tilde{K}_s$) plane.
Increasing the value of $\tilde{K}_s$ an expansion of the ST and TS regions and a compression of the BS region are noticed, while the transition curve $MS \rightarrow ST$ remains unaffected (see Fig. 3.5b). On the other hand, an increase of the value of $\tilde{K}_3$ causes a shift of the curve $ST \rightarrow TS$ to the left and the associated expansion of ST region, while the curves $MS \rightarrow ST$ and $TS \rightarrow BS$ remain unaltered (see Fig. 3.5c).

A useful and common method for studying the stability of a nonlinear oscillator is the characterisation of Hamiltonian orbits. The Hamiltonian orbits are the orbits described by the underliyng conservative oscillator in the state space

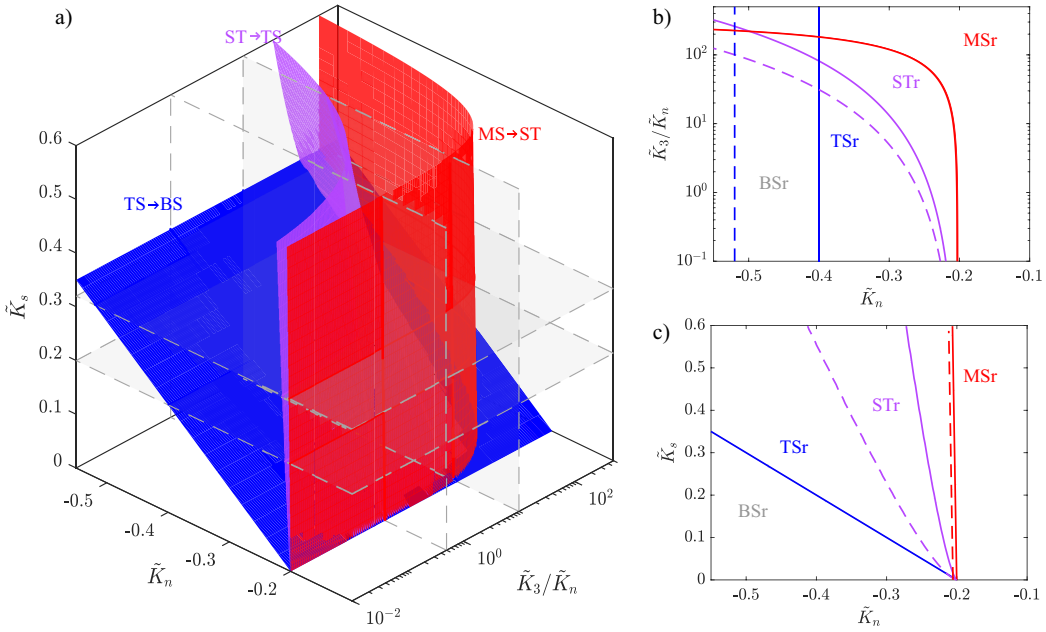

Figure 3.5: Analytical transition surfaces between MSr, STr, TSr and BSr (in red, violet and blue, respectively) in the ($\tilde{K}_n$, $\tilde{K}_3$, $\tilde{K}_s$) parameters space.(b) Traces of transition surfaces with ($\tilde{K}_n$, $\tilde{K}_3$) plane for $\tilde{K}_s = 0.2, 0.32$ (solid and dashed lines, respectively). (c) Traces of transition surfaces with ($\tilde{K}_n$, $\tilde{K}_s$) plane for $\tilde{K}_3/\tilde{K}_n = 0.5, 10$ (solid and dashed lines, respectively).

$(\tilde{x}, \dot{\tilde{x}})$ and are distinguished by the conservation of mechanical energy (H), that is defined as

$$H(\tilde{x}, \dot{\tilde{x}}) = T(\dot{\tilde{x}}) + W(\tilde{x}), \tag{3.16}$$

where $T = \frac{1}{2} m \dot{\tilde{x}}^2$ is the kinetic energy of the oscillator and W is the potential energy. By computing the Hamiltonian in the instant corresponding to the condition of maximum potential energy and null kinetic energy for a given maximum orbit displacement $\tilde{x}_0$ as

$$H_0(\tilde{x}_0, \dot{\tilde{x}} = 0) = T(0) + W(\tilde{x}_0) = W(\tilde{x}_0), \tag{3.17}$$

and considering the conservation of mechanical energy

$$H(\tilde{x}, \dot{\tilde{x}}) = H_0(\tilde{x}_0, \dot{\tilde{x}} = 0) = W(\tilde{x}_0), \tag{3.18}$$

the state space orbits can be defined as follows

$$\tilde{v} = \sqrt{2 \frac{W(\tilde{x}_0) - W(\tilde{x})}{m}}. \tag{3.19}$$

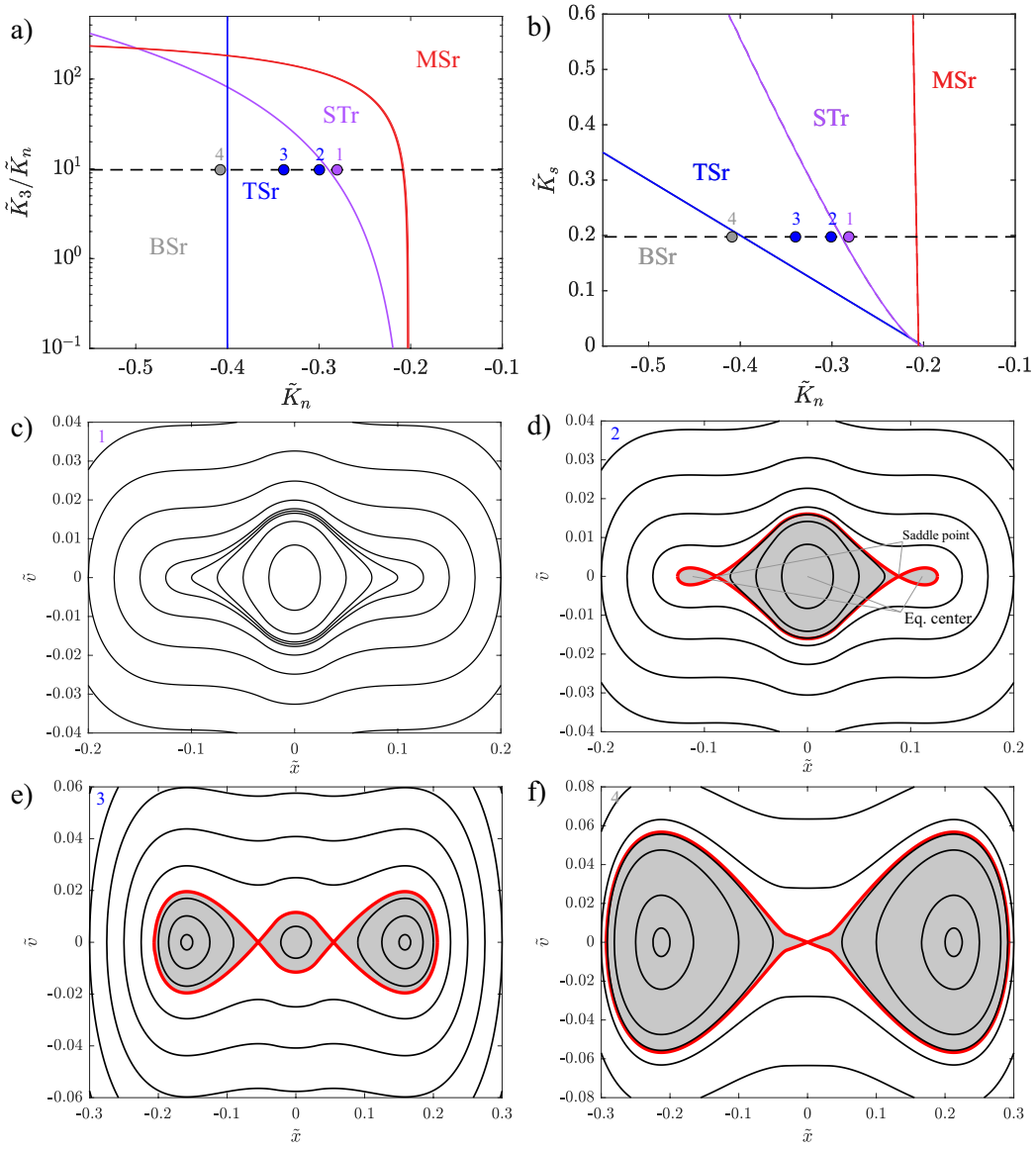

Figure 3.6: Stability regions in the $(\tilde{K}_n, \tilde{K}_3)$ and $(\tilde{K}_n, \tilde{K}_s)$ planes (a, b) and Hamiltonian orbits of the system with $\tilde{K}_3 = -10\tilde{K}_n$ and $\tilde{K}_s = 0.2$ for values of $\tilde{K}_n$ equal to 0.28 (c), to 0.29 (d), to 0.32 (e) and to 0.42 (f) (ST, TS and BS state, respectively).

In Fig. 3.6 the Hamiltonian orbits for configurations belonging to the STr, TSr and BSr are shown. The ST configuration exhibit one equilibrium center in zero and a strecthing of the orbits near the loci of null tangent stiffness ($\tilde{x}_{k0}$). The Hamiltonian orbits associated with the Tri-stable configuration are characterized by the existence of lateral saddle joints and lateral equilibrium centers, located at $\tilde{x}_{f0d}$ and $\tilde{x}_{f0u}$ respectively. In particular, the orbit passing through the lateral saddle

joints divides the state space in intra-well and inter-well orbits. The first group are the orbits within the central or lateral wells, while the second group are those that travel on trajectories outside the wells. In the Bi-stable region, the lateral saddle joints coalesce and replace the trivial equilibrium center. The reliability of the analytical predictions on the stability behaviour of system are validated numerically through the computation of the basins of attraction in free oscillations of the real (hysteretic) oscillator. The equations of motion are numerically integrated for a grid of initial conditions. The initial conditions, in terms of displacement and velocity, that lead to different attractors are denoted by different colors. In Fig. 3.7 the basins computed for configurations associated with a ST, to a TS and to a BS state are shown.

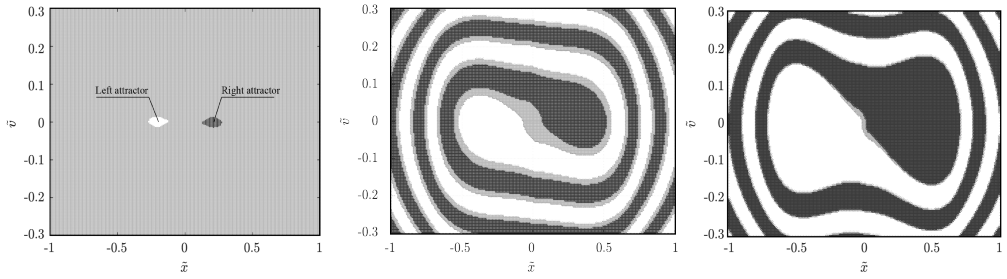

Figure 3.7: Numerically obtained basins of attraction in free oscillations of the system with $\tilde{K}_3 = 2\tilde{K}_n, \tilde{K}_s = 0.2$ and $\tilde{K}_n = -0.25$ (left), $\tilde{K}_n = -0.3$ (left) and $\tilde{K}_n = -0.41$.

In particular, the initial conditions that lead to the right equilibrium are denoted by black dots, the ones that lead to the lateral left equilibrium by white dots and, finally, the initial conditions that lead to the trivial equilibrium are indicated by gray dots. The basin corresponding to the ST state is almost totally gray, this denotes the self-recentering capacity of the selected configuration and the unicity of the trivial equilibrium center. The basin of attraction of the TS configuration shows three distinct attractors, while those associated with the BS configuration shows only the two non trivial equilibria given the instability of the trivial state.

3.2 Equivalent stiffness and damping

Given the dependence in nonlinear oscillators of stiffness and damping on the amplitude of motion, a useful way to characterize the dynamic behavior of the hysteretic oscillator is to make use of the equivalent linearization. The equivalent linear stiffness (K_{eq}) for a given displacement amplitude (U) has been calculated by considering the equivalence between the elastic energy of the real nonlinear

oscillator ($W(U)$) and the one of the equivalent linear oscillator ($W_{el}(U)$). The elastic energy of the real and of the equivalent oscillator can be defined as

$$W(U) = \int_0^U f_m(x)dx, \tag{3.20}$$
$$W_{el}(U) = \tfrac{1}{2}K_{eq}(U)U^2, \tag{3.21}$$

where $f_m(x)$ denotes the median force between loading and unloading branch of the hysteretic cycle. The equivalent damping is obtained as the ratio between the damped energy during a cycle (E_d) and the associated elastic work ($4W$) multiplying π. The equivalent linear stiffness and damping ratio can be defined as function of the displacement amplitude (U) as

$$K_{eq}(U) = \frac{2W(U)}{U^2}, \xi(U) = \frac{E_d(U)}{4\pi W(U)}, \tag{3.22}$$

Firstly, the equivalent stiffness and damping for the system composed by superelastic element alone arranged in parallel with the elastomeric device (system S_2) are investigated. In order to clarify the effects of the design parameters, three different cases are reported in Fig. 3.8: ($Y = Z_m, \tilde{K}_s = \alpha, y_s = 0.2$) (red dashed line), ($Y = Z_m, \tilde{K}_s = \alpha, y_s = 0.8$) (red solid line), ($Y = 1.6Z_m, \tilde{K}_s = 1.6\alpha, y_s = 0.8$) (red dashed dotted line).

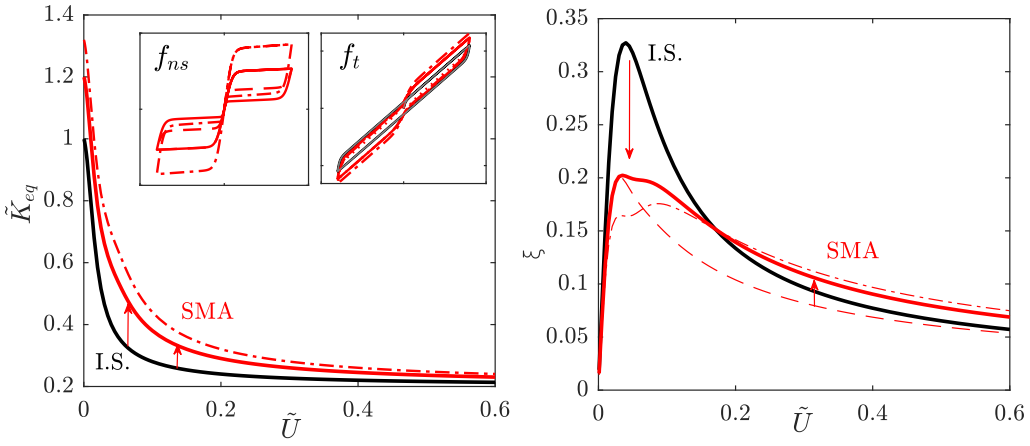

Figure 3.8: Equivalent nondimensional stiffness vs. nondimensional displacement amplitude (left) and equivalent damping vs. nondimensional amplitude (right) for S_1 (black line), S_2 with $Y = Z_m, y_s = (0.2, 0.8)$ (dashed and solid red lines, respectively) and with $Y = 1.6Z_m, y_s = 0.8$ (dashed-dotted red line). The subfigures show the hysteresis loops of device (a) and system (b) for the parameters described above.

The trends of equivalent stiffness and damping in Fig. 3.8 show that, for low ratios

of super-elastic hysteresis (y_s) (see dashed red curve), the only effect is an increase in stiffness that causes a reduction of equivalent damping in the low amplitude range. For greater ratios of superelastic hysteresis, a small increase of damping is achieved for moderate and large displacements, whereas, for low amplitudes, a decrease of damping persists. Increasing the yielding force (Y) entails an increase of initial stiffness; hence, the damping reduction at low amplitudes is more significant. Moreover, a damping increment is exhibited for large displacements. The introduction of the superelastic element within the isolation system, regardless from its hysteresis contribution, causes a decrease in seismic isolation performance for low intensity earthquakes characterized by high frequency of occurrence (because of an increase in stiffness and a subsequent decrease of the damping). On the other hand, a slight improvement of performance is obtained for medium and high intensity earthquakes. By considering next the case ($Y = Z_m, y_s = 0.8$), Figure 3.9 shows that the introduction of negative stiffness drastically amplifies the equivalent damping. In fact, while the maximum increase of damping achieved with the superelastic element alone was of $\simeq 2\%$, with $\tilde{K}_n = -(0.5, 1, 1.2)\alpha$ and $\tilde{K}_3 = -2\tilde{K}_n$, the achieved increments are $\simeq (10, 30, 90)\%$, respectively.

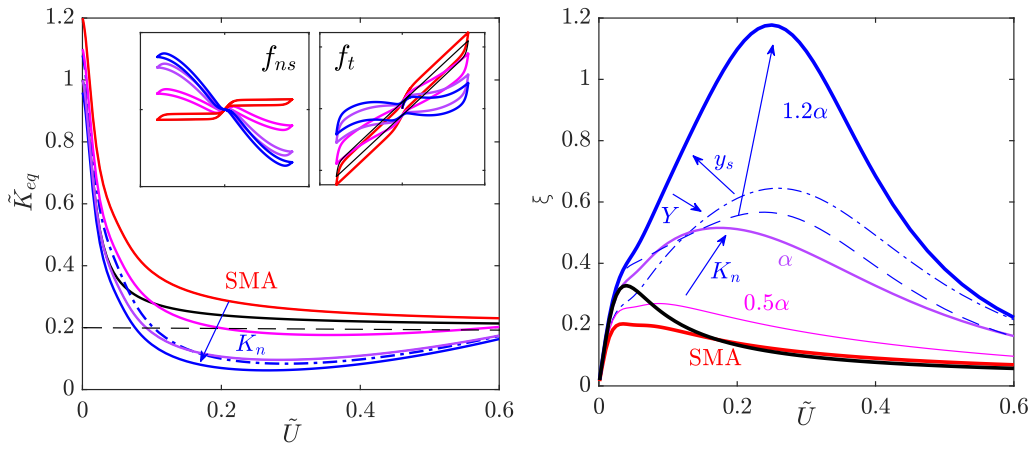

Figure 3.9: Equivalent nondimensional stiffness vs. nondimensional displacement amplitude (left) and equivalent damping vs. nondimensional amplitude (right) for S_1 (black line), S_2 with $Y = Z_m, y_s = 0.8$ (red line), S_3 with $\tilde{K}_3 = -2\tilde{K}_n$ and $\tilde{K}_n = -(0.5, 1, 1.2)\alpha$ (magenta, violet, blue lines, respectively); the blue dashed-lines represent the case $\tilde{K}_n = -1.2\alpha, Y = Z_m, y_s = 0.2$, the blue dashed-dotted lines represent the case $\tilde{K}_n = -1.2\alpha, Y = 1.6Z_m, y_s = 0.8$, while the sub-figures show the hysteresis loops for the assigned parameters.

As already seen for the system S_2, the increase of the hysteresis ratio y_s entails an increase of the equivalent damping, while the increase of the yielding force Y

gives rise to an increase of the initial stiffness and thus a drop of the equivalent damping over a broad range of displacements. In addition, it is possible to note that the system with $\tilde{K}_3 = -2\tilde{K}_n, \tilde{K}_n = -1.2\alpha$ (ST configuration) exhibits an over-damped behaviour. In Fig. 3.10 it is shown that, for $\tilde{K}_n = -1.2\alpha$, the response is still mono-stable but exhibits a negative stiffness range and the damped energy profile along the associated branch is greater than the potential profile, determining an over-damped condition. For values of $\tilde{K}_n < -1.2\alpha$, the median line of the hysteresis loops intersects the abscissa line (i.e., the force vanishes), 2 lateral minima in the energy profile appear and the system becomes globally tri-stable. This means that exists a shift between the $ST \rightarrow TS$ transition surface and the surface bounding the under-damped and the over-damped regions.

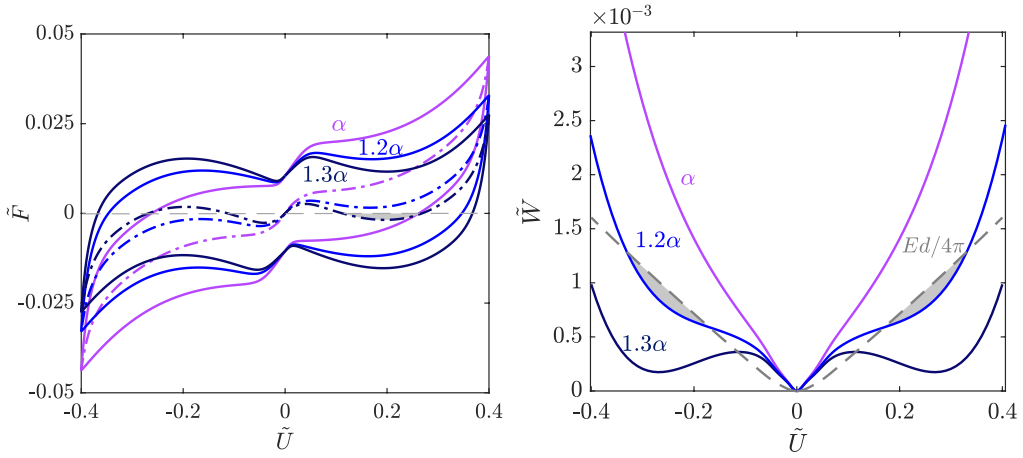

Figure 3.10: (left) Force displacement cycles together with the average force in dashed-dotted lines and (right) potential energy profiles of system S_3 with $Y = Z_m, y_s = 0.8, \tilde{K}_3 = -2\tilde{K}_n$ and $\tilde{K}_n = (1, 1.2, 1.3)\alpha$ represented by magenta, blue, and violet lines, respectively. The gray dashed lines denotes the damped energy profile

Figure 3.11 shows the evolution of the minimum value of equivalent stiffness curve and of the maximum value of damping curve as function of the value of $\tilde{K}_n$ for a system S_3 with $\tilde{K}_3 = -2\tilde{K}_n, Y = Z_m, y_s = 0.8$. By increasing negative stiffness level is possible to obtain strong reduction of equivalent stiffness up to $K_{eq} \leq 0$ and drastic amplification of damping up to $\xi \geq 1$. The minimum value of equivalent stiffness curve shows a quasi-linear trend, while the maximum value of damping curve exhibits an exponential evolution. This means that most of damping amplification is obtained in a small range of negative stiffness values. In fact, an increase of $\tilde{K}_n$ from 0 to 0.15 produce an amplification of only $\simeq 10\%$ in damping, while, in the range between 0.15 and 0.22, corresponding to the ST region,

the increase obtained is $\simeq 70\%$. It is shown also that an increase of $\tilde{K}_s$, hence of the value of superelastic yielding force Y, as well as a decrease of the hysteresis ratio y_s, induces a delay in the damping amplification. Two distinct regions asso-

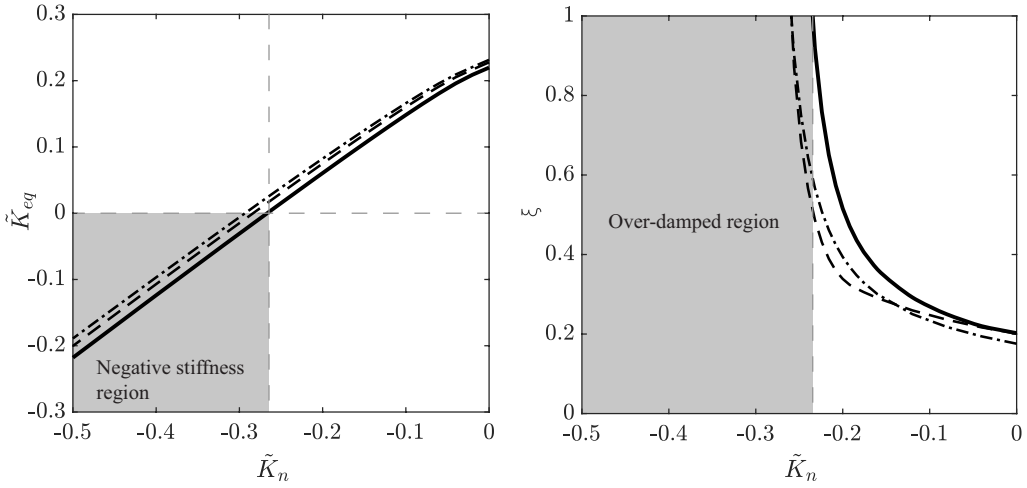

Figure 3.11: Evolution of the minimum value of equivalent stiffness curve (left) and of the maximum value of damping curve (right) in function of the value of $\tilde{K}_n$ for system S_3 with $\tilde{K}_3 = -2\tilde{K}_n, Y = Z_m, y_s = (0.2, 0.8)$ (dashed and solid lines respectively) and with $\tilde{K}_3 = -2\tilde{K}_n, Y = 1.6Z_m, y_s = 0.8$ (dashed-dotted lines).

ciated with a negative equivalent stiffness and with an over-damped response are identifiable in the 3D space of design parameters. As shown in Fig. 3.12, both the boundary surface between positive and negative equivalent stiffness regions and the boundary surface between under-damped and over-damped regions are offset of the $ST \rightarrow TS$ surface. The first surface, associated with $K_{eq} \leq 0$, lies within the TS region, while, the surface associated with $\xi \geq 1$, lies in the ST region. This means that the configurations belonging to the intersection portion of parameter space between the over-damped region and the ST region exhibit simultaneously self-recentering capabilities and over- damped behaviour, that is a promising and desirable combination of features for an isolation system.

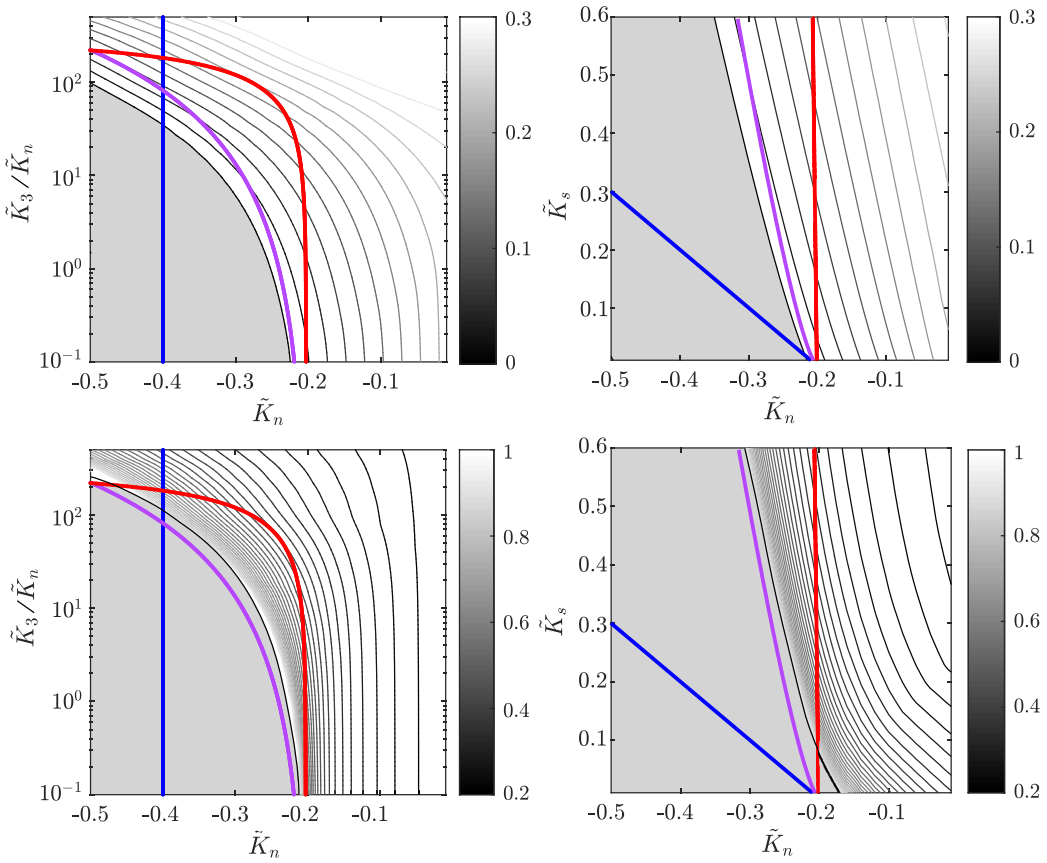

Figure 3.12: Contour levels of the minimum value of equivalent stiffness curve (up) and of the maximum value of damping curve (bottom) in the ($\tilde{K}_n$, $\tilde{K}_3$) plane when $\tilde{K}_s = 0.2$ and in the ($\tilde{K}_n$, $\tilde{K}_s$) plane with $\tilde{K}_3 = -2\tilde{K}_n$. In gray are denoted the negative equivalent stiffness region (up) and the over-damped region (bottom).

3.3 Conclusions

The first step of the investigation has involved the static characterization of the response of the dimensionless system in terms of stability, stiffness and equivalent damping, highlighting the presence of different types of stability in the ($\tilde{K}_n$, $\tilde{K}_3$, $\tilde{K}_s$) design parameters space. In particular, depending from the design parameters selected, it is possible to obtain Mono-Stable, Snap-Trough, Tri-Stable and Bi-Stable types of response. In addition, is proven the possibility of obtaining almost zero stiffness together with amplifications of the damping up to over-damped responses. Of particulare interest results the existence of a compenetration region between the Snap-Trough and the over-damped regions, which allow to obtain self-recentering and highly damped responses.

Chapter 4

Nonlinear dynamic response to harmonic excitation

The frequency-response curves (FRCs) of the described hysteretic oscillators endowed with the rheological devices S_1, S_2, S_3 are numerically obtained for several excitation levels employing a continuation procedure based on the Poincarè map. The Poincarè map and the associated monodromy matrix are computed via the fourth-order Runge-Kutta integration scheme and the finite difference method, respectively. The stability and the bifurcations along the path of periodic solutions are ascertained according to the eigenvalues of the monodromy matrix [134]. In the next subsections, a full parametric analysis is carried out to investigate the sensitivity of the FRCs with respect to the design parameters.

4.1 Effects of design parameters on dynamic response

4.1.1 Linear and nonlinear negative stiffness

Figure 4.1 shows the displacement and acceleration FRCs for the baseline isolation system (S_1) (denoted by black lines), for the isolation system with the SMA damper (S_2) assuming $\tilde{K}_s = \alpha, \tilde{x}_g = 0.05, y_s = 0.2$, (denoted by red lines) and for the isolation system with the same SMA damper plus the negative stiffness (S_3) with $\tilde{K}_n = (0.5, 1, 1.2)\alpha$ and $\tilde{K}_3 = -2\tilde{K}_n$ under two excitation amplitudes, $\tilde{A}_g = (0.01, 0.015)$. As expected, the addition of the superelastic element induces an increase of stiffness that is larger for low amplitudes, and results in a shift of the curves to the right with an increase of the acceleration and a decrease of the displacement (see the red lines in Fig. 4.1). The addition of negative stiffness implies a reverse shift of the curves to the left, a decrease of the acceleration and

an increase of the displacement. It is interesting to note that, despite the stiffness of S_3 being much lower than that of the baseline system S_1, the maximum displacement is always smaller, at most equal, thanks to the beneficial effect of the augmented damping. The peak of absolute accelerations transmissibility, or force transmissibility, defined as the ratio between absolute acceleration and base acceleration, results for the S_1 configuration equal to 2.5 and 7, for low and high excitation ($\tilde{A}_g = (0.01, 0.015)$) respectively, while for the S_2 configuration is equal to 3.3 and 6.1. The S_3 system exhibits a halved force transmissibility peak for both the excitation amplitudes (1.8 and 4).

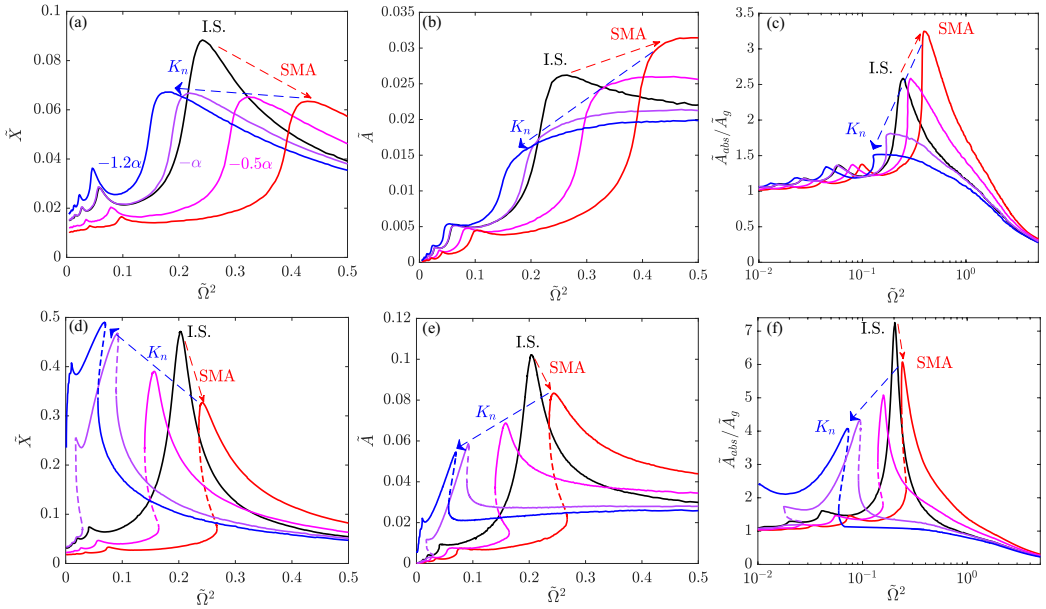

Figure 4.1: Frequency-response curves (FRCs) in terms of nondimensional displacement (left), acceleration (center), and force transmissibility for a ground acceleration of 0.01 (a, b, c) and 0.015 (d, e, f). The response of S_1 is denoted by black lines, the response of S_2 (when $Y = Z_m, y_s = 0.2$) by red lines while the response of S_3 by magenta ($\tilde{K}_n = 0.5\alpha$), violet ($\tilde{K}_n = \alpha$) and blue lines ($\tilde{K}_n = 1.2\alpha$), respectively. The dashed lines indicate unstable periodic responses.

Besides the negative stiffness coefficient, also the nonlinear stiffness coefficient $\tilde{K}_3$ plays an important role on the nonlinear dynamic response. Figure 4.2 shows families of displacement and acceleration FRCs of the systems S_1 and S_3 upon variation of the nonlinear stiffness coefficient $\tilde{K}_3$. Note that an increase of $\tilde{K}_3$, associated with a smaller working displacement $\tilde{x}_f$, entails a stronger hardening nonlinearity that leads to a reduction of the peak displacement and an increase of the peak acceleration.

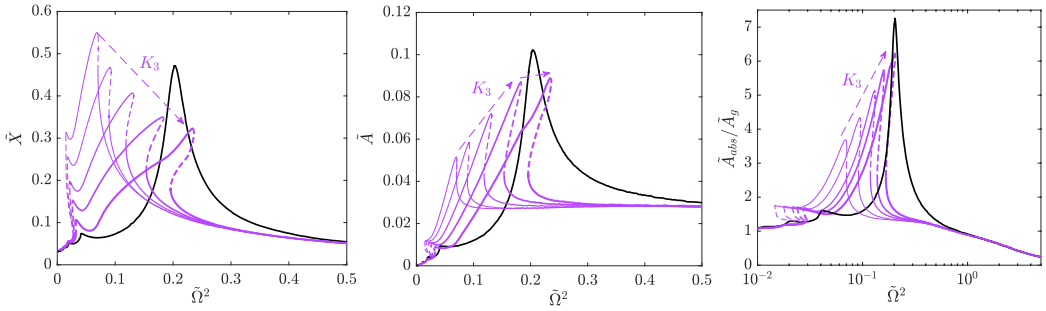

Figure 4.2: Frequency-response curves (FRCs) in terms of nondimensional displacement (left), acceleration (center), and force transmissibility for a ground acceleration set to 0.015. The response of S_1 is represented by black lines and that of S_3 (when $Y = Z_m, y_s = 0.2, \tilde{K}_n = \alpha$ and $\tilde{K}_3 = -(1,2,4,8,10)\tilde{K}_n$) is denoted by solid violet lines with increasing thickness for increasing $\tilde{K}_3$.

4.1.2 SMA mechanical characteristics

In Fig. 4.3, the FRCs of the system S_1 (black lines) are compared with those of S_2 (red lines) and S_3 (violet lines) for different levels of hysteresis ratio y_s and for two excitation amplitudes, $\tilde{A}_g = (0.01, 0.015)$. The acceleration of the system S_2 shows, for low excitations and regardless of the hysteresis ratio, an increase of the acceleration compared to the baseline system S_1. On the contrary, S_3 exhibits a strong reduction in accelerations for both excitation amplitudes while it also undergoes a strong reduction in displacements for medium and high hysteresis ratios of the superelastic element. For both the systems S_2 and S_3 an increase of hysteresis ratio y_s produces an improvement of the performance, mild at low amplitudes and more consistent at high amplitudes. The peak of force transmissibility for S_2 configuration is reduced from 3.3 ($y_s = 0.2$) to 2.8 ($y_s = 0.8$) at the lower amplitude and from 6.1 to 3 at the higher amplitude. Instead, the S_3 configuration exhibits a reduction of force transmissibility peak from 1.8 to 1.5 at the lower amplitude and from 4 to 1.4 at the higher amplitude. By increasing the yielding force of the superelastic element (with $Y = 1.6Z_m$), an additional reduction of displacement amplitude can be achieved but paying the cost of a stiffness increase and, accordingly, of the accelerations transmissibility. This deterioration of performances is stronger at low amplitudes, where the increase of stiffness is greater. In fact, the peak of force transmissibility grows from 1.5 to 2.3 at the lower amplitude, while for the higher amplitude goes from 1.4 to 1.8.

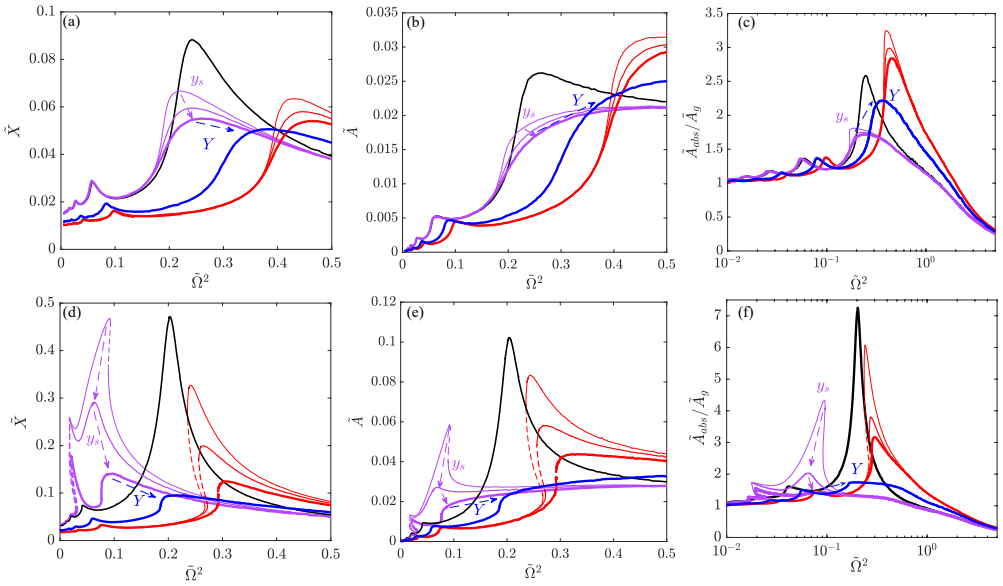

Figure 4.3: Frequency-response curves (FRCs) in terms of nondimensional displacement (left), acceleration (center), and force transmissibility for a ground acceleration of 0.01 (a, b, c) and 0.015 (d, e, f). The response of the S_1-isolated system is described by black lines, those of S_2 (when $Y = Z_m, y_s = (0.2, 0.5, 0.8)$) by red lines with increasing thickness for increasing y_s, and those of S_3 (when $\tilde{K}_n = \alpha, Y = Z_m, y_s = (0.2, 0.5, 0.8)$) by violet lines with increasing thickness for increasing y_s and blue lines (when $\tilde{K}_n = \alpha, Y = 1.6Z_m, y_s = 0.8$), respectively.

4.2 Nonlinear dynamic scenarios

The parametric study unfolds a meaningful sensitivity of the frequency-response with respect to the system parameters. Henceforth, the evolution of the response for increasing base accelerations is discussed. The FRCs of the system S_3, set in two different Snap-Through configurations, are computed for different excitation amplitudes and are showed in Fig. 4.4. The strong softening-hardening nonlinearity of the system is reflected by the trend of the backbone curves, that bend firstly to the left and then to the right. The severe curvature of the backbone curves cause different nonlinear phenomena, such as Jumping phenomena both to the left (softening) and to the right (hardening) of the main resonance frequency. Other interesting phenomena are observed such as the emergence of detached resonance curves. For the case with large negative stiffness ($\tilde{K}_n = 1.2\alpha$) a disappearance of the peak occurs in the response within the displacement range in which the system turns out to be overdamped ($0.2 < \tilde{x} < 0.4$). Moreover, for the strongest base acceleration in the low frequency range, there exists a bandwidth in which no

stationary solutions could be obtained, a circumstance that suggests the existence of quasi-periodic/nonperiodic responses. All these features persist in the response of Tri-Stable configurations and are enriched and complexified by the presence of the two additional lateral equilibria.

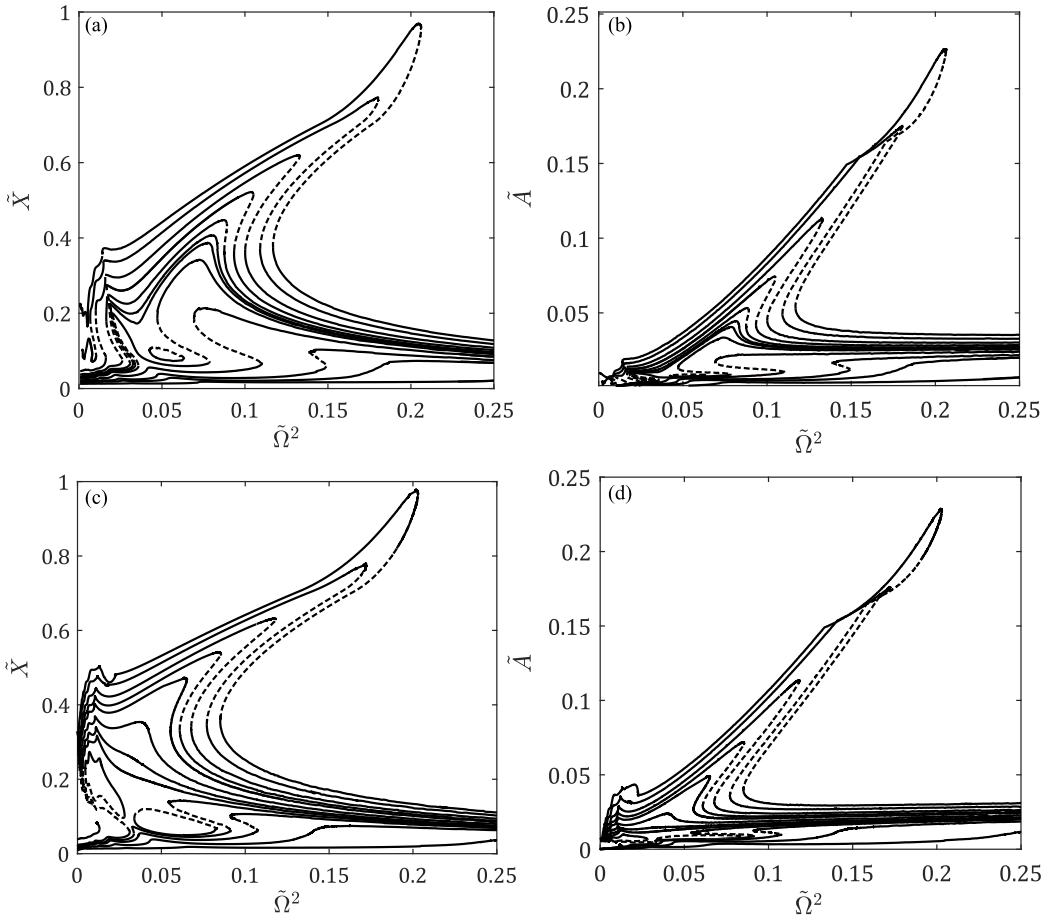

Figure 4.4: FRCs in terms of nondimensional displacement (left) and acceleration (right) for the S_3 system with $\tilde{K}_n = \alpha, \tilde{K}_3 = -2\tilde{K}_n, Y = Z_m, y_s = 0.2$ (top) and with $\tilde{K}_n = 1.2\alpha, \tilde{K}_3 = -2\tilde{K}_n, Y = Z_m, y_s = 0.2$ (bottom) when the base accelerations are set to $(0.8, 1, 1.08, 1.2, 1.28, 1.3, 1.32, 1.36, 1.4, 1.48, 1.6, 1.8, 2)10^{-2}$.

4.2.1 Primary, superharmonic and detached resonances

The severe softening nonlinearity associated with the softening hysteresis induces an interaction between the primary and the superharmonic resonances causing the emergence of detached resonance curves, a phenomenon that is well documented

in the literature [135, 136, 137]. However, a new phenomenology is here documented. Figure 4.5 show the evolution of the isolas for the system with two levels of negative stiffness associated with ST configurations.

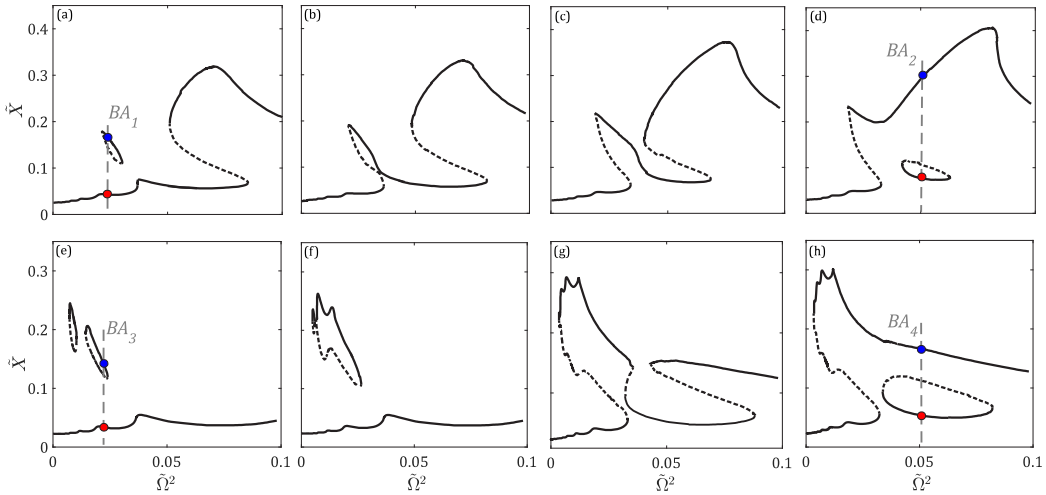

Figure 4.5: Evolution of isolas topology for S_3 with $\tilde{K}_n = \alpha, \tilde{K}_3 = -2\tilde{K}_n, Y = Z_m, y_s = 0.2$ (top) for a nondimensional ground acceleration equal to 0.0128 (a), 0.01288 (b), 0.0130 (c), 0.0132 (d) and for S_3 with $\tilde{K}_n = 1.2\alpha, \tilde{K}_3 = -2\tilde{K}_n, Y = Z_m, y_s = 0.2$ (bottom) for a nondimensional ground acceleration equal to 0.01072 (e), 0.01088 (f), 0.01112 (g) and 0.0112 (h).

The qualitative pattern in both cases consists in the birth of an outer isola in the neighborhood of the superharmonic resonance frequency which, for increasing base acceleration levels, coalesces first with the superharmonic resonance branch and, thereafter, upon further increase of the excitation amplitude, coalesces with the main resonance branch, giving rise to an inner isola. It is possible to observe that for the system S_3 with $\tilde{K}_n = \alpha$, there exists only a small outer isola, while for the case with $\tilde{K}_n = 1.2\alpha$, different outer isolas coexist. Indeed, for a ground acceleration of 0.01, two outer detached resonance isolas are visible in the proximity of the superharmonic resonances of order 1:3 and 1:5 (see Fig. 4.5e). For a higher amplitude, the two distinct isolas merge and a new isola is formed near the superharmonic resonance of order 1:7 (see Fig. 4.5f). Upon further increase of the excitation amplitude, all previous isolas merge with each other and with the 1:3 superharmonic resonance branch (see Fig. 4.5g). At a higher excitation amplitude, the primary resonance branch and the outer superisola merge and give rise to an inner isola for slightly higher excitation amplitudes (see Fig. 4.5h). Despite the very low frequency range where the isolas appear, the outer isolas are detrimental for isolation purposes since they can give rise to an unwanted dynamic amplification. On the contrary, the inner isola can be used to reduce the main resonance.

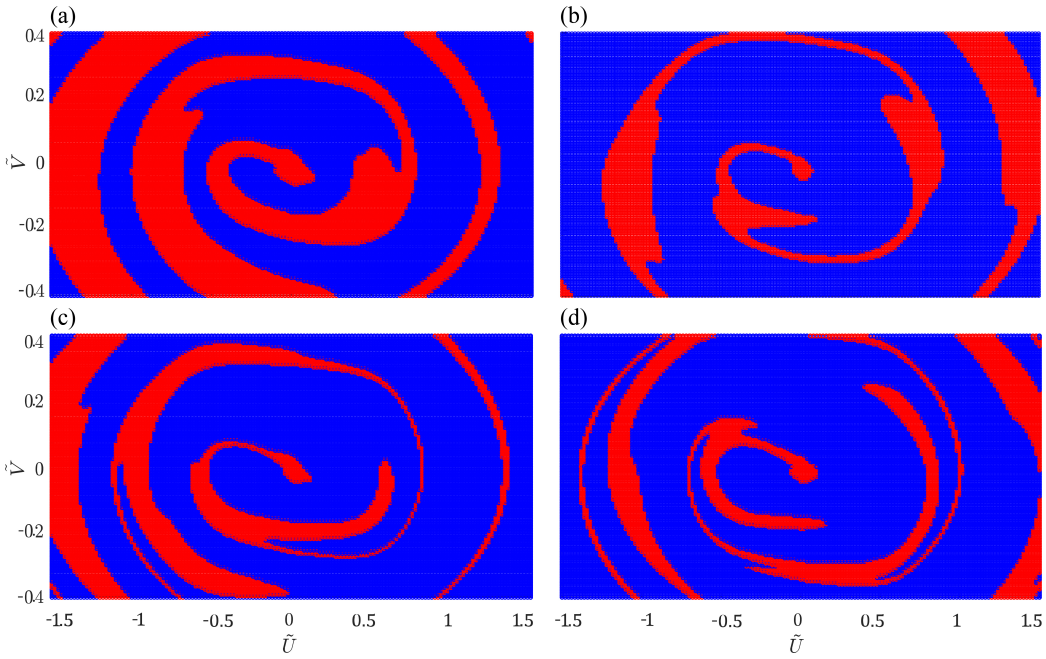

Figure 4.6: Basins of attraction for the system S_3 with $\tilde{K}_n = \alpha, \tilde{K}_3 = -2\tilde{K}_n, Y = Z_m, y_s = 0.2$ (top) for a base acceleration $\tilde{A}_g = 0.0128$ and frequency $\tilde{\Omega}^2 = 0.022$, corresponding to the outer isola (left), and for a base acceleration $\tilde{A}_g = 0.0132$ and frequency $\tilde{\Omega}^2 = 0.05$, corresponding to the inner isola (right). (bottom) Basins of attraction for the system S_3 with $\tilde{K}_n = 1.2\alpha, \tilde{K}_3 = -2\tilde{K}_n, Y = Z_m, y_s = 0.2$ for a base acceleration of $\tilde{A}_g = 0.01072$ and $\tilde{\Omega}^2 = 0.022$, corresponding to the outer isola (left), and for a base acceleration of $\tilde{A}_g = 0.0112$ and $\tilde{\Omega}^2 = 0.05$, corresponding to the inner isola (right). In red, the initial conditions that lead to the low-amplitude solution, while in blue those that lead to the high-amplitude solution.

The factors that determine whether the mass will move along the detached solution curve or along the main branch are the initial conditions or the perturbations causing jumps between the coexisting attractors. In order to obtain the basins of attraction of the system for the isolas (see Fig. 4.6), the equations of motion are numerically integrated for a fixed harmonic excitation over 1,000 periods for a grid of initial conditions. The initial conditions, in terms of displacement and velocity, that lead to different attractors are denoted by different colors. In particular, the initial conditions that lead to the low-amplitude solution are represented in red, while in blue those associated with the high-amplitude solution. It is possible to note that the system with $\tilde{K}_n = \alpha$ shows much thinner basins of attraction for both the outer and inner isola than the system with $\tilde{K}_n = 1.2\alpha$, denoted by larger blue and red regions for the outer and inner isolas, respectively. For a more thor-

ough characterization of the two coexisting attractors exhibited by the system with $\tilde{K}_n = 1.2\alpha, Y = Z_m, y_s = 0.2$, the force-displacement cycles, the phase portraits, the time histories and the FFTs of the response for a harmonic base excitation with $\tilde{A}_g = 0.01072$ and $\tilde{\Omega}^2 = 0.022$ are shown in Fig. 4.7.

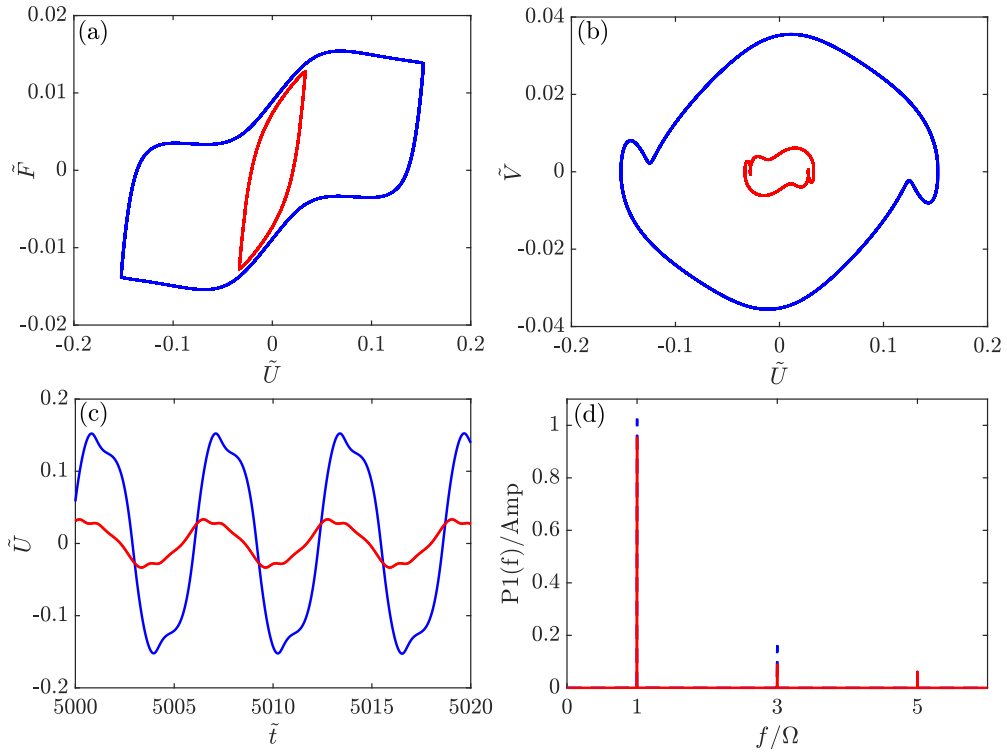

Figure 4.7: Force-displacement cycles (a), phase portraits (b), time histories (c) and FFTs (d) of the system S3 (with $\tilde{K}_n = 1.2\alpha, \tilde{K}_3 = -2\tilde{K}_n, Y = Z_m, y_s = 0.2$) for $\tilde{A}_g = 0.01072$ and $\tilde{\Omega}^2 = 0.022$. In red the response to a zero initial condition along to the main solutions branch, while in blue the solution for the initial conditions $\tilde{x} = 0.2, \tilde{v} = 0$, giving rising to the isola solution curve.

The response belonging to the main solution branch is richer due to the presence of more superharmonic components. In fact, while in the first case, third, fifth and seventh harmonics are relevant in terms of amplitude, in the case of the isola, only the third harmonic is considerable. From the FFT it is also possible to see that, for solutions belonging to the isola, the amplitude of the main harmonic is larger than that of the overall response (sum of all harmonics) while for the solution along the main curve, the fundamental harmonic exhibits the same amplitude of the overall response. This suggests a different relative phase between the main harmonic and higher harmonics for the two solutions. The harmonic decomposition of the two

different responses shows that for the solution belonging to the main branch, the peak of main harmonic component corresponds to the zero of all other harmonics having thus a relative phase of $\pi/2n$ with n representing the order of the harmonic component (see Fig. 4.8).

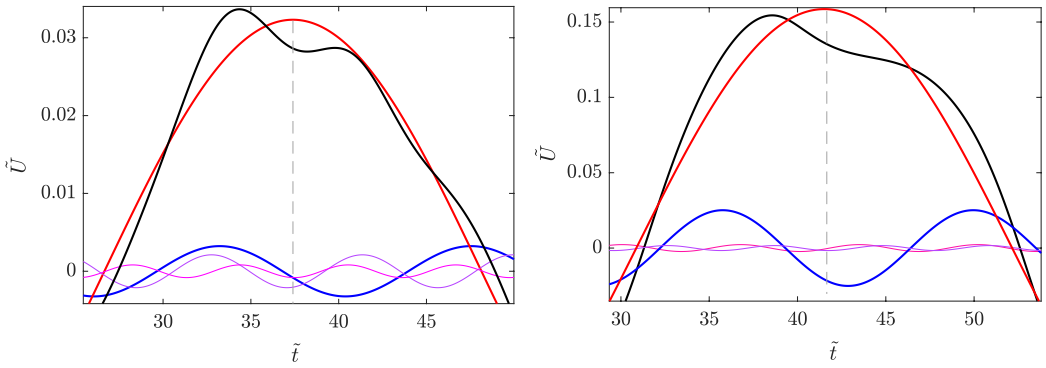

Figure 4.8: Harmonic decomposition of the superharmonic response along the main resonance branch (left) and detached resonance (right). The first, third, fifth and seventh harmonics and the total response are represented by red, blue, violet, magenta and black lines, respectively.

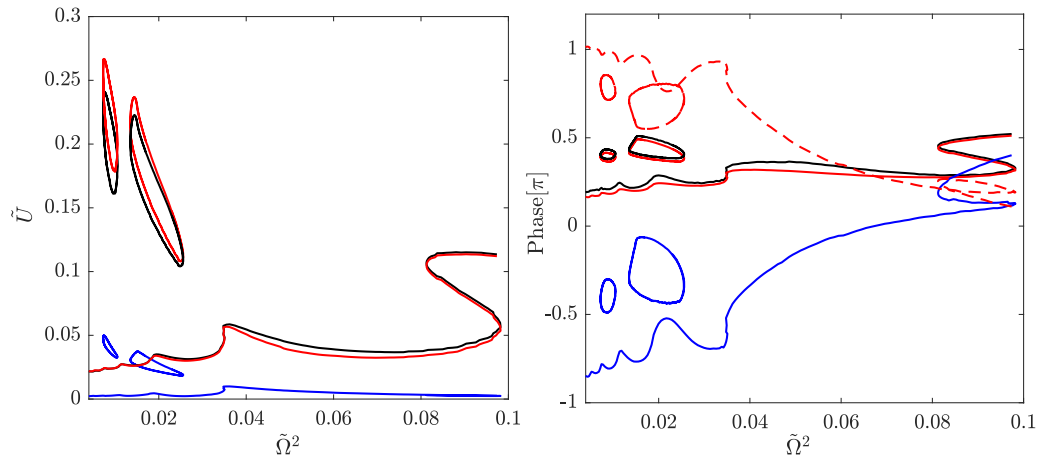

Figure 4.9: Nondimensional displacement (left) and phase angle (right) vs. nondimensional frequency for S_3 with $\tilde{K}_n = 1.2\alpha, \tilde{K}_3 = -2\tilde{K}_n, Y = Z_m, y_s = 0.2$ and $\tilde{A}_g = 0.01072$. Black lines show the amplitude and phase angle of the overall response, red lines and blue lines represent the amplitude and phase angle of the main harmonic and of the first superharmonic of order 1:3, respectively. The phase angle between the main harmonic and the first superharmonic is reported in red dashed lines.

By focusing on the third harmonic, a relative phase of $\pi/6$ means that the peak of the main harmonic coincides with the zero value along the descending branch of the superharmonic and this is equivalent to the out-of-phase condition or deamplification condition. On the other hand, the solution along the detached curve shows that the peak of the main harmonic coincides with the minimum of the third harmonic, thus giving rise to a $\pi/2$ relative phase. Thus, for the solutions belonging to the detached curve, the higher harmonics are phased with the main harmonic, producing a less distorted and larger motion. Figure 4.9 shows the amplitudes and the phases of the overall response, of the main harmonic and of the first superharmonic and the relative phase between the main harmonic and the first superharmonic in the frequency domain. Note that the main harmonic of the solution belonging to the detached resonance curve shows a phase equal to $\pi/2$ at the peak. This condition is shared only with the solution of the primary resonance.

4.2.1.1 Tri-Stable configurations response

The detached resonance curves descrived above, exhibited by ST configurations, are mainly due to the progressive emerging of the unstable equilibrium, which expand the motion of the mass. As shown, isolas come out at low frequencies range, where the oscillator, under certain initial values of displacement and velocity, establish an in-phase motion with the ground excitation. A different scenario unfolds for TS configurations, where the existence of multiple stable equilibria allows the mass to oscillate stably around one or another equilibrium position. This type of intra-well motions is manifested for low excitation amplitudes, where the incoming energy is not sufficient to escape the mass from the wells. For higher excitation amplitudes, the mass is able to escape and the motion involves all the equilibrium (inter-wells).
In Fig. 4.10 the FRCs of the TS configuration with $\tilde{K}_n = 1.4\alpha, \tilde{K}_3 = -2\tilde{K}_n, Y = Z_m, y_s = 0.2$ are shown for two levels of excitation amplitudes ($\tilde{A}_g = 0.01, 0.015$). For the lower amplitude two distinct and stable intra-well solutions exist, one around the central equilibrium and the other around the laterals equilibria with ascissa $\tilde{x}_{f0u}$. As shown in Fig. 4.11, while the central solution is symmetric, the lateral solution reveals an asymmetric motion, highlighted by the presence of even super-harmonics (see Fig. 4.11d). For the higher excitation amplitude the intra-well motions endure only for high frequencies range. In fact, at the frequency $\tilde{\Omega}^2 = 0.18$ the central solution crosses the position of unstable equilibrium and the motion, for lower frequencies, expands towards inter-well orbits. In this expansion process the simmetry of motion is broken by the near presence of lateral equilibria, producing a loss of stationarity in response for the frequencies range $0.04 < \tilde{\Omega}^2 < 0.18$ (dashed line of inter-well motion in Fig. 4.10d). For lower frequencies the mass establishes high energy inter-wells orbits and regain station-

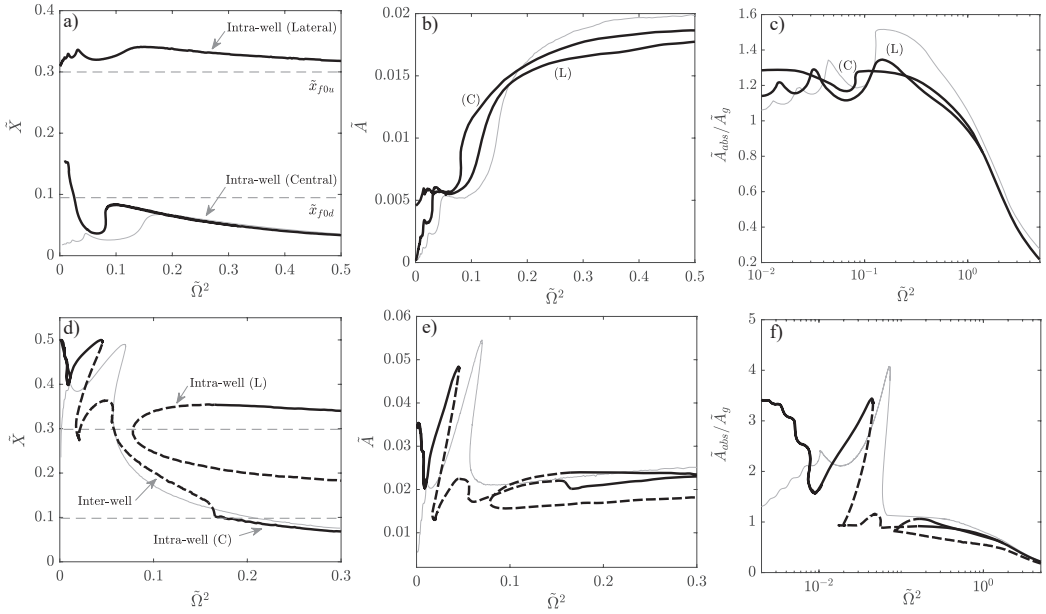

Figure 4.10: Frequency-response curves (FRCs) in terms of nondimensional displacement (left), acceleration (center), and force transmissibility for a ground acceleration of 0.01 (a, b, c) and 0.015 (d, e, f) of S_3 configuration with $\tilde{K}_n = 1.4\alpha, \tilde{K}_3 = -2\tilde{K}_n, Y = Z_m, y_s = 0.2$. The dashed lines indicate unstable periodic responses.

arity. This type of orbits causes an amplification of accelerations transmissibility for low frequencies compared with the configuration with $\tilde{K}_n = 1.2\alpha$ (see Fig. 4.10f) For both excitation amplitudes, the lateral intra-well solutions show a higher force transmissibility with respect to the central intra-well solution because of the more developed cubic stiffness. Also in this case, the factor that determines the equilibrium around which the mass vibrates are the initial conditions, in terms of initial displacement and velocity. In Fig. 4.12 the basins of attraction of the shown TS configuration are reported for $\tilde{A}_g = 0.01$ at $\tilde{\Omega}^2 = 0.09, 0.3$. For the lower frequency, corresponding to the main resonance in the central solution, a greater attraction of the central equilibrium is observed compared with the attraction exhibited by the lateral equilibria. On the other hand, when $\tilde{\Omega}^2 = 0.3$, the area covered by the lateral solution, hence their attraction, is greater than the one of the central equilibrium.

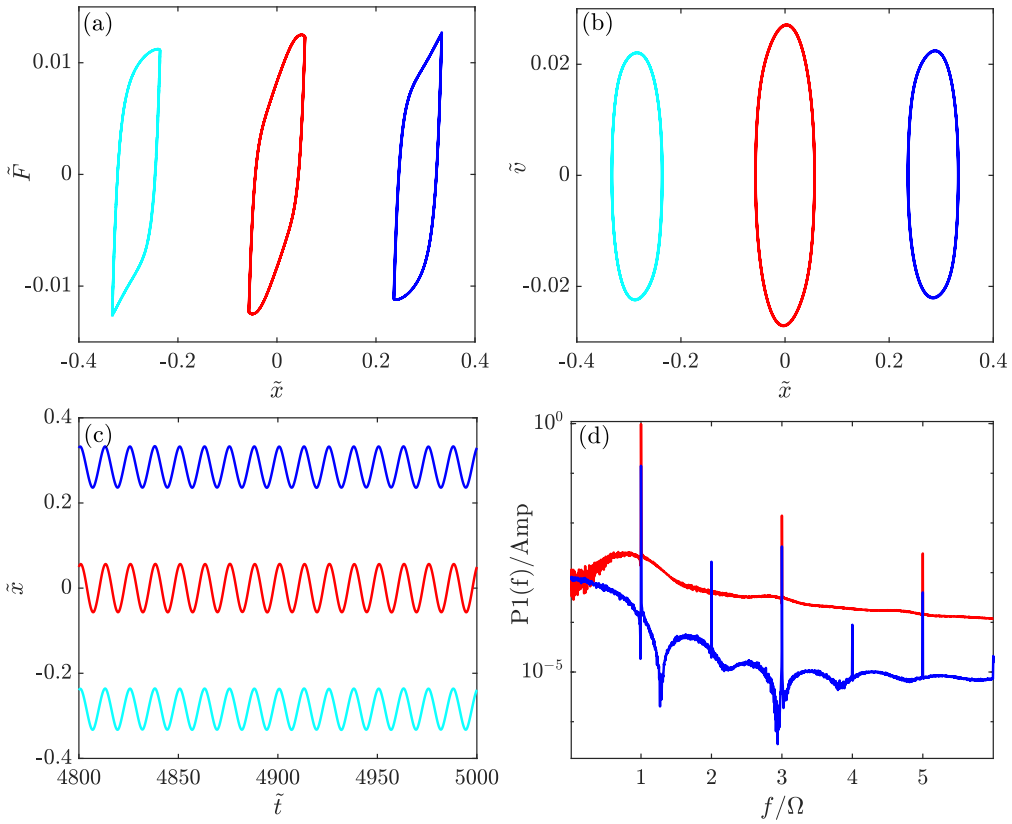

Figure 4.11: Force-displacement cycles (a), phase portraits (b), time histories (c) and FFTs (d) of the system S_3 with $\tilde{K}_n = 1.4\alpha, \tilde{K}_3 = -2\tilde{K}_n, Y = Z_m, y_s = 0.2$ for $\tilde{A}_g = 0.01$ and $\tilde{\Omega}^2 = 0.3$. In red the response along to the central solutions branch, while in blue the solution along the lateral solutions curve.

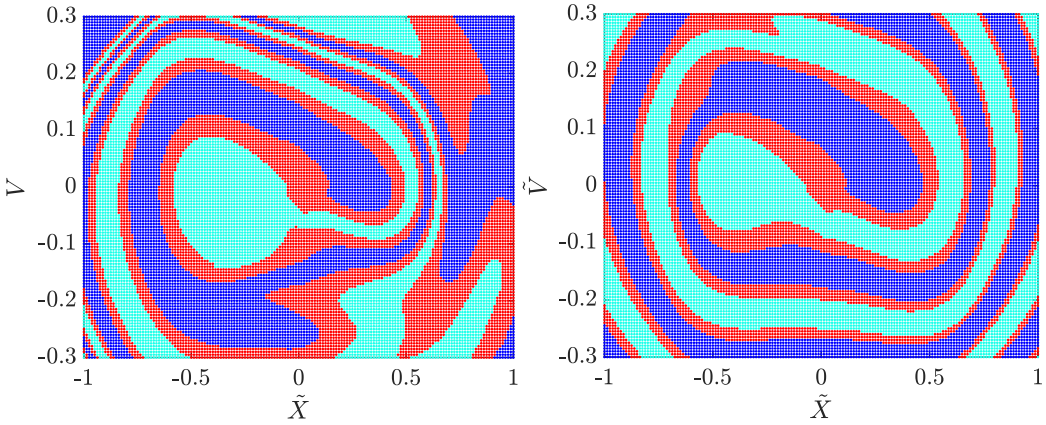

Figure 4.12: Basins of attraction of the system S_3 with $\tilde{K}_n = 1.4\alpha, \tilde{K}_3 = -2\tilde{K}_n, Y = Z_m, y_s = 0.2$ for $\tilde{A}_g = 0.01$ and $\tilde{\Omega}^2 = 0.09$ (left), 0.3 (right). In red the initial conditions leading to to the central solutions, while in blue and green those leading to the lateral solutions.

4.2.2 Bifurcation scenarios and quasi-periodicity

As mentioned above, for low frequencies and high base accelerations, the periodic response of the system S_3 with $\tilde{K}_n = 1.2\alpha$ and $\tilde{K}_3 = -2\tilde{K}_n$ undergoes a loss of stability. By restricting our analysis to the frequency range reported in Fig. 4.13, a rich sequence of bifurcations is found. Moving from low to high frequencies, the first encountered bifurcation is a Neimark-Sacker or secondary Hopf bifurcation (A), signalled by a pair of Floquet multipliers crossing the unit circle away from the real axis (red circles). The solution emerging out of the Neimark-Sacker bifurcation is a quasi-periodic solution. However, past the bifurcation, the continuation of the unstable periodic solution cannot be successfully achieved. On the other hand, between C and D, a stable branch of periodic solutions is found, which loses its stability at C due to a symmetry-breaking bifurcation. The two branches of mirror nonsymmetric periodic attractors lose their stability at B due to a period-doubling bifurcation, circumstance indicated by the fact that one of the Floquet multipliers crosses the unit circle through -1.

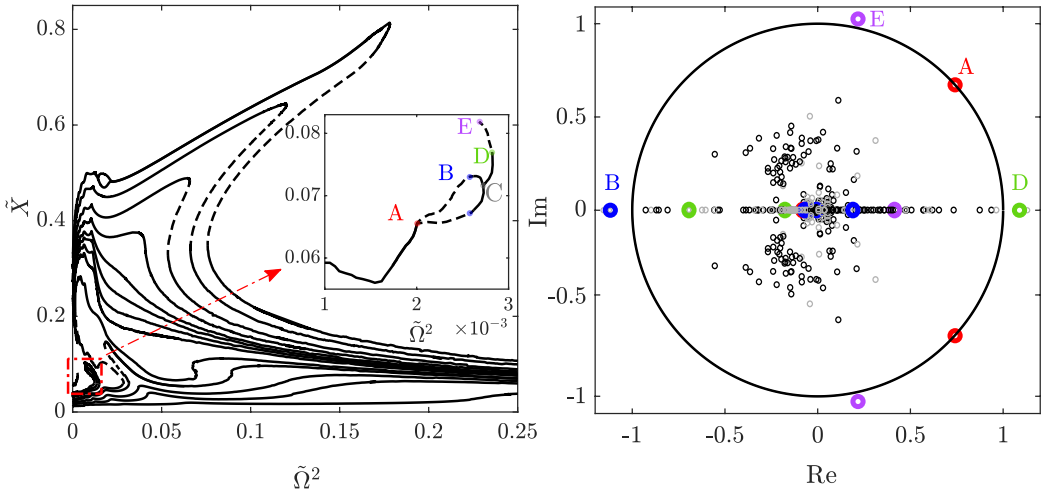

Figure 4.13: FRCs of the system S_3 with $\tilde{K}_n = 1.2\alpha, \tilde{K}_3 = -2\tilde{K}_n, Y = Z_m, y_s = 0.5$ for a nondimensional ground acceleration equal to $\tilde{A}_g = 0.0148$ (left) and imaginary parts vs. real parts of Floquet multipliers (right).

In D the solution experiences a fold bifurcation, whereby one of the Floquet multipliers crosses the unit circle along the positive real axis. Finally, in E a new Neimark-Sacker bifurcation is manifested and afterwards path following of the stationary solutions breaks down. To investigate more in depth the scenario between the Neimark-Sacker bifurcation at A and the period-doubling at B, bifurcation diagrams were constructed by direct numerical integration of the equations of motion (see Fig. 4.14). The time step was fixed by dividing the excitation pe-

riod into 4,096 equally spaced points. The integration was carried out over 2,000 cycles of the excitation by considering as initial conditions those obtained at the previous excitation frequency and the last 64 points of the Poincaré map were recorded.

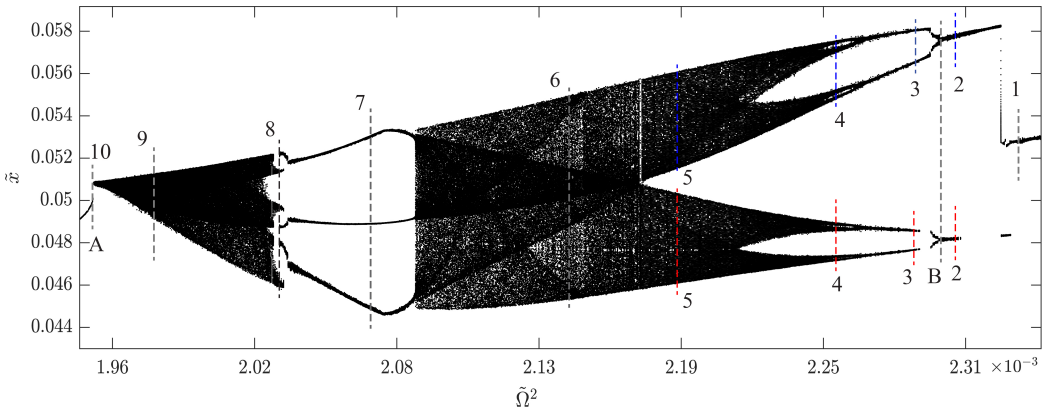

Figure 4.14: Bifurcation diagram for the system with $\tilde{K}_n = 1.2\alpha, \tilde{K}_3 = -2\tilde{K}_n, Y = Z_m, y_s = 0.5$ for a nondimensional ground acceleration equal to $\tilde{A}_g = 0.0148$.

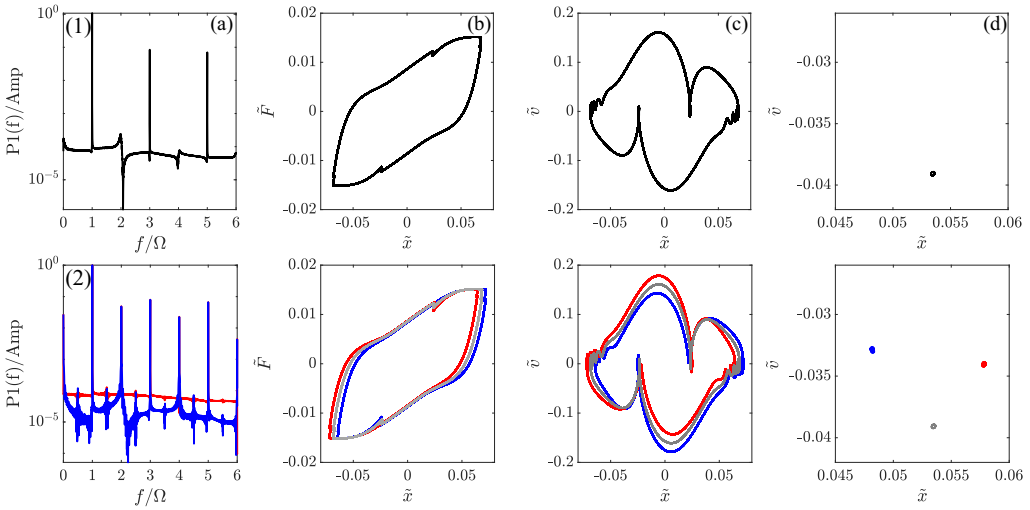

Figure 4.15: FFTs of the response (a), force-displacement cycles (b), phase portraits (c) and Poincarè map (d) of the system S_3 when $\tilde{K}_n = 1.2\alpha, \tilde{K}_3 = -2\tilde{K}_n, Y = Z_m, y_s = 0.5$, the nondimensional ground acceleration is set to $\tilde{A}_g = 0.0148$ for the frequencies corresponding to sections 1, 2.

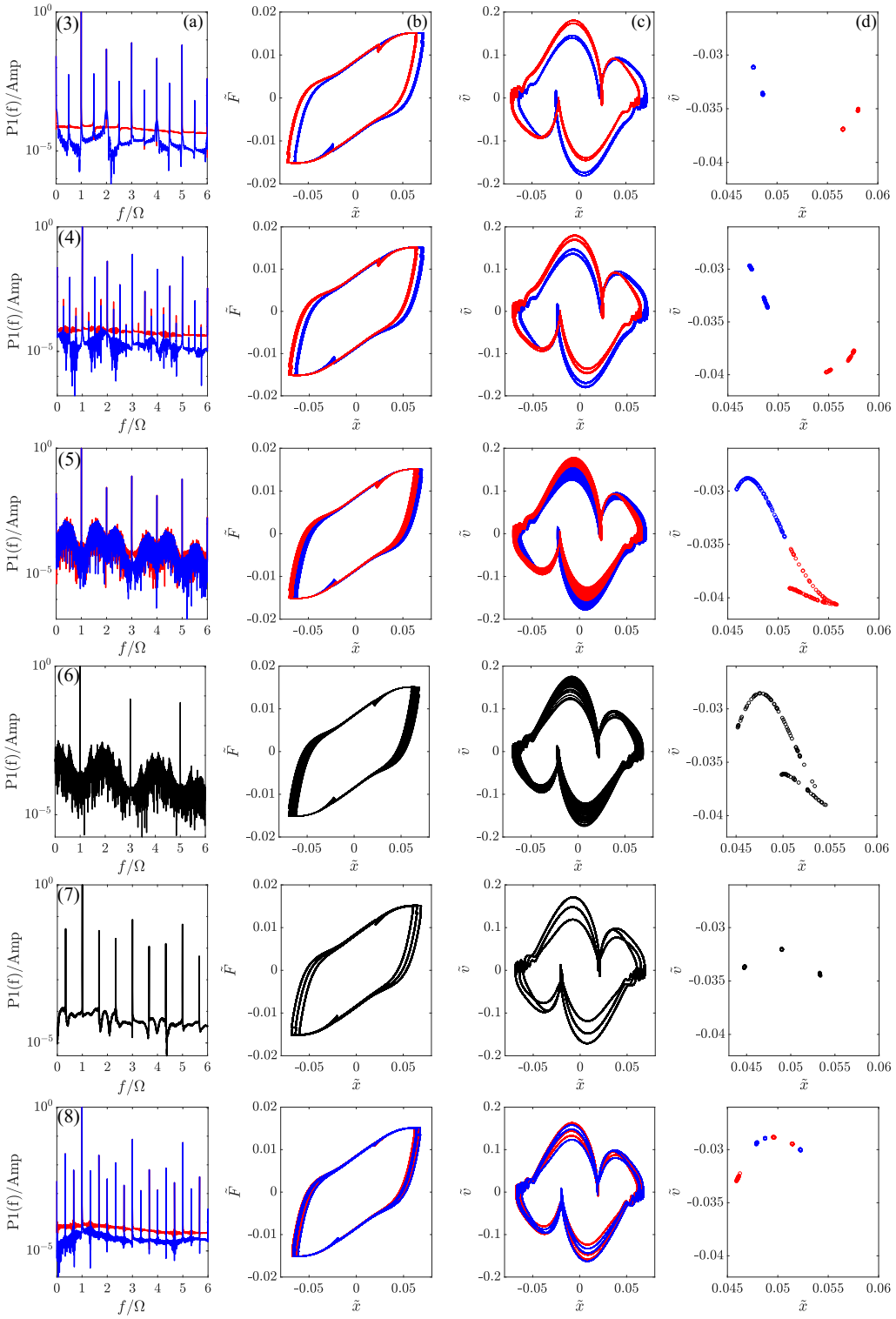

Figure 4.16: FFTs of the response (a), force-displacement cycles (b), phase portraits (c) and Poincarè map (d) of the system S_3 when $\tilde{K}_n = 1.2\alpha, \tilde{K}_3 = -2\tilde{K}_n, Y = Z_m, y_s = 0.5$ for a nondimensional ground acceleration equal to $\tilde{A}_g = 0.0148$ for the frequencies referred to as 3, 4, 5, 6, 7, 8 in Fig. 4.14.

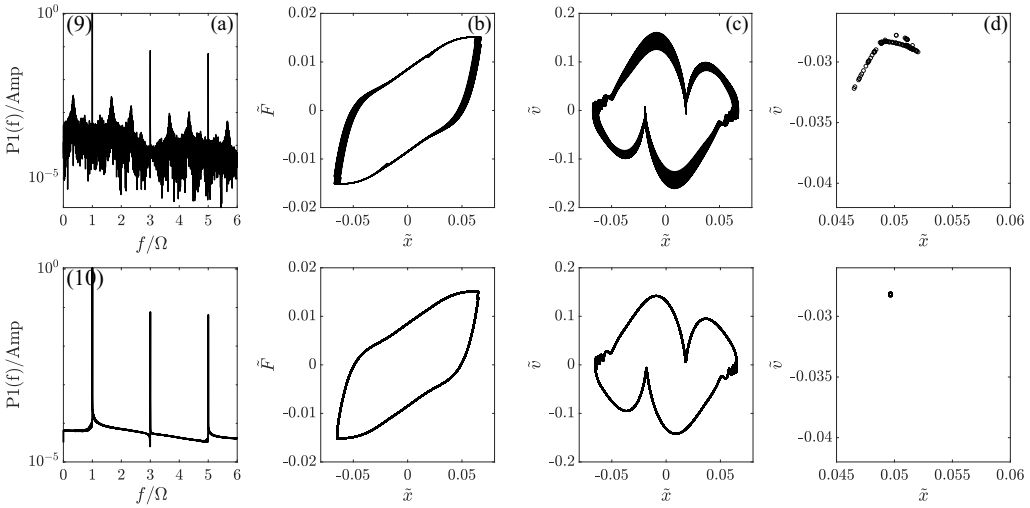

Figure 4.17: FFTs of the response (a), force-displacement cycles (b), phase portraits (c) and Poincarè map (d) of the system S_3 when $\tilde{K}_n = 1.2\alpha, \tilde{K}_3 = -2\tilde{K}_n, Y = Z_m, y_s = 0.5$ for a nondimensional ground acceleration equal to $\tilde{A}_g = 0.0148$ for the frequencies referred to as 9 and 10 in Fig. 4.14.

It is possible to note that at A the solution becomes quasiperiodic, through the mentioned secondary Hopf bifurcation, while from B to the left the solution becomes quasi-periodic by means of a more complex sequence of bifurcations. Figure 4.15 shows a symmetry-breaking bifurcation at the frequency denoted by section 2 (see Fig. 4.14), singled out by the birth of an even superharmonic component, after the limit cycle exhibited at section 1. This symmetry-breaking paves the way to two distinct branches of nonsymmetric mirror solutions, whose orbits include the limit cycle and towards the latter they extend.In this frequency range, the solution turns out to jump from one nonsymmetric branch to the other for any small frequency variation. Each of these branches undergoes a cascade of successive period-doubling bifurcations induced by the birth of a subharmonic component of order 2:1 at section 3 and of subharmonics of order 4:1 and 2:1 at section 4. This cascade of period-doubling bifurcations, giving rise to a rich nidification of subharmonics and superharmonics, may lead to a chaotic attractor. When the orbits of the nonsymmetric solutions touch the orbit of the limit cycle, there is a reverse symmetry-breaking and the solution regains symmetry. This is signalled by the disappearance of the even superharmonic component (section 6). In the frequency range between 2.04 and 2.09, the ratio between the modulation frequency and the carrier frequency locks into a rational number, due to the so-called frequency-locking phenomenon with three-period motions, supported by the 3:1 subharmonic component (section 7). Past this window, a new symmetry-breaking is experienced by the 3-T solution, yielding two distinct branches of

3-T solutions in which, in addition to the 3:1 subharmonic, there appears an even superharmonic of order 1:2 (section 8). The symmetry-breaking forces the solution to transition towards a quasiperiodic, symmetric solution regime (section 9). Finally, the amplitude of the phase plane portion covered by the trajectory progressively gets reduced until reaching the frequency indicated by 10, where a reverse secondary Hopf bifurcation makes the solution stable.

4.2.2.1 Bifurcation scenarios for the tri-stable configuration

For $\tilde{K}_n = 1.2\alpha$ and $\tilde{K}_3 = -2\tilde{K}_n$, the bifurcation scenario engages only ultra-low frequencies and a small displacements range. On the other hand, when $\tilde{K}_n > 1.2\alpha$, the bifurcation scenario involves much larger ranges of frequencies and displacements. As shown, for $\tilde{K}_n > 1.2\alpha$ the system is tri-stable and the presence of the two lateral attractors breaks the symmetry of the response. Because of the existence of symmetry-breaking and period-doubling bifurcations, the response is quasi-periodic for most of the frequencies within the considered range. In order to obtain the FRC and bifurcation diagram of the tri-stable configuration (i.e., $\tilde{K}_n = 1.4\alpha$), the equations of motion are numerically integrated for a harmonic base excitation over 1,000 periods and the maximum amplitudes exhibited in the last 50 cycles, together with the Poincaré sections, are recorded for each frequency within the range (see Fig. 4.18). Depending on the initial conditions, the mass can vibrate around the origin, the left or the right equilibrium positions. Regardless of the equilibrium around which the mass vibrates, the adjacent attractor breaks the symmetry of the response and leads to quasi-periodicity. Further, when the mass vibrates around one of the lateral equilibria, due to the stronger effects of the cubic stiffness, the acceleration transmissibility is higher compared with that exhibited by the mass vibrating around the origin. For limited frequency intervals, the phase-locking phenomenon is observable together with a reduction of transmissibility with respect to the adjacent quasi-periodic response. By analysing more in depth the response in Fig. 4.18, we can note that for low frequencies ($0 < \tilde{\Omega}^2 < 0.022$), the system has sufficient energy to complete symmetric periodic cycles. For higher frequencies ($0.022 < \tilde{\Omega}^2 < 0.042$), because of a folding bifurcation, two different responses are exhibited by the system depending on the initial conditions. The high amplitude response, such as the response of the previous frequency range, exhibits stable cycles. On the other hand, the low amplitude solution, with a lower associated energy, suffers the attraction of the lateral equilibria and shows a quasi-periodic behavior. By increasing the frequency up to $\tilde{\Omega}^2 = 0.042$, a downward jump occurs together with the birth of two mirrored nonsymmetric solutions, each of which experiences cascades of period-doubling bifurcations. In the frequency range $0.118 < \tilde{\Omega}^2 < 0.18$, the existing solutions regain periodicity and two new mirrored nonsymmetric and quasi-periodic solutions

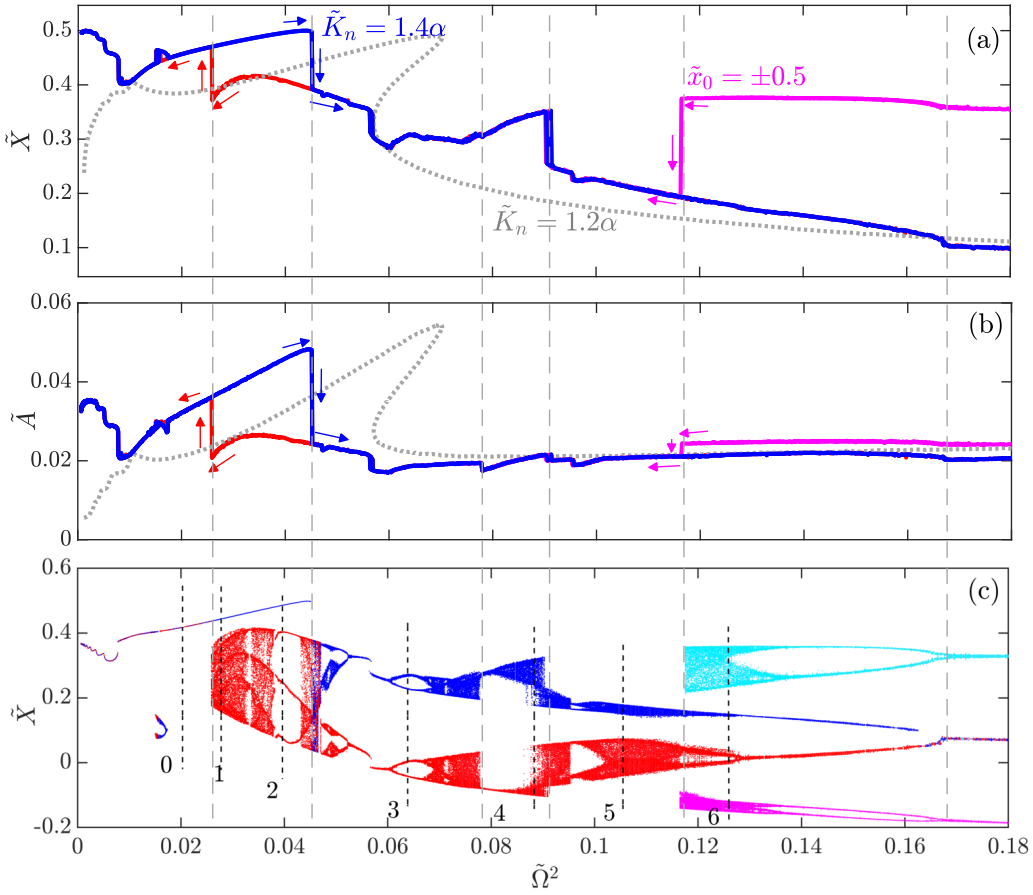

Figure 4.18: FRCs in terms of nondimensional displacements (a) and accelerations (b) and bifurcation diagram (c) for the system S_3 with $\tilde{K}_n = 1.4\alpha, \tilde{K}_3 = -2\tilde{K}_n, Y = Z_m, y_s = 0.2$ for a ground acceleration equal to $\tilde{A}_g = 0.0142$. Blue lines represent the responses obtained for the forward frequency sweep while red lines denote those obtained in reverse sweep. Magenta and cyan lines indicate the responses of the system with initial conditions $\tilde{x}_0 = 0.5$ and of $\tilde{x}_0 = -0.5$, respectively. Finally, for comparative purposes, the responses of the mono-stable system with $\tilde{K}_n = 1.2\alpha$ are represented by gray lines.

appear along the lateral right and left equilibria. Finally, when $\tilde{\Omega}^2 = 0.165$, the first two mirrored solutions coalesce into one symmetric periodic solution while the two lateral nonsymmetric solutions regain stability. In the latter frequency range, an amplification of both accelerations and displacements is observable. In Fig. 4.19 the FFTs, the hysteresis loops, phase portraits and Poincarè maps associated with the frequencies highlighted in Fig. 4.18 are reported. By focusing on section 6, the coexistence of four different types of response is noted.

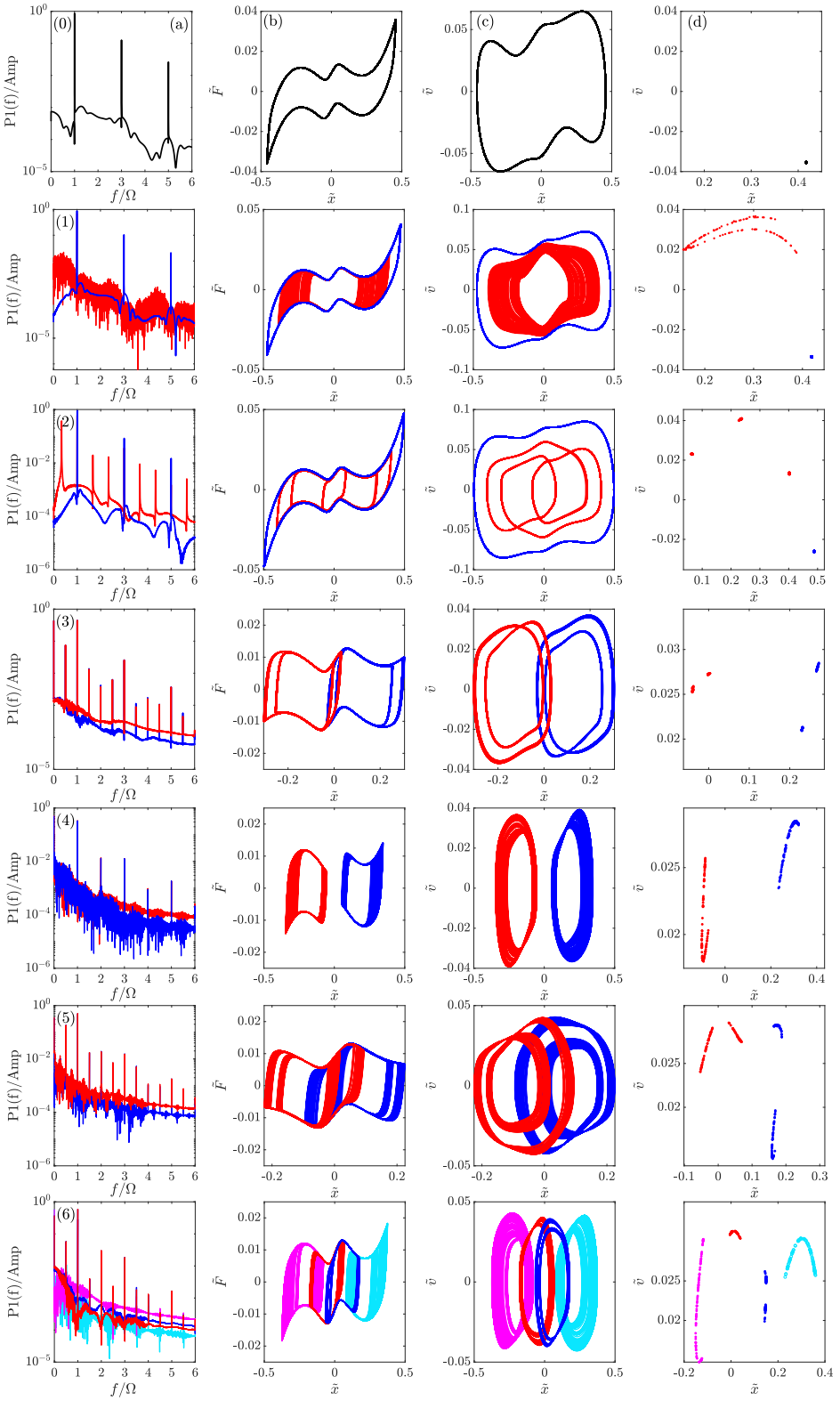

Figure 4.19: FFTs of the response (a), force-displacement cycles (b), phase portraits (c) and Poincarè map (d) of the system S_3 when $\tilde{K}_n = 1.4\alpha, \tilde{K}_3 = -2\tilde{K}_n, Y = Z_m, y_s = 0.2$ and the nondimensional ground acceleration is set to $\tilde{A}_g = 0.0142$ for the frequencies referred to as 0, 1, 2, 3, 4, 5, 6 in Fig. 31.

The basins of attraction obtained for this frequency are reported in Fig. 4.20. The coexistence of four different attractors, namely, the left stable (LS) and unstable (LU) and the right stable (RS) and unstable (RU) equilibria, gives rise to in a high sensitivity of the dynamic response to the initial conditions, as manifested by the richness of the basins. From the progressive zooming of the basins of attraction (see Fig. 4.20c and Fig. 4.20d), it is remarkable that the strict adherence to the attractors succession order (LS, LU, RU, RS) leads to a fractal-like pattern.

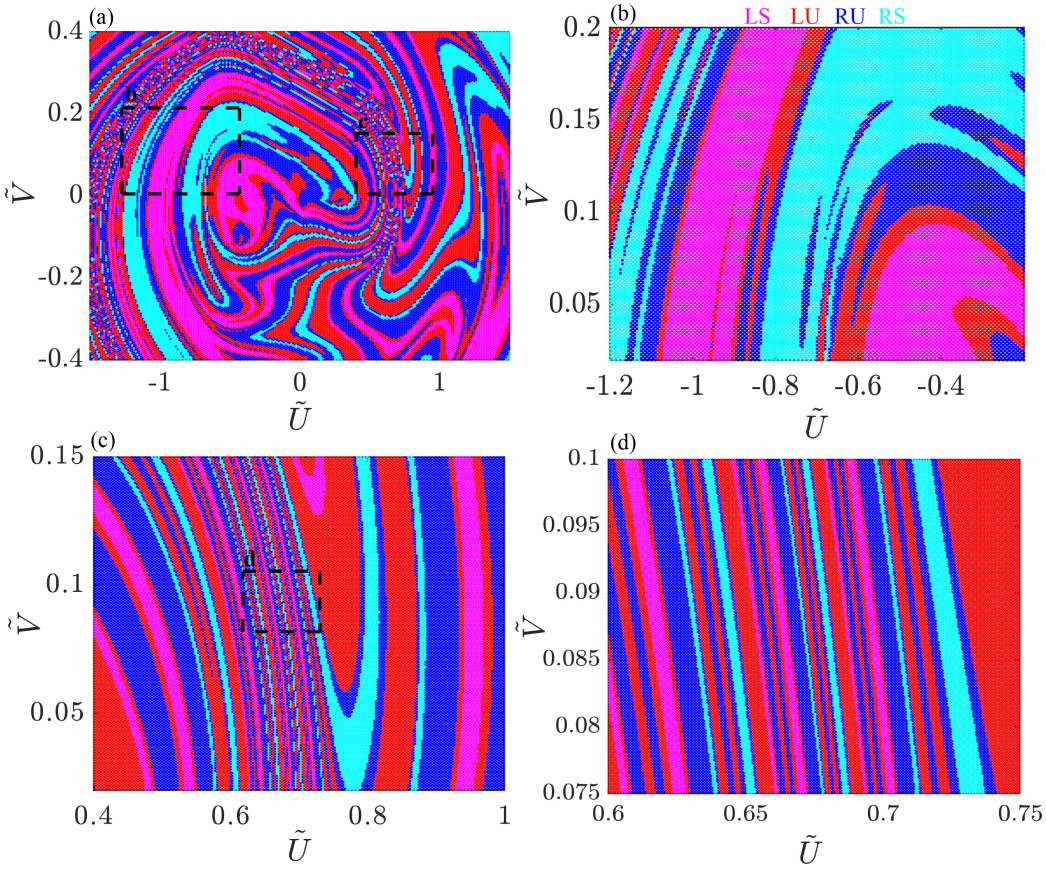

Figure 4.20: (a) Basins of attraction for the system with $\tilde{K}_n = 1.4\alpha, \tilde{K}_3 = -2\tilde{K}_n, Y = Z_m, y_s = 0.2$ for a base acceleration $\tilde{A}_g = 0.0142$ and frequency $\tilde{\Omega}^2 = 0.125$. Parts (b), (c) and (d) are zoomed-in regions bounded by the dashed rectangles. Magenta and red dots denote the initial conditions that lead to the left stable (LS) and unstable (LU) attractors, respectively, while cyan and blue dots represent the initial conditions that lead to the right stable (RS) and unstable (RU) attractors, respectively.

4.3 Displacement and acceleration transmissibility

For the same excitation amplitudes range, the FRCs are computed for the system S_1 and S_2 assuming various hysteresis ratios and yielding force levels, and for S_3 varying the amount of hysteresis and considering three different levels of negative stiffness $\tilde{K}_n = \alpha, 1.2\alpha, 1.4\alpha$, corresponding to MS, ST and TS states, respectively. The peak responses of S_2 or S_3 and those of the baseline system S_1 are reported in Fig. 4.21 as function of the base acceleration. As expected, the insertion of the superelastic element alone (system S_2) causes an increase of accelerations response for weak excitations. The increase is about 30% when $Y = Z_m$ and 60% for $Y = 1.6Z_m$, respectively, and it is mainly due to the initial stiffness of the hysteretic damping and slightly to the damping ratio. On the other hand, the damping ratio strongly affects the response for moderate and strong base accelerations. It turns out that reductions of 20%, 60% and 75% are obtained when $Y = Z_m, y_s = (0.2, 0.8)$ and $Y = 1.6Z_m, y_s = 0.8$, respectively.
By introducing the negative stiffness in parallel with the SMA damper (system S_3), the amplification of accelerations for weak excitations is totally cancelled and a mild reduction can be observed. In addition, a further 20% reduction of accelerations compared with the system S_2 is obtained for moderate and strong base excitations, achieving an overall acceleration reduction of 40% and 80% for $y_s = (0.2, 0.8)$, respectively. Also in the S_3 configuration, an increase of the yielding force Y determines an higher accelerations transmissibility for low base excitations and a reduction of accelerations transmissibility for high base excitations. By balancing the increase of SMA damper initial stiffness with an equivalent increase of negative stiffness as is the case with $\tilde{K}_n = 1.4\alpha$ and $Y = 1.6Z_m$, (see violet line in Fig. 4.21d), the increase of the peak accelerations for low excitation amplitudes is cancelled again. According to the presence of the cubic stiffness in the NS mechanism, the equivalent stiffness and consequently the maximum acceleration reach again the values of the system S_2 for large displacements. For all the levels of negative stiffness reported, the acceleration transmissibility of S_3 is lower than the one of S_2 along the entire range of base excitations, except the configurations with low damping ratio ($Y = Z_m, y_s = 0.2$), that exhibit for high base excitations an higher acceleration transmissibility compared with S_2.
Regarding the displacements, it is worth highlighting for weak base excitations a substantial coincidence between the peak exhibited by the systems S_2 and S_3 in the MS and ST states. In fact, the curves overlap up to a value corresponding to the displacement that yields the maximum damping. Past this point, the trend of the peak displacements curve for S_3 deviates from the trend of S_2, showing a smaller reduction. The maximum deviation between the two responses occurs where the stiffness reduction is maximum. The maximum displacement reduction is quite similar for both systems S_2 and S_3 (MS, ST states) except for low damping

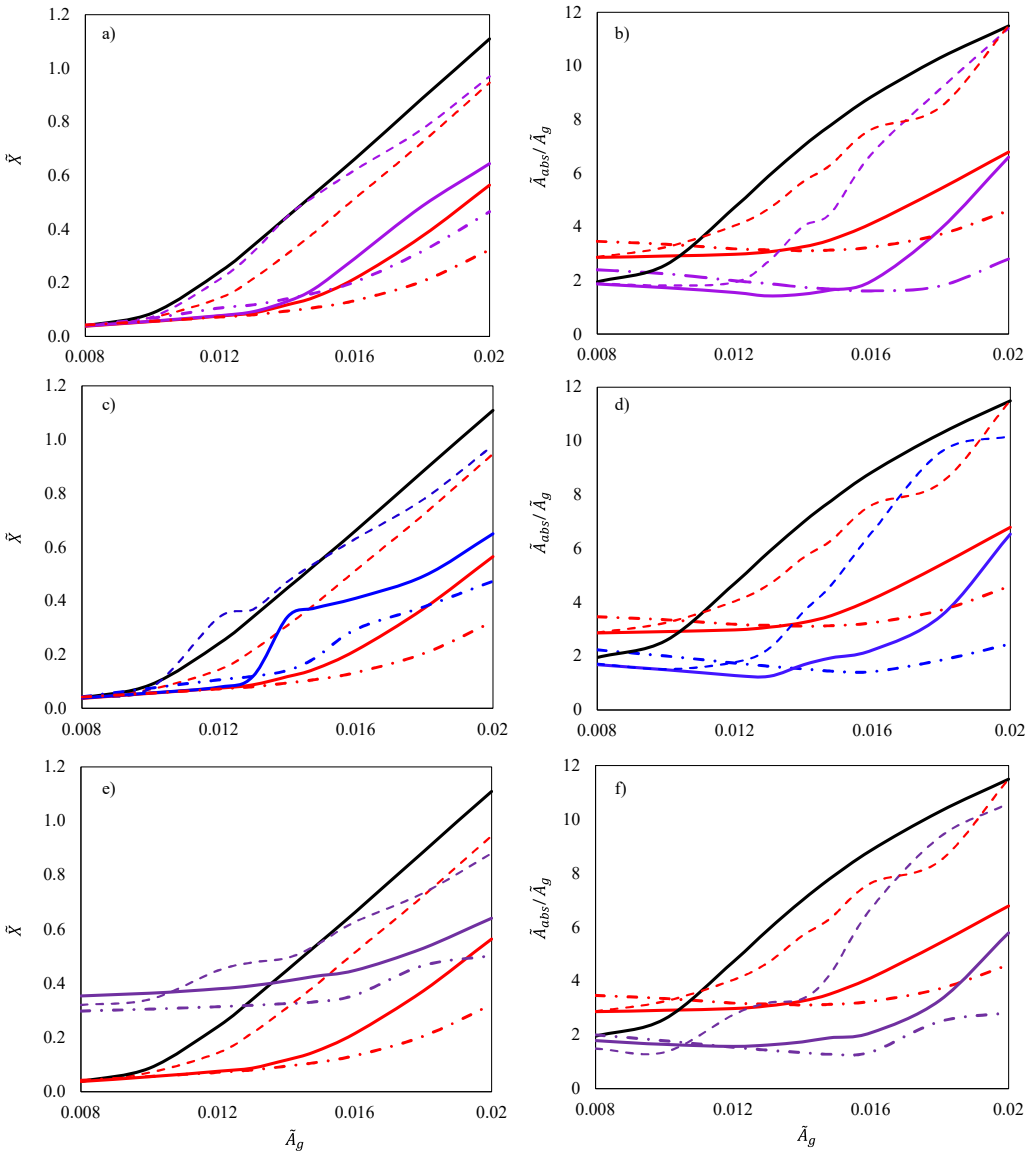

Figure 4.21: Peak responses of the controlled systems (S_2 and S_3) and that of the baseline system (S_1) in terms of nondimensional displacement (left) and absolute acceleration transmissibility (right) as function of the nondimensional base acceleration. The responses of S_2 for $Y = Z_m$ and $y_s = (0.2, 0.8)$ are represented by red dashed and red solid lines, respectively, while the response of S_2 with $Y = 1.6Z_m$ and $y_s = 0.8$ is described by red dashed-dotted lines. The responses of S_3 with $\tilde{K}_3 = -2\tilde{K}_n$ and $\tilde{K}_n = \alpha$ (a, b), 1.2α (c, d), 1.4α (e, f) are described by magenta, blue and violet lines, respectively.

ratios ($Y = Z_m, y_s = 0.2$), where it is about 20% for S_3 and 40% for S_2. This is because for $y_s = 0.2$ the stiffness reduction is not balanced by a robust damping augmentation. For the remaining damping ratios ($Y = Z_m, 1.6Z_m$ and $y_s = 0.8$), the maximum of displacements reduction for both systems is about 65%. The increase

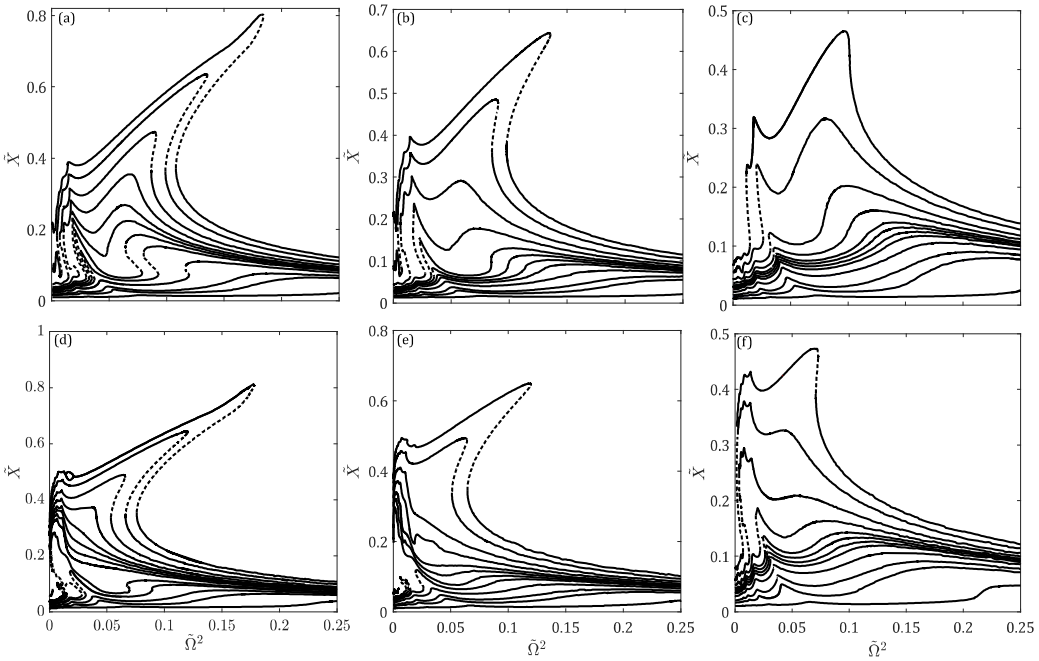

Figure 4.22: FRCs in terms of nondimensional displacements for the base accelerations set to $(0.8, 1, 1.08, 1.2, 1.28, 1.3, 1.32, 1.36, 1.4, 1.48, 1.6, 1.8, 2)10^{-2}$ for the S_3 system with $\tilde{K}_n = \alpha, Y = Z_m, y_s = (0.5, 0.8)$ (parts (a) and (b)) and $\tilde{K}_n = \alpha, Y = 1.6Z_m, y_s = 0.8$ (part (c)), and with $\tilde{K}_n = 1.2\alpha, Y = Z_m, y_s = (0.5, 0.8)$ (parts (d) and (e)) and $\tilde{K}_n = \alpha, Y = 1.6Z_m, y_s = 0.8$ (part (f)).

of yielding force (Y) from $Y = Z_m$ to $Y = 1.6Z_m$, hence, the increase of the initial superelastic stiffness, causes a smaller reduction for weak excitations and a larger reduction for moderate and strong base excitations. For the case with $\tilde{K}_n = 1.2\alpha$, the displacement reduction is smaller than that achieved with $\tilde{K}_n = \alpha$ and, for a certain range of base excitations, there exists an increase in the response. This range of base excitations corresponds to the FRCs where the displacement peak is due to the superharmonic resonance, as can be observed in Fig. 4.22. Finally, the TS configurations with $\tilde{K}_n = 1.4\alpha$ shows a strong amplification of displacement transmissibility for low excitations because of the presence of the lateral attractors. In conclusion, with the introduction of negative stiffness in parallel to SMA damper is possible to cancel the increase of acceleration transmissibility for low base excitations and to halve it for medium and strong excitations, preserving a

significant reduction of displacement compared with the baseline system S_1. In order to avoid residual displacement and amplification of peak displacement a ST configuration is to be preferred over a TS configuration.
Next, we address the force transmissibility in terms of frequency bandwidth where effective isolation is attained. As known, the response is considered effectively controlled when the transmissibility is lower than 1. For the nondimensional base acceleration of 0.02, the acceleration peak reduction for S_3 is the minimum (i.e., 40%) and it is equal to that of S_2 (see Fig. 4.21b and Fig. 4.21d). By analysing the force transmissibility under the same base accelerations, useful considerations can be drawn about the isolation performance of the proposed system. While Fig. 4.21 shows only the reduction in peak accelerations, Fig. 4.23 portrays the bandwidth of the isolated frequencies. The introduction of the SMA damper alone increases

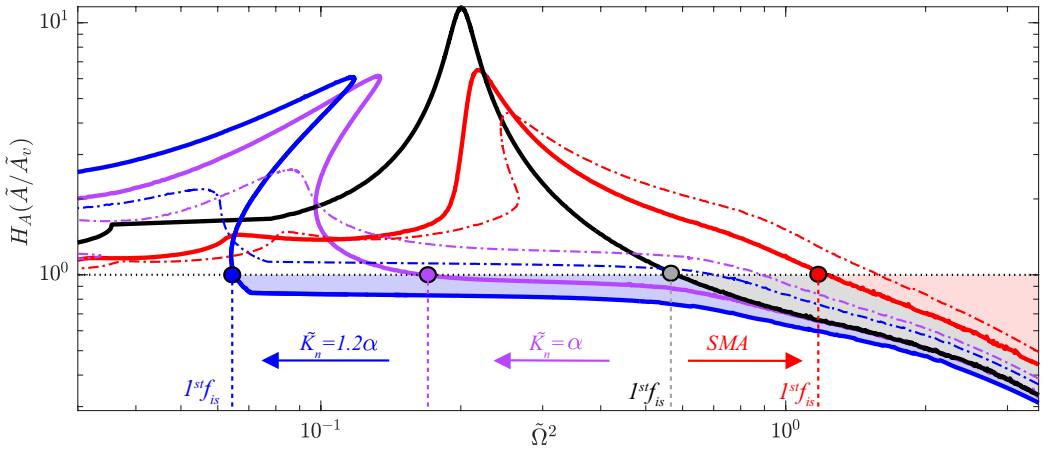

Figure 4.23: FRCs in terms of force transmissibility for a nondimensional base acceleration equal to 0.02. The response of S_1 is described by the black solid line, while the responses of S_2 when $y_s = 0.8, Y = (1, 1.6)Z_m$ are denoted by the red solid and red dashed lines, respectively. The responses of S_3 when $\tilde{K}_n = \alpha, Y = (1, 1.6)Z_m$ are described by the violet solid and dashed lines and those of S_3 when $\tilde{K}_n = 1.2\alpha, Y = (1, 1.6)Z_m$ are denoted by the blue solid and blue dashed lines, respectively. For all cases $y_s = 0.8$ and $\tilde{K}_3 = -2\tilde{K}_n$.

the value of the first isolated frequency, thus reducing the bandwidth of the isolated frequencies of 69% and 87% for $Y = Z_m$ and $Y = 1.6Z_m$, respectively. On the other hand, the negative stiffness mechanism in parallel with the SMA damper, determines a reduction of the peak response together with an increase of the isolated frequency bandwidth reducing the value of the first isolated frequency of 25% and 44% with $\tilde{K}_n = \alpha$ and $\tilde{K}_n = 1.2\alpha$, respectively. It can be observed that an increase of the SMA yielding force (Y) determines an increase of the initial superelastic stiffness not accompanied by an increase of negative stiffness. This

yields a further reduction in peak response but the isolated frequency bandwidth is reduced (see Tab. 4.1).

System	Parameters	A_{Abs}/A_g	1st isolated freq. $[\tilde{\Omega}]$	1st isolated freq. $[\tilde{\Omega}]$	Δ_f[%]
Baseline system (S_1)	$\tilde{K}_n = 0,\ Y = 0,\ y_s = 0$	11.46	0.77	1.72	0%
SMA system (S_2)	$\tilde{K}_n = 0,\ Y = Z_m,\ y_s = 0.8$	6.48	1.12	2.49	69%
	$\tilde{K}_n = 0,\ Y = 1.6\,Z_m,\ y_s = 0.8$	4.35	1.25	2.80	87%
NS-SMA system (S_3)	$\tilde{K}_n = \alpha,\ Y = Z_m,\ y_s = 0.8$	6.13	0.40	0.89	-25%
	$\tilde{K}_n = \alpha,\ Y = 1.6\,Z_m,\ y_s = 0.8$	2.61	0.94	2.10	45%
	$\tilde{K}_n = 1.2\alpha, Y = Z_m,\ y_s = 0.8$	6.07	0.25	0.57	-44%
	$\tilde{K}_n = 1.2\alpha, Y = 1.6Z_m,\ y_s = 0.8$	2.17	0.84	1.88	33%

Tab.4.1: Force transmissibility performance for the three kinds of isolated systems, S_1, S_2 and S_3.

4.4 Research of optimal configuration

The study of the dynamic response has revealed a richness of scenarios that determines an high sensitivity of response to the selection of design parameters $\tilde{K}_n, \tilde{K}_3, \tilde{Y}$ and y_s. An increase of the parameter y_s is found to be always enhancing of performances, hence it will be set on the high value $y_s = 0.8$. For the remaining three design parameters, a research of the optimal configuration is done in the 3D space $(\tilde{K}_n, \tilde{K}_3, \tilde{K}_s)$ minimizing the peak of absolute accelerations transmissibility through the use of the Differential Evolution Algorithm. Differential Evolution Algorithm (DE) is a meta heuristic method that optimizes a problem by iteratively trying to improve a candidate solution minimizing a certain quantity. Differently from other Optimization method, DE does not use the gradient of objective equation,which means DE does not require the optimization problem to be differentiable and can also be used on optimization problems that are not continuous. The algorithm optimize the problem starting from an initial population of candidate solutions and creating new candidate solutions by combining existing ones and then keeping the candidate solution that exhibits the lowest cost function. The initial population is a *nxm* matrix, where *m* represents the number of values for each of the *n* parameters selected within an uniform probability distribution on the search ranges.
The results of previous section has revealed also that the configuration that exhibit best performances mutes parameters with a variation in base excitations, hence the research of optimal configuration is done for different levels of base acceleration. In Fig. 4.24 the candidate optimal solutions for the base excitations $\tilde{A}_g = 0.01, 0.015, 0.02$ are tracked in the 3D space $(\tilde{K}_n, \tilde{K}_3, \tilde{K}_s)$ and the associated values of cost function, the peak in absolute accelerations transimissibility, are

reported.

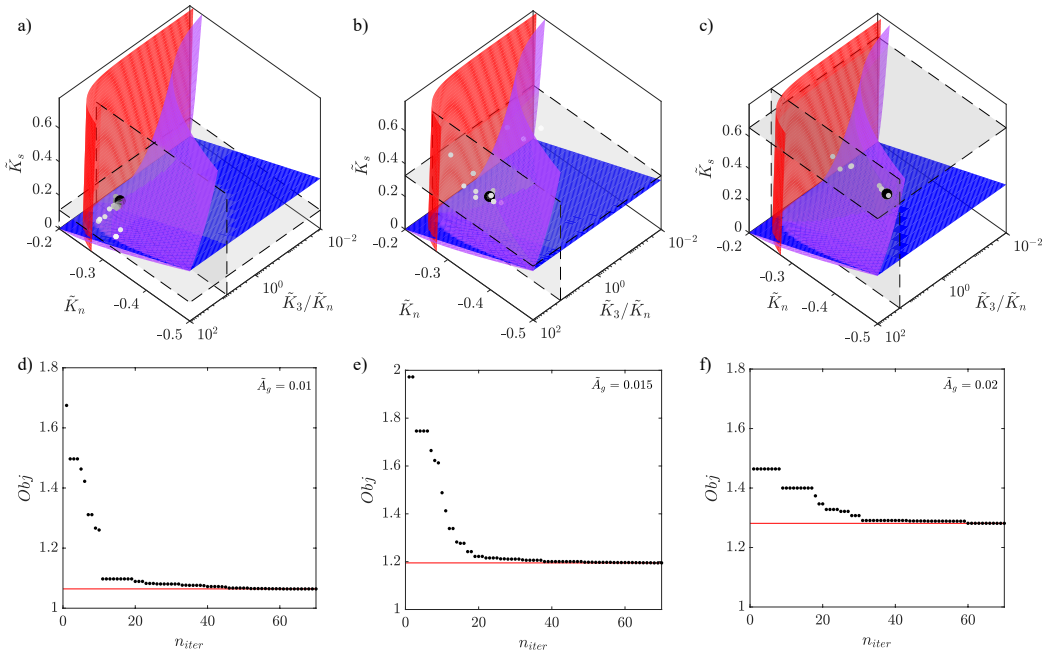

Figure 4.24: Candidate optimal solutions for the base excitations $\tilde{A}_g = 0.01$ (a), 0.015(b), 0.02(c) tracked in the 3D space $(\tilde{K}_n, \tilde{K}_3, \tilde{Y})$ and associated values of cost function (d, e, f).

As shown, the DE alghorithm achieves a good solution already from the first iteration and improves it in subsequent iterations until it asymptotes to the minimum value. For all base excitations it can be observed that the peak in absolute accelerations transmissibility is reduced to the low value of 1.2. Moreover, we can note that the best solution always lies in the ST region, in particular close to the ST-TS transition surface. This is in agreement with the above results, where it was shown that an increase in the level of negative stiffness always leads to a reduction in the peak transmissibility of absolute accelerations up to the limit value of transition in the Tri-stable state, where response amplification due to the presence of lateral equilibria can occur. The parameters planes $(\tilde{K}_n, \tilde{K}_3)$ and $(\tilde{K}_n, \tilde{K}_s)$ passing through the optimum point were swept in order to investigate the trend of the cost function when the parameters vary. The associated contour plots in terms of peak of displacements and absolute accelerations transmissibility FRCs are reported for the base excitations $\tilde{A}_g = 0.01, 0.015, 0.02$ in Fig. 4.25, 4.26, 4.27, respectively. It is worth noting that the configurations lying on vertical line with ascissa $\tilde{K}_n = 0$ in the $(\tilde{K}_n, \tilde{K}_3)$ plane are representative of the system with the SMA damper alone (S_2), while the point with coordinates $\tilde{K}_n = 0, \tilde{K}_s = 0$ in the $(\tilde{K}_n, \tilde{K}_s)$ plane denotes the response of the baseline system (S_1). For all base excitation levels, it can be

observed that in plane $(\tilde{K}_n, \tilde{K}_3)$ the contours associated with accelerations peak follow the shape of the transition curves $MS \rightarrow ST$ and $ST \rightarrow TS$, exhibiting a valley in correspondence of the ST region. On the other hand, the peak in displacements FRCs keep almost costant until the $ST \rightarrow TS$ transition curve, past which become strongly affected by the lateral equilibrium.

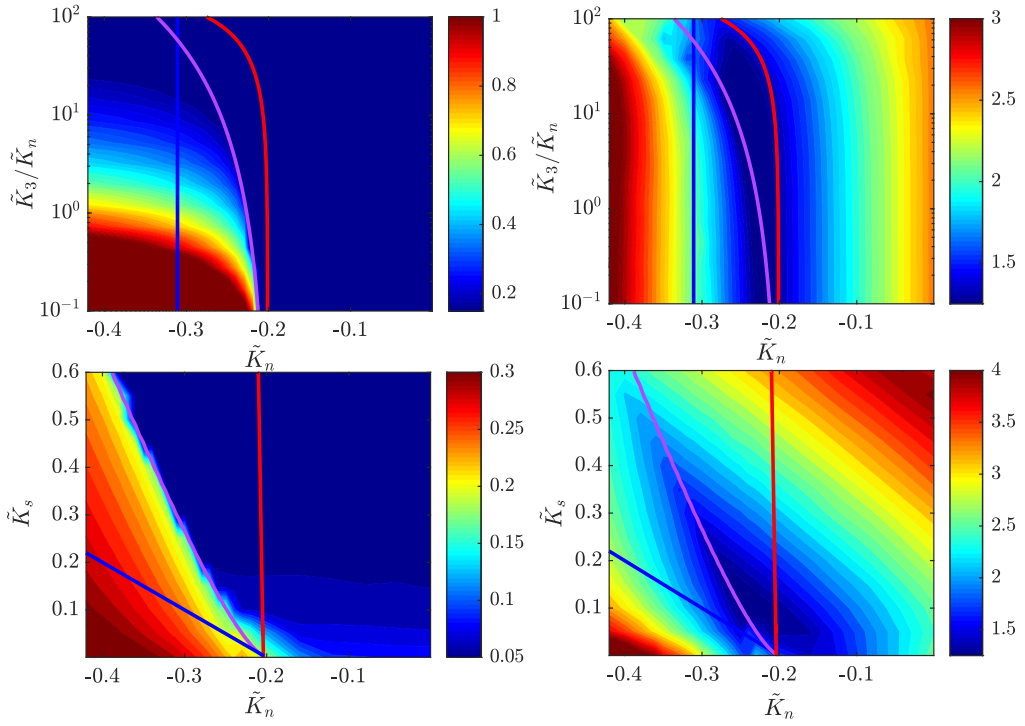

Figure 4.25: Contour plots in terms of peak of displacements (a, c) and absolute accelerations transmissibility (b, d) FRCs for the base excitation $\tilde{A}_g = 0.01$ on the planes $(\tilde{K}_n, \tilde{K}_3)$ for $\tilde{K}_s = 0.11$ (a, b) and $(\tilde{K}_n, \tilde{K}_s)$ for $\tilde{K}_3 = -7.33\tilde{K}_n$ (c, d).

The contour maps associated with the base acceleration $\tilde{A}_g = 0.01$, representative of low base excitation levels, exhibit the minimum in acceleration for relative low value of $\tilde{K}_s$. This depend by the fact that the mass oscillates with small amplitudes and the negative effect of an increase of superelastic hysteresis, hence of the initial stiffness, is more pronounced than the beneficial effect introduced by the added damping. The optimal solution shows a peak in displacement and absolute accelerations transmissibility of 0.068 and 1.08, respectively. On the other hand, the associated S_2 configuration (with the same SMA damping but without negative stiffness) exhibits, compared with the optimal S_3 configuration, more or less the same displacement (0.062) but more of two times the acceleration transmissibility (2.58). For the base acceleration $\tilde{A}_g = 0.015$, representative of medium base

excitation levels, the strong improvement of S_3 compared to S_2 strongly persist, in fact the optimal configuration S_3 shows a peak in displacement and absolute accelerations transmissibility of 0.09 and 1.28, respectively, while the associated S_2 configuration exhibit the same displacement peak and absolute accelerations transmissibility peak of 3. The optimal configuration this time requires an higher $\tilde{K}_s$ in order to exploit sufficient hysteretic damping. Looking the contour maps on the plane $(\tilde{K}_n, \tilde{K}_s)$, it can be observed that in the region of low values of $\tilde{K}_s$, hence with low hysteretic damping, there is an amplification in both displacement and acceleration peaks. The same considerations can be made for the optimization done for the last reported base excitation $\tilde{A}_g = 0.02$, representative of high base excitation levels. Also for this ground acceleration, the peak of displacement FRCs of the optimal system S_3 and of the associated S_2 system are equal (0.11), while the peak of absolute accelerations transmissibility FRCs of S_2 (3.1) is two times the one of S_3 (1.4).

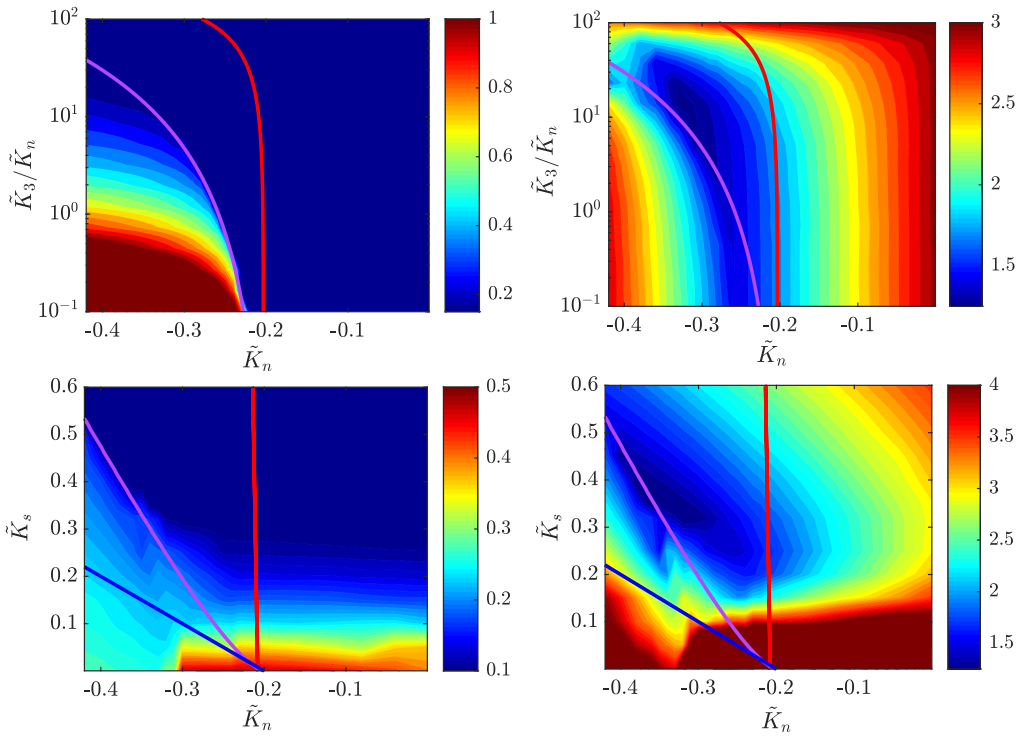

Figure 4.26: Contour plots in terms of peak of displacements (a, c) and absolute accelerations transmissibility (b, d) FRCs for the base excitation $\tilde{A}_g = 0.01$ on the planes $(\tilde{K}_n, \tilde{K}_3)$ for $\tilde{K}_s = 0.327$ (a, b) and $(\tilde{K}_n, \tilde{K}_s)$ for $\tilde{K}_3 = -13.91\tilde{K}_n$ (c, d).

In Fig. 4.28 are reported the displacements and absolute accelerations transmissibility FRCs of the configurations optimized for the base accelerations $\tilde{A}_g =$

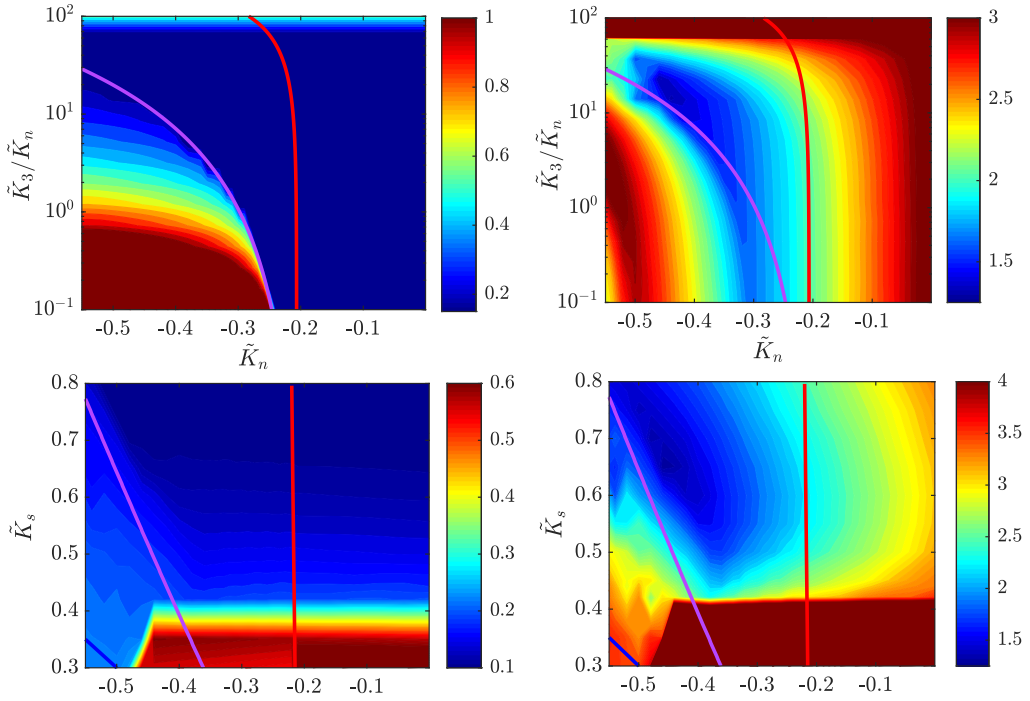

Figure 4.27: Contour plots in terms of peak of displacements (a, c) and absolute accelerations transmissibility (b, d) FRCs for the base excitation $\tilde{A}_g = 0.01$ on the planes $(\tilde{K}_n, \tilde{K}_3)$ for $\tilde{K}_s = 0.654$ (a, b) and $(\tilde{K}_n, \tilde{K}_s)$ for $\tilde{K}_3 = -20.5\tilde{K}_n$ (c, d).

$0.01, 0.015, 0.02$. The strong improvement of displacements and accelerations transmissibility is clearly notable.

Figure 4.29 shows the hysteric cycles of the optimal S_3 configurations corresponding to the resonant response, together with their damping curves. It can be observed that the configurations provided by optimization for each base accelerations are those exhibiting the peak of damping at the amplitude equal to the one reached in resonance. For different levels of base excitation the oscillator will reach different amplitudes of motion and the optimal configurations follow with the amplitude corresponding to the peak of damping the raising amplitude of motion. This, as can be noted in Fig. 4.29, results in a shift to the right of peak in damping curves of optimal configurations for increasing ground accelerations.

The trend of the optimal parameters in function of base acceleration is shown in Fig. 4.30 and can therefore be explained by the purpose of the optimization algorithm to achieve two objectives: maximizing the damping introduced and allocating it to a progressively increasing amplitude. This implies that in 3D parameter space, the points corresponding to the optimized parameter terns varying the base

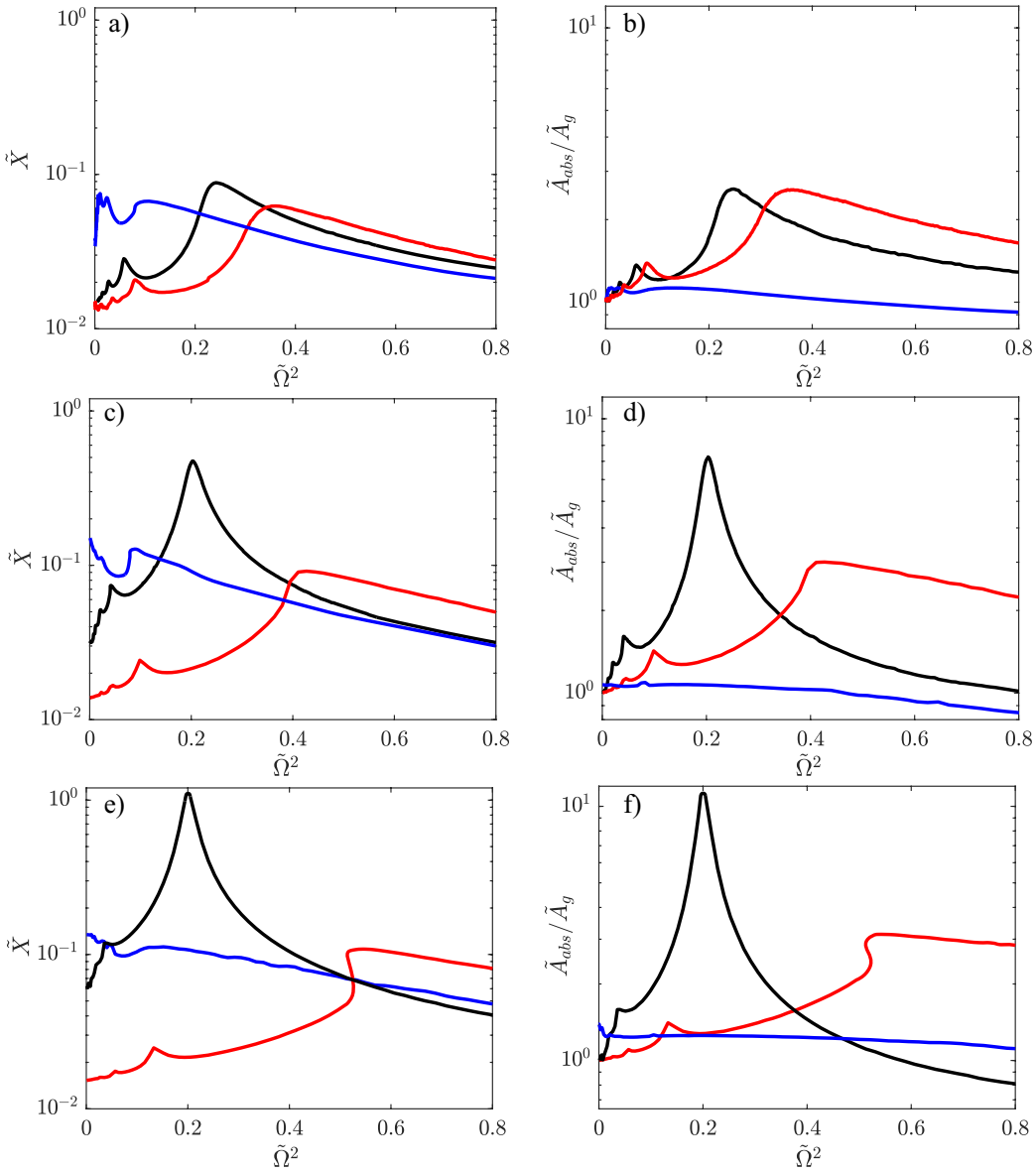

Figure 4.28: FRCs in terms of nondimensional displacement (left) and force transmissibility (right) for a ground acceleration of 0.01 (a, b), 0.015 (c, d), 0.02 (e, f) of optimized S_3 configurations, of the associated S_2 configurations and of the baseline system in blu, red and black lines, respectively.

excitation describe a curve lying on the transition surface $ST \rightarrow TS$.
In Fig. 4.31 are reported the displacements and absolute accelerations FRCs peaks vs the base excitations for the three configurations optimized with $\tilde{A}_g = 0.01, 0.015, 0.02$. It can be observed that, in agreement with the above, the configuration optimized

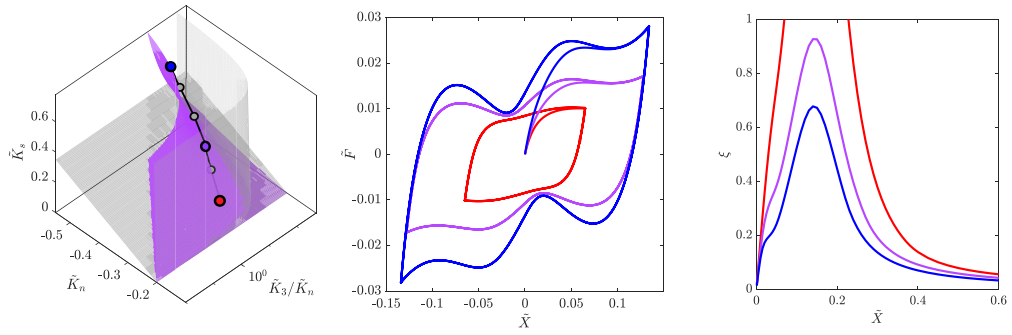

Figure 4.29: Hysteric cycles of resonant response(left) and damping curves (right) of the S_3 configurations optimized for $\tilde{A}_g = 0.01, 0.015, 0.02$ in red, violet and blue lines, respectively.

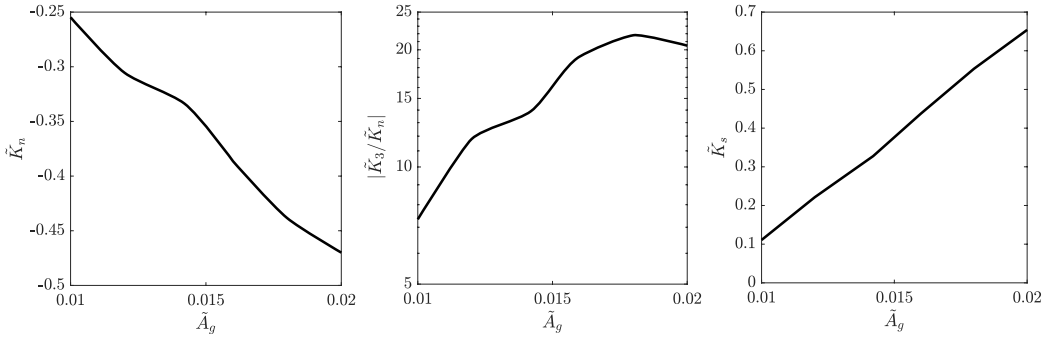

Figure 4.30: Optimized parameters $\tilde{K}_n, \tilde{K}_3, \tilde{K}_s$ vs base excitation.

with $\tilde{A}_g = 0.01$ suffers a deterioration of performances for increase of base acceleration, hence, of amplitude of motion. On the other hand, the configurations optimized with $\tilde{A}_g = 0.015, 0.02$ show enhanced performances for the optimizing amplitudes together with a slight loss of performance for lower base accelerations. In the light of the above, the preferable and most robust configurations is the one optimized for the highest base acceleration.

4.5 Conclusions

A novel vibration isolation system featuring a negative stiffness mechanism and superelastic damping arranged in parallel with classical elastomeric isolation devices is parametrically investigated for different levels of negative stiffness, superelastic damping ratio, and yielding force.
The introduction of superelasticity alone, without negative stiffness, leads to a detrimental increase of the initial stiffness and, hence, to an increase of accelera-

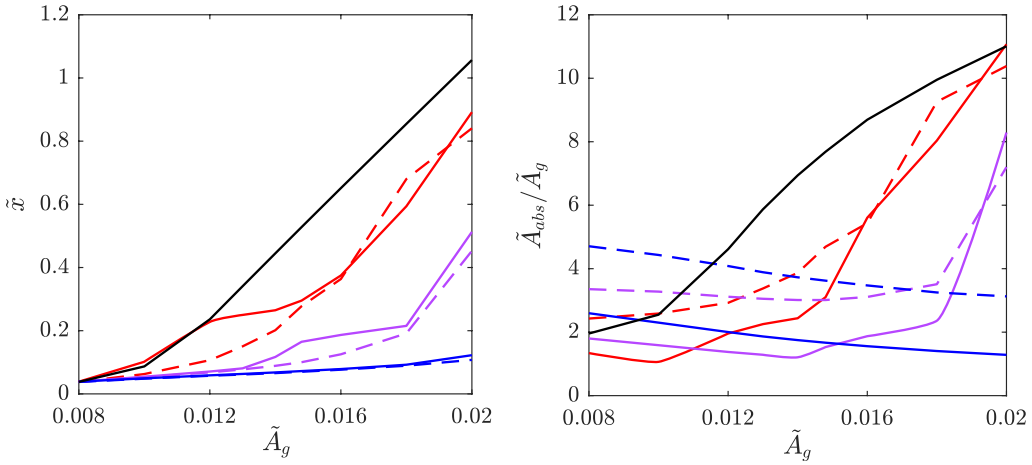

Figure 4.31: Displacements (left) and absolute accelerations transmissibility (right) FRCs peaks vs base excitation of the configurations optimized for $\tilde{A}_g = 0.01, 0.015, 0.02$ in red, violet and blue lines, respectively and of the associated S_2 configurations in dashed lines. The response of the baseline system S_1 is denoted by the black lines.

tions for low base excitations. On the other hand, by accurately tuning the negative stiffness with the superelastic damping, a remarkable reduction of displacement and acceleration amplitudes can be achieved, while preserving a self-recentering capability and without incurring an increase of acceleration transmissibility for low excitations. To ensure an effective acceleration transmissibility reduction and, at the same time, the mono-stability and self-recentering capability of the isolated system, the optimum negative stiffness coefficient $\tilde{K}_n$ must be bounded in the range $\alpha < \tilde{K}_n < 1.2\alpha$, where α is the ratio between the post-elastic and the initial isolators stiffness. Regarding the superelastic rheological element, the initial stiffness must be equal to the negative stiffness in order to keep the stiffness of the isolation system unaltered at the origin while exhibiting sufficiently high damping. By considering the lower bound for the negative stiffness, $\tilde{K}_n = \alpha$, the optimum superelastic yielding force was found to be $\tilde{Y} = \alpha\tilde{x}_g$, where $\tilde{x}_g$ is the ratio between the gap displacement and the maximum allowable displacement. Moreover, a high hysteresis ratio y_s was shown to entail a better isolation performance. The study of the nonlinear dynamic response and its bifurcations revealed extremely rich bifurcation scenarios with detached resonances and unusual interactions between the primary resonance and superharmonic resonances, or between superharmonic resonances of various orders, featuring multiplicity of coexisiting attractors, secondary Hopf bifurcations responsible for quasi-periodicity, synchronization, symmetry-breaking and period-doubling cascades towards chaos. The

detached resonance curves and bifurcations were numerically explored for high levels of negative stiffness and their nonlinear impact on isolation performance was discussed. In particular, when $\tilde{K}_n = \alpha$, the peak of the detached resonance curve was found to be lower than the peak of the main resonance curve, thus not affecting the isolation performance. On the contrary, for a higher negative stiffness value (i.e., $\tilde{K}_n = 1.2\alpha$), the peak of the detached resonance curve was found to be larger than the primary resonance peak, hence, largely affecting the isolation performance. Moreover, the quasi-periodicity of the response of the tri-stable configuration (i.e., $\tilde{K}_n = 1.4\alpha$) together with the subsequent dynamic amplification were illustrated. The obtained results pave the way towards a streamlined design process which aims to optimize the isolation performance of the proposed negative stiffness superelastic device in terms of transmissibility and dynamic stability.

Chapter 5

Nonlinear dynamic response to pulse load

The response of the proposed isolation system under impulsive ground motion is studied in the next chapter. The ground motion is modeled according to three different formulations, associated with different kinds of ground motion mechanisms. The performances are evaluated computing Shock Response Curves (SCR) and varying design parameters and the amplitude of the motion.

5.1 Pulse load type

Three kinds of base shock excitations are considered: rounded displacement step (P1), rounded displacement pulse (P2), and oscillatory displacement step (P3) (see Fig. 5.1). The mathematical expressions of the ground motions and accelerations for each pulse type are:

$$\tilde{x}_{p1}(\tilde{t}) = \tilde{A}[1-(1+\gamma_p\tilde{t})e^{-\gamma_p\tilde{t}}] \tag{5.1}$$

$$\tilde{a}_{p1}(\tilde{t}) = \tilde{A}(1-\gamma_p\tilde{t})\gamma_p^2 e^{-\gamma_p\tilde{t}} \tag{5.2}$$

for the rounded displacement step (P1);

$$\tilde{x}_{p2}(\tilde{t}) = \frac{e^2}{4}\tilde{A}\,(\gamma_p\tilde{t})^2 e^{-\gamma_p\tilde{t}} \tag{5.3}$$

$$\tilde{a}_{p2}(\tilde{t}) = \frac{e^{2-\tilde{t}\gamma_p}}{4}\tilde{A}\gamma_p^2\,[\gamma_p\tilde{t}\,(\gamma_p\tilde{t}-4)+2] \tag{5.4}$$

for the rounded displacement pulse (P2);

$$\tilde{x}_{p3}(\tilde{t}) = 0.68684\tilde{A}\left[1-e^{-0.25\gamma_p\tilde{t}}\,(0.25\sin(\gamma_p\tilde{t})+\cos(\gamma_p\tilde{t}))\right] \tag{5.5}$$

$$\tilde{a}_{p3}(\tilde{t}) = \tilde{A}\gamma_p^2 e^{-0.25\gamma_p\tilde{t}}\,[0.729768\cos(\gamma_p\tilde{t})-0.182442\sin(\gamma_p\tilde{t})] \tag{5.6}$$

for the oscillatory displacement step (P3), where $\tilde{A}$ is the nondimensional ground motion amplitude while γ_p represents the shock severity.

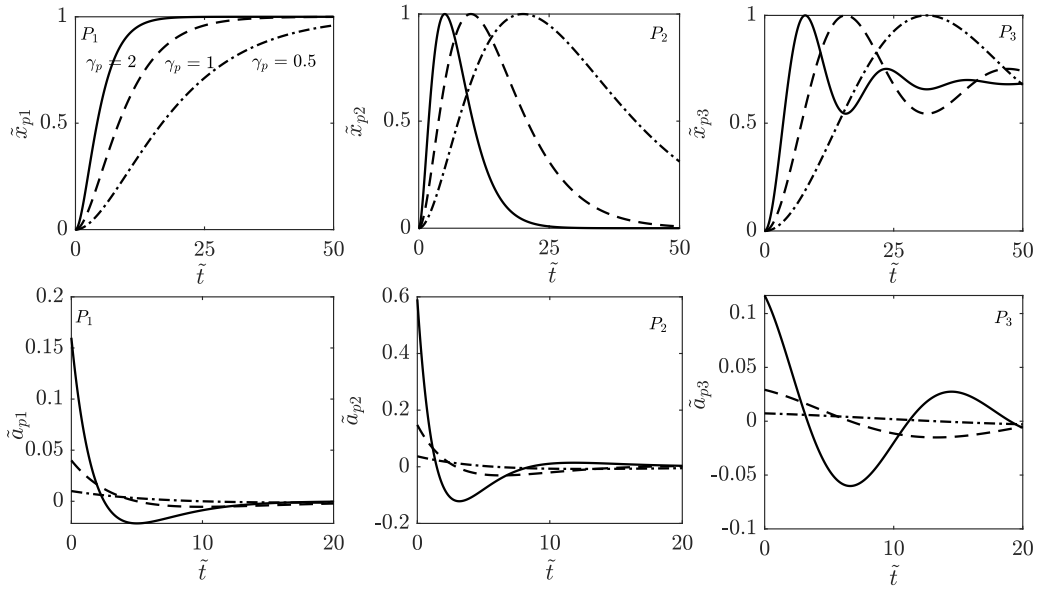

Figure 5.1: (top) Ground displacements and (bottom) associated accelerations for the pulse loads denoted by P1,P2,and P3.

5.2 Response to P1

The response to the first type of pulse load is discussed first. In Fig. 5.2 the time histories of the displacement,acceleration and input energy are shown when $\gamma_p = 1$ and $\tilde{A} = 0.4$ and different levels of negative stiffness are accounted for ($\tilde{K}_n = 0, -0.2, -0.32, -0.42$).

As seen, the system with $\tilde{K}_n = -0.2$ is still monostable and self-recentering but shows a faster deacy rate with respect to the case without negative stiffness $\tilde{K}_n = 0$. For $\tilde{K}_n = -0.32$, a greater reduction of absolute accelerations and input energy is obtained. In addition, a residual displacement equal to the amplitude of pulse is exhibited. For $\tilde{K}_n = -0.42$, an increase of absolute accelerations and input energy with respect to the case $\tilde{K}_n = -0.32$ is experienced, while the residual displacement is greater than the amplitude of pulse. This is due to the *well − trapping phenomenon*. The configuration with $\tilde{K}_n = -0.32$ is tri-stable and, in particular, the nontrivial equilibrium is at a distance $\tilde{x}_{f0u}$ equal to the pulse amplitude $\tilde{A}$. This causes the mass under ground motion to settle down almost instantly into the lateral potential well.

By recording maximum values of displacement and absolute acceleration, input

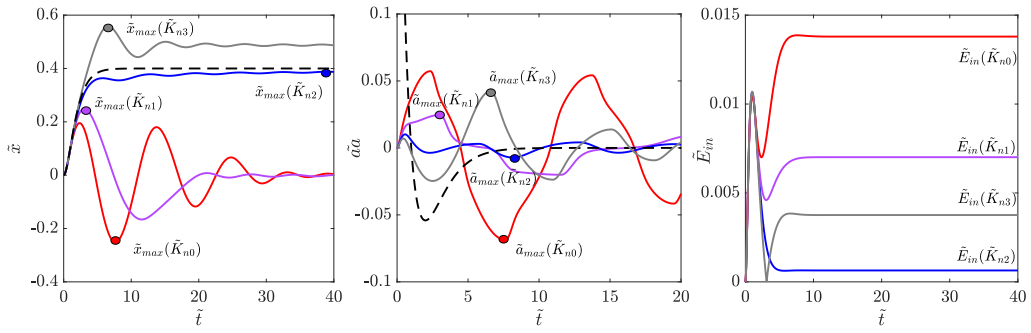

Figure 5.2: Time histories of displacements, accelerations and input energy for the system with $\tilde{K}_n = -(0, 0.22, 0.32, 0.45)$ and $\tilde{K}_3 = -2\tilde{K}_n$ (red, violet, blue and gray lines, respectively) under pulse load P1 with $\gamma_p = 1$ and $\tilde{A} = 0.4$.

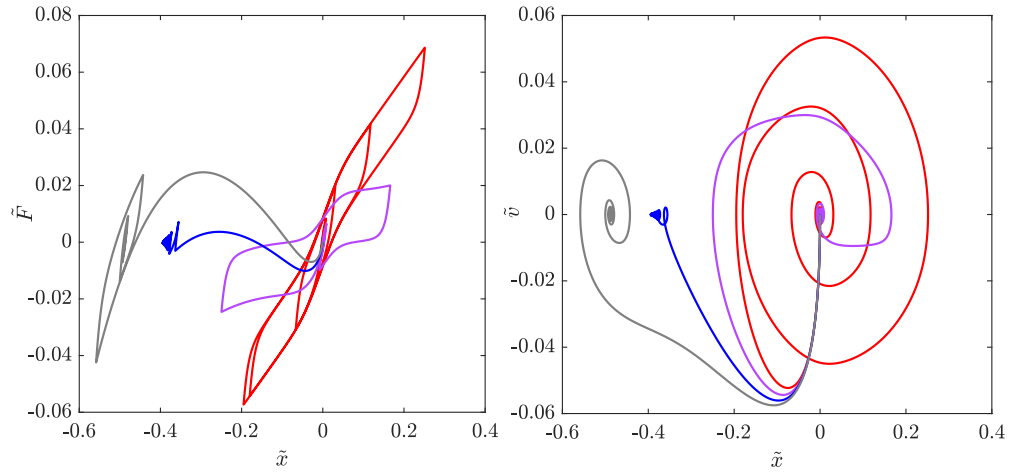

Figure 5.3: Force-displacement cycles and phase portraits for the system with $\tilde{K}_n = -(0, 0.22, 0.32, 0.45)$ and $\tilde{K}_3 = -2\tilde{K}_n$ (red, violet, blue and gray lines, respectively) under pulse load P1 with $\gamma_p = 1$ and $\tilde{A} = 0.4$.

energy and residual displacement and by changing the parameter corresponding to the speed and severity of pulse γ_p, the shock curves in terms of displacement (DSCs), residual displacement (RDSCs), absolute acceleration (ASCs) and input energy (ESCs) are numerically obtained changing the main design parameters $\tilde{K}_n$ and $\tilde{K}_3$ (see Figs. 5.4 and 5.5. Absolute acceleration and input energy are efficiently reduced so long as the negative stiffness does not exceed $\tilde{K}_n = -0.32$, while for greater value of $\tilde{K}_n$ the response tends to grow. The same is valid for $\tilde{K}_3$; an increase of this parameter leads initially to a reduction of ASCs and ESCs, subsequently it causes a new increase of these quantities. The DSCs of the tri-stable

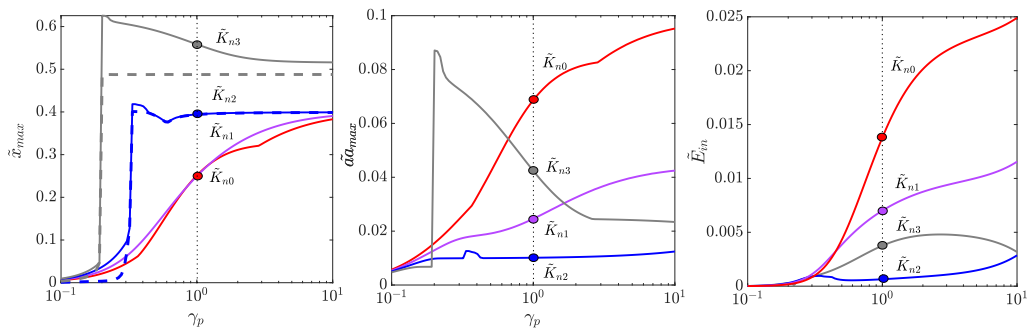

Figure 5.4: (left) DSCs, (center) ASCs and (right) ESCs for the system with $\tilde{K}_n = -(0, 0.22, 0.32, 0.45)$ and $\tilde{K}_3 = -2\tilde{K}_n$ (red, violet, blue and gray lines, respectively).

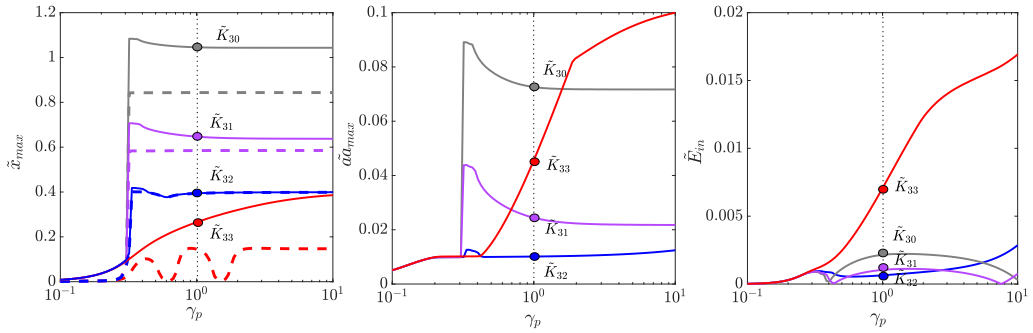

Figure 5.5: (left) DSCs, (center) ASCs and (right) ESCs for the system with $\tilde{K}_3 = -(0.5, 1, 2, 10)\tilde{K}_n$ and $\tilde{K}_n = -0.32$ (red, violet, blue and gray lines, respectively).

configuration show a jump from the lateral unstable to the lateral stable equilibrium and, unlike the mono-stable configuration, a residual displacement exists and is equal to the amplitude of the lateral stable equilibrium ($\tilde{x}_{f0u}$). As noted in Fig. 5.6, this jump happens when the pulse causes a displacement greater than the unstable equilibrium and then the mass is attracted by the lateral stable equilbrium. The configuration that achieves the best performance shows a residual displacement shock curve RDSC which coincides with the maximum displacement curve DSC, a direct effect of the *well − trapping phenomenon*. In order to find the optimum values of $\tilde{K}_n$ and $\tilde{K}_3$ that lead to the best reduction of accelerations and input energy the maximum values of the shock curves DSCs, RDSCs, ASCs and ESCs and their root mean square values are recorded changing the parameters $\tilde{K}_n$ and $\tilde{K}_3$ (see Figs. 5.7 and 5.8). Note that the optimum values of negative stiffness $\tilde{K}_{nopt}$ and cubic coefficient $\tilde{K}_{3opt}$ are those that cause a residual displacement equal to the amplitude of pulse and for these values the residual displacement shock curve

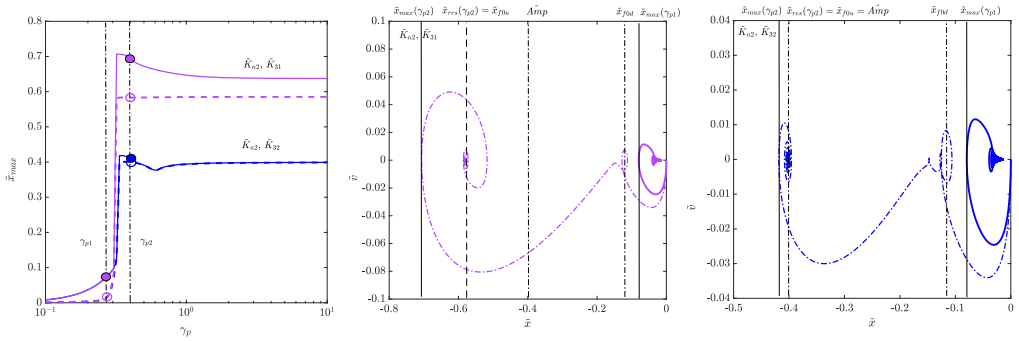

Figure 5.6: (left) DSCs for the system with $\tilde{K}_3 = -(1,2)\tilde{K}_n$ and $\tilde{K}_n = -0.32$ (violet and blue lines, respectively) and phase portraits for a pulse load with $\gamma_p = (0.28, 0.4)$ in solid and dashed lines, respectively.

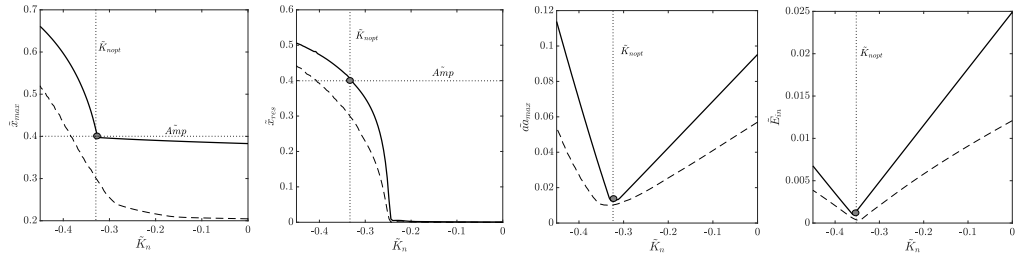

Figure 5.7: Peak (solid line) and RMSv (dashed line) of DSCs, RDSCs, ASCs and ESCs vs. negative stiffness coefficient $\tilde{K}_n$.

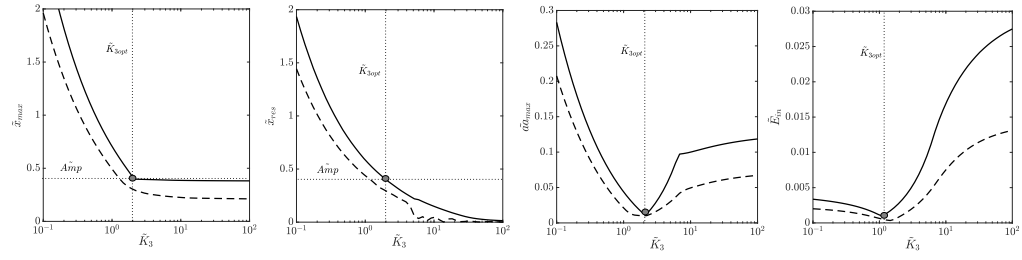

Figure 5.8: Peak (solid line) and RMSv (dashed line) of DSCs, RDSCs, ASCs and ESCs vs. cubic stiffness coefficient $\tilde{K}_3$.

touches the maximum displacement curve DSC. Assuming that the residual displacement for the tri-stable configurations is equal to the amplitude of the lateral equilibria (see Fig. 5.9), thanks to the *well − trapping phenomenon*, it is possible to define in analytical fashion the optimum values of negative stiffness $\tilde{K}_n$ and

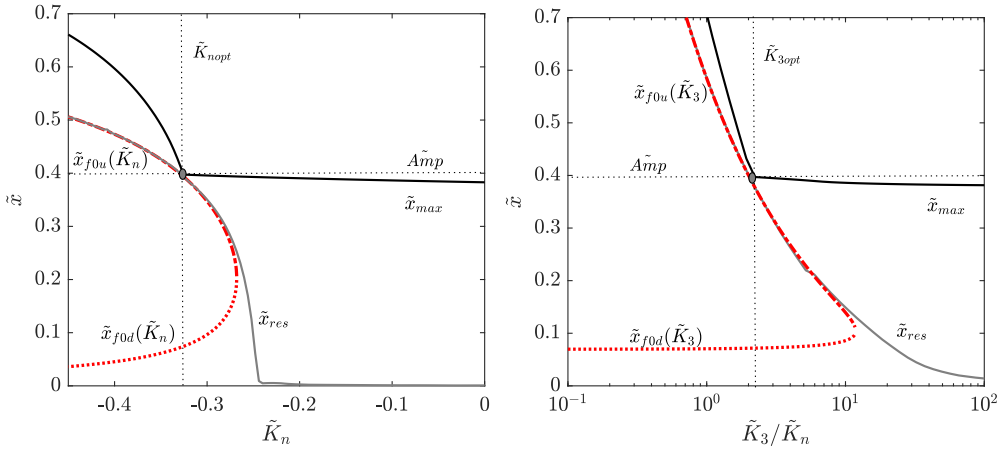

Figure 5.9: (left) Peak of DSCs (black line) and RDSCs (gray line) vs. $\tilde{K}_n$(left) and vs. $\tilde{K}_3$ and analytical curves $\tilde{x}_{f0d}$, $\tilde{x}_{f0u}$ in red dashed-dotted and dashed lines, respectively.

cubic stiffness $\tilde{K}_3$ solving $\tilde{f}_{e2}(\tilde{A}) = 0$.

$$\tilde{K}_{nopt} = \frac{(\alpha_s - 1)\tilde{x}_{gapm}\tilde{K}_s}{\tilde{A}} - \alpha_s\tilde{K}_s - \tilde{K}_3\tilde{x}^2 - \alpha \tag{5.7}$$

$$\tilde{K}_{3opt} = \frac{(\alpha_s - 1)\tilde{x}_{gapm}\tilde{K}_s - \tilde{x}\left(\tilde{K}_n + \alpha_s\tilde{K}_s + \alpha\right)}{\tilde{A}^3} \tag{5.8}$$

By accounting for these equations it is possible to predict analytically in the parameters ($\tilde{K}_n$, $\tilde{K}_3$) space the combination of values that give rise to $\tilde{f}_{e2}(\tilde{A}) = 0$ for a definite pulse load amplitude. In Fig. 5.10 it is possible to note that this equation shows two different branches separated by the contact point between the curve $\tilde{f}_{e2}(\tilde{A}) = 0$ and the transition curve $ST \rightarrow TS$. The roots of $\tilde{f}_{e2}(\tilde{A}) = 0$ are $\tilde{x} = \tilde{x}_{f0u} = \tilde{x}_{f0d}$. In the first branch (high values of cubic coefficient) $\tilde{f}_{e2}(\tilde{A}) = 0$ is achieved for $\tilde{x} = \tilde{x}_{f0u}$. This is the real optimum condition; in fact the pulse amplitude is equal to the amplitude of the stable equilibrium and thus the well can trap the mass. In the second branch (low values of cubic coefficient) $\tilde{f}_{b2}(\tilde{A}) = 0$ is achieved for $\tilde{x} = \tilde{x}_{f0d}$: For this combination an escape from the unstable to the stable lateral equilibrium causes an amplification of the response. In Fig. 5.11 the optimum combinations ($\tilde{K}_n$, $\tilde{K}_3$) for pulse loads of different magnitude are reported, together with the trend of $\tilde{K}_{nopt}$ vs. the ground motion amplitude for different values of $\tilde{K}_3$. Here we note that with the lowest level of cubic coefficient $\tilde{K}_3/\tilde{K}_n = 2e^{-2}$ it is not possible to exploit the $well-trapping\ phenomenon$ and then there are no optimum values of $\tilde{K}_n$. For $\tilde{K}_3/\tilde{K}_n = 1.3e^{-1}$ it is possible to exploit the well-trapping for pulse load amplitude greater then $\tilde{A} > 0.42$. For higher values of cubic coefficient the range of amplitudes of pulse load that can be ef-

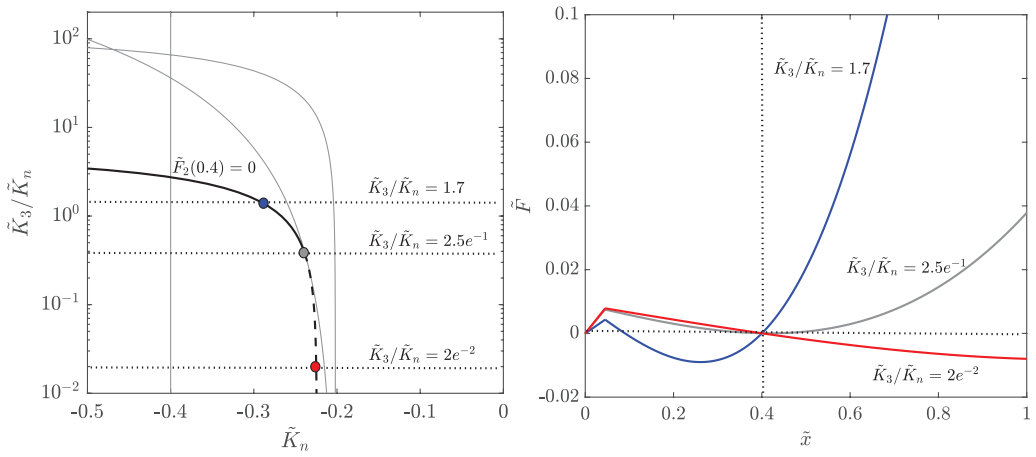

Figure 5.10: (left) Loci in the $\tilde{K}_n$, $\tilde{K}_3$ plane $\tilde{f}_{e2}(0.4)=0$. (right) Force-displacement equilibrium response of the system in three different configurations along the curve $\tilde{f}_{b2}(0.4)=0$.

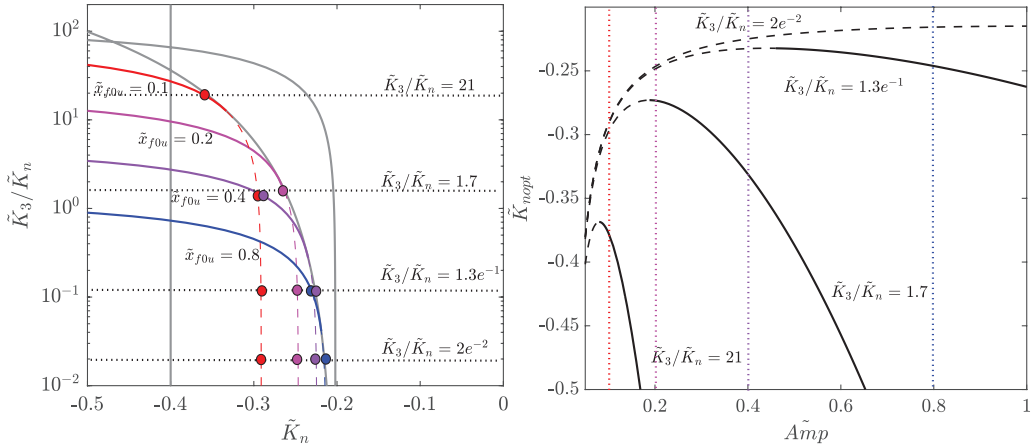

Figure 5.11: (left) Optimum $(\tilde{K}_n,\ \tilde{K}_3)$ for a pulse load of amplitude $\tilde{A}=(0.1,0.2,0.4,0.8)$ in red, magenta, violet and blue lines, respectively. (right) Trend of $\tilde{K}_{nopt}$ vs. pulse amplitude for the system with $\tilde{K}_3/\tilde{K}_n=(2e^{-2},1.3e^{-1},1.7,21)$.

ficiently controlled by the well-trapping grows but also the variation of optimum value of $\tilde{K}_{nopt}$ become stronger. Changing values of $\tilde{K}_n$ and $\tilde{K}_3$ and recording maximum values of the shock curves DSCs, RDSCs, ASCs and ESCs and their root mean square (RMS) values, performance maps in the tridimensional parameters space are numerically obtained.

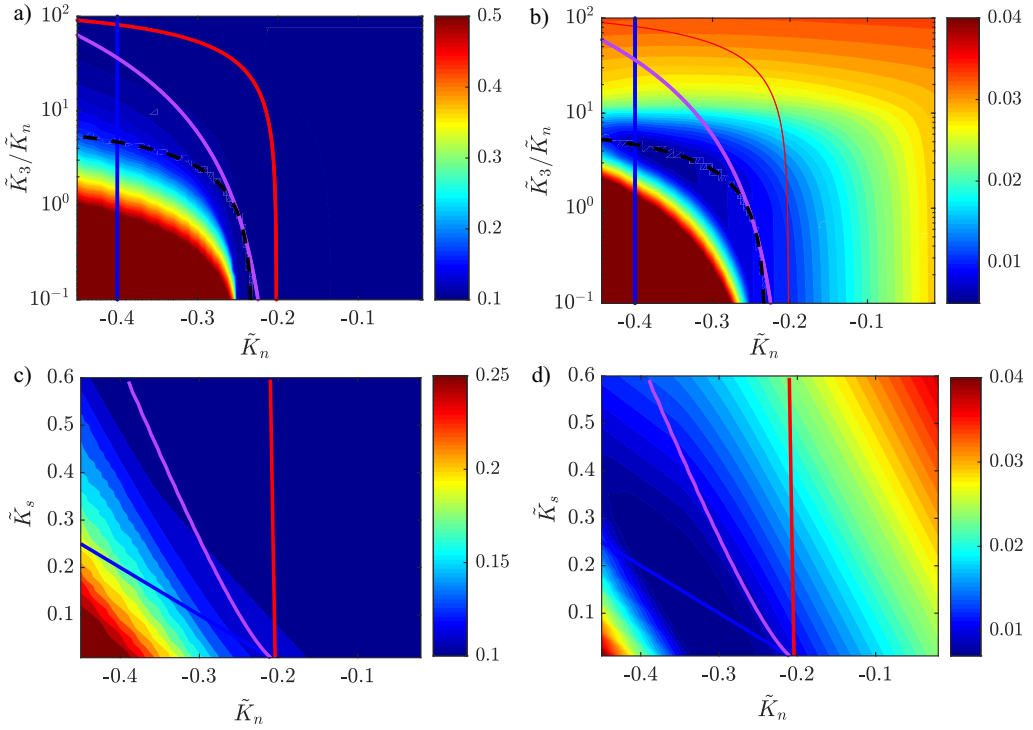

Figure 5.12: Performance maps in terms of RMS of DSCs (left) and ASCs (right) in the ($\tilde{K}_n$, $\tilde{K}_3$) space with $\tilde{K}_s = 0.2$ (top) and in the ($\tilde{K}_n$, $\tilde{K}_s$) space with $\tilde{K}_3/\tilde{K}_n = 3.9$ (bottom) for a pulse amplitude of 0.3. The transition curves between stability region are denoted by red, violet and blue lines and the analytical prediction of optimum values by black dashed line.

In Figs. 5.12, 5.13 and 5.14 performance contour plots and analytical prediction of optimum parameters combination are reported for pulse amplitudes $\tilde{A} = 0.3, 0.5, 1$, respectively. Here we note that the minimum of level curves, corresponding to the optimum numerical $\tilde{K}_n$, $\tilde{K}_3$ combination, lies to the tri-stable region for all pulse amplitudes and, in particular, on the curve $\tilde{f}_{e2}(\tilde{A}) = 0$, thus proving the effectiveness of well-trapping phenomenon. In order to evaluate the robustness of the parameters optimization for a specific pulse amplitude under different amplitudes, the system with three different configurations coinciding with the optimum numerical combinations $\tilde{K}_n$, $\tilde{K}_3$ for pulse amplitudes $\tilde{A} = (0.3, 0.5, 1)$ ($C1$, $C2$ and $C3$, respectively) is considered and, for each configuration, the shock curves are obtained for a pulse amplitudes range $\tilde{A} = [0.1 : 0.1 : 1]$. In Fig. 5.15 note that the system optimized for $\tilde{A} = 0.3$ effectively reduce accelerations through well-trapping only for low pulse amplitudes.
For the system optimized for $\tilde{A} = 0.5$ the range of pulse amplitudes effectively

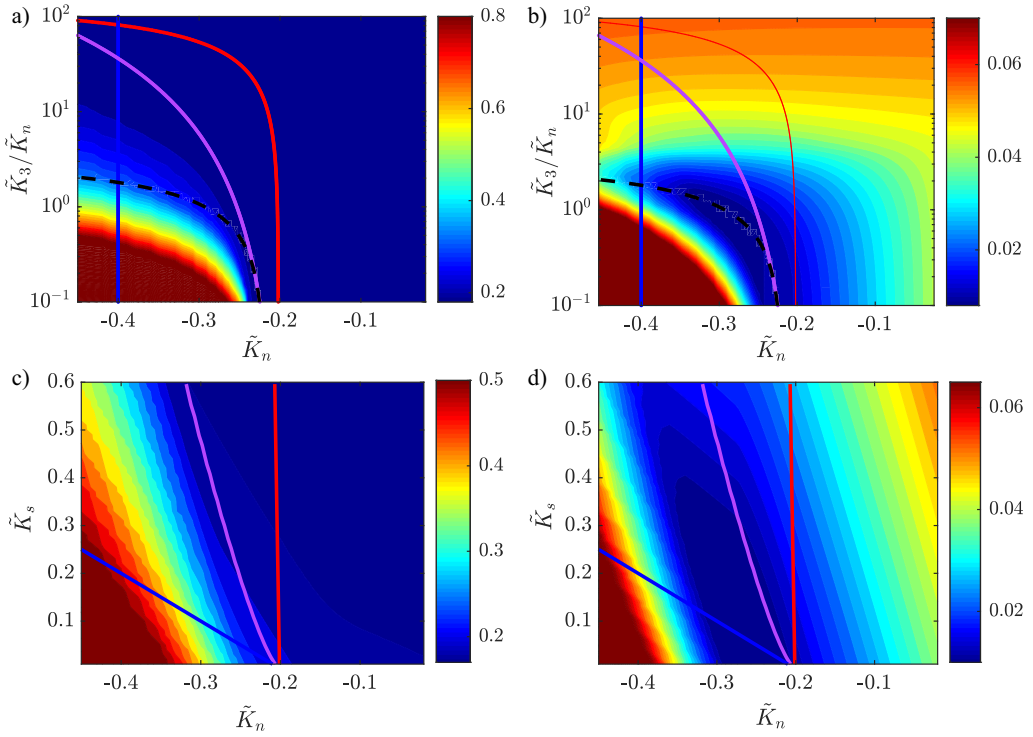

Figure 5.13: Performance maps in terms of RMS of DSCs (left) and ASCs (right) in the ($\tilde{K}_n$, $\tilde{K}_3$) space with $\tilde{K}_s = 0.2$ (top) and in the ($\tilde{K}_n$, $\tilde{K}_s$) space with $\tilde{K}_3/\tilde{K}_n = 1.26$ (bottom) for a pulse amplitude of 0.5. The transition curves between stability region are denoted by red, violet and blue lines and the analytical prediction of optimum values by black dashed line.

controlled grow, but for large pulse amplitudes a loss of performance is observable. Finally, the configuration optimized for $\tilde{A} = 1$ shows the major robustness effectively controlling all the range of pulse amplitudes. In Fig. 5.16 the curves of DSCs and AASCs peaks vs. the pulse amplitudes are reported for the three systems optimized respectively for $\tilde{A} = (0.3, 0.5, 1)$. Note that the configuration optimized for $\tilde{A} = (0.3, 0.5)$ show a slightly better performance for the optimizing amplitudes (0.3, 0.5) then the configuration optimized for $\tilde{A} = 1$, but for larger pulse amplitudes the latter configuration is strongly more effective. From this we can assume that the best configuration for effectively controlling the accelerations along a certain range of pulse amplitudes $0 < \tilde{A} < \tilde{A}_{max}$ is the one optimized for the single amplitude $\tilde{A}_{max}$. In order to confirm this assumption, a numerical optimization using a genetic algorithm (Differential Evolution algorithm) is performed adopting as performance parameter the RMS of the curve of the peaks of ASCs vs. pulse amplitudes within a range of $0 < \tilde{A} < 1$.

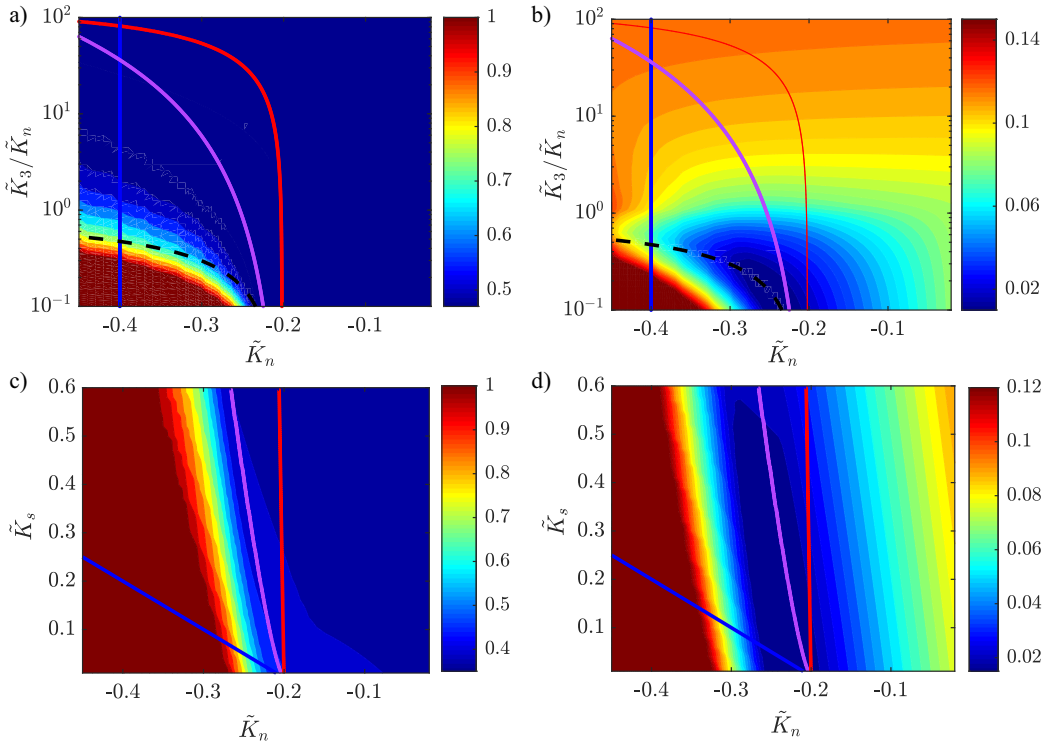

Figure 5.14: Performance maps in terms of RMS of DSCs (left) and ASCs (right) in the ($\tilde{K}_n$, $\tilde{K}_3$) space with $\tilde{K}_s = 0.2$ (top) and in the ($\tilde{K}_n$, $\tilde{K}_s$) space with $\tilde{K}_3/\tilde{K}_n = 0.15$ (bottom) for a pulse amplitude of 1. The transition curves between stability region are denoted by red, violet and blue lines and the analytical prediction of optimum values by black dashed line.

The search spaces relative to $\tilde{K}_n, \tilde{K}_3$ parameter values are respectively $0 < \tilde{K}_n < -0.5$ and $10^{-2} < \tilde{K}_3/\tilde{K}_n < 10^2$. The number of candidates for each generation is 20 while the number of generations is 100. In Fig. 5.17 the evolution of best candidate solutions and the final optimum solution provided by the DE algorithm are reported. In particular, the candidate solutions are tracked in the parameters ($\tilde{K}_n$, $\tilde{K}_3$) space and the associated curves of AASCs peaks vs. pulse amplitudes is shown together with the RMS of the curve vs. iteration. Note that DE results confirm the previous assumption, an optimum configuration that effectively control the response within the entire pulse amplitudes range $0 < \tilde{A} < \tilde{A}_{max}$ is quiet coincident with the one optimized on the single amplitude $\tilde{A} = \tilde{A}_{max}$.

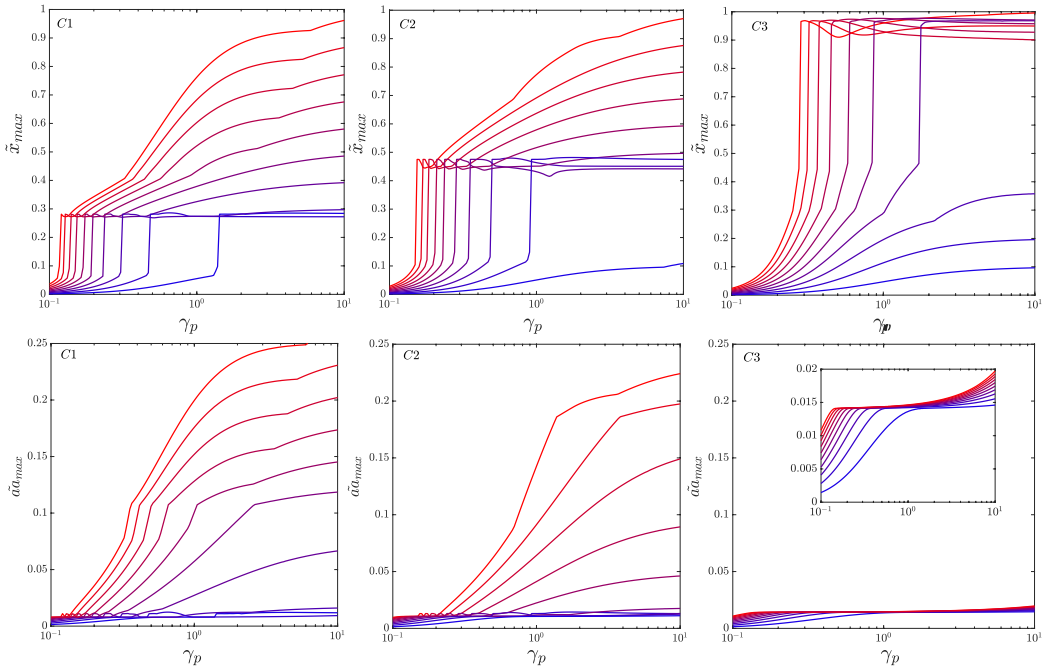

Figure 5.15: DSCs (top) and ASCs (bottom) curves for the optimized configurations $C1$, $C2$ and $C3$, (left, center and right, respectively) under P1 pulse load with amplitudes $\tilde{A} = [0.1 : 0.1 : 1]$.

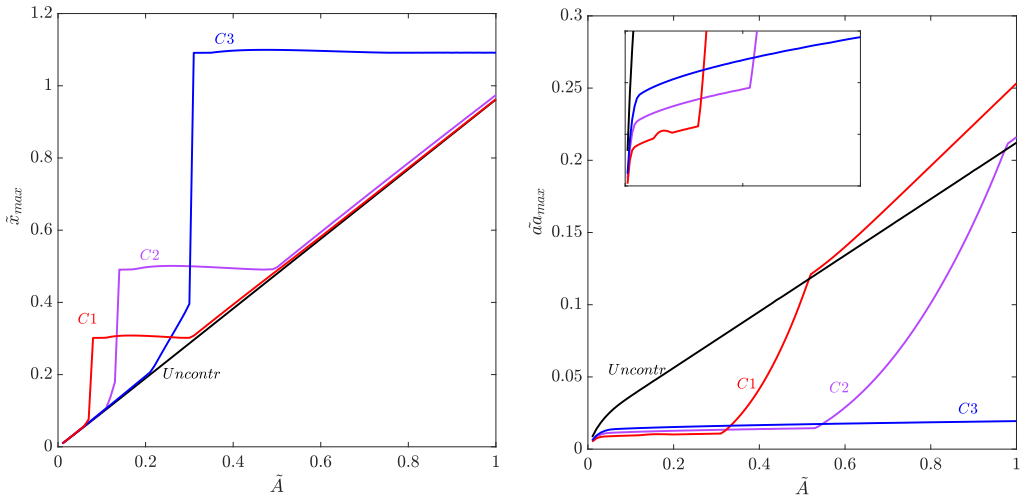

Figure 5.16: Curves of DSCs and ASCs peaks vs. pulse amplitudes for the uncontrolled configuration (black line) and for the systems optimized for $\tilde{A} = (0.3, 0.5, 1)$ (in red, violet and blu line, respectively).

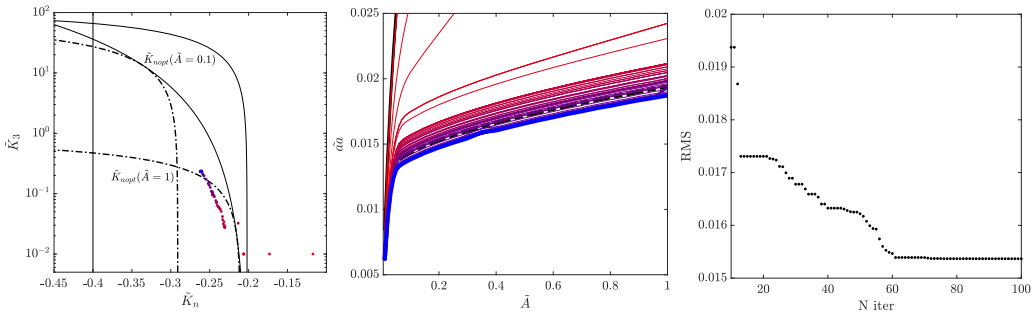

Figure 5.17: Candidate solutions tracked in the parameters ($\tilde{K}_n$, $\tilde{K}_3$) space (left), associated curves of AASCs peaks vs. pulse amplitudes (center) and RMS of the ASCs peaks vs. pulse amplitudes curves vs. iteration number (right).

5.3 Response to P2

The same parametrical investigation in the parameters ($\tilde{K}_n$, $\tilde{K}_3$) space is done also for the second and third pulse types. Here the main numerical results relative to the response of the system forced by the second pulse type are reported. In Fig. 5.18 performance contour plots and analytical prediction of optimum parameters combination are reported for pulse amplitudes $\tilde{A} = (0.3, 0.5, 1)$. Similarly to the response associated with the first pulse type, the optimum combinations of the parameters $\tilde{K}_n$, $\tilde{K}_3$ lies in the tri-stable region, but, this time, closer to the transition curve STr-TSr.
In Fig. 5.19 time histories of the uncontrolled system, of the optimized configuration for $\tilde{A} = 0.5$ and of a controlled but not optimized configuration are reported for a pulse load P2 with $\gamma_p = 0.5$ and $\tilde{A} = 0.5$. Note that for the optimized configuration the lateral stable equilibrium strongly slows down the mass and then trap it in $\tilde{x}_{f0u} = \tilde{A}$. On the other hand, in the not optimized configuration response, the potential well trap the mass, but, because its location is larger than the pulse amplitude, there is an amplification of displacements and accelerations.
The system with three different configurations associated with the optimum numerical combinations $\tilde{K}_n$, $\tilde{K}_3$ for pulse amplitudes $\tilde{A} = (0.3, 0.5, 1)$ ($C1'$, $C2'$ and $C3'$, respectively) is considered and, for each configuration, the shock curves are obtained for a pulse amplitudes range $\tilde{A} = [0.1 : 0.1 : 1]$ (see Fig. 5.20).
Also for this type of pulse, the configuration optimized on $\tilde{A} = 1$ shows the best performance in terms of accelerations reduction in the entire pulse amplitudes range. Note that, unlike the first pulse type, no jumping in AASCs and DSCs exists. In Fig. 5.21 curves of ASCs and DSCs peaks vs. the pulse amplitudes are reported for the three systems $C1'$, $C2'$ and $C3'$. Note that all configurations, unlike first pulse type, show a displacements reduction together to an accelerations

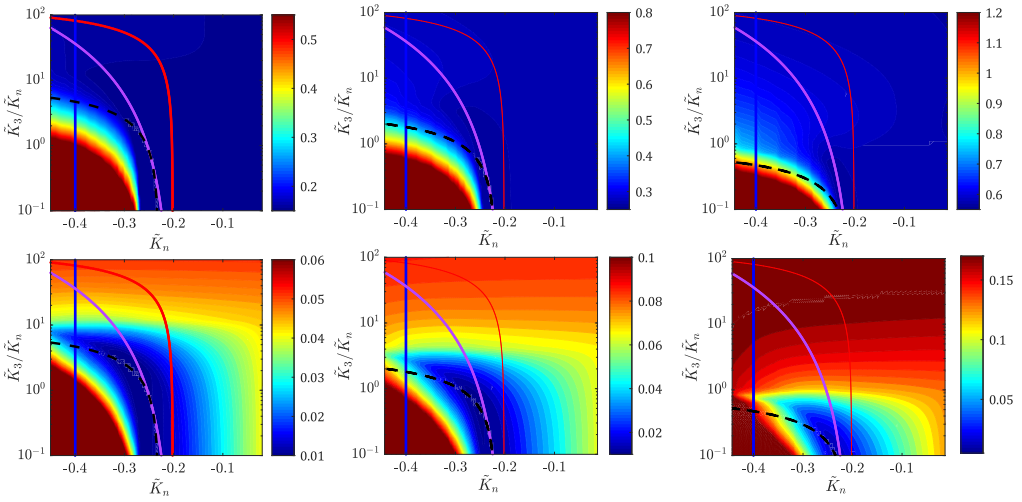

Figure 5.18: Performance maps in terms of RMS of DSCs (top) and ASCs (bottom) in the ($\tilde{K}_n$, $\tilde{K}_3$) space with $\tilde{K}_s = 0.2$ for pulse amplitudes $\tilde{A} = (0.3, 0.5, 1)$ (left, center and right respectively). The transition curves between stability region are denoted by red, violet and blue lines and the analytical prediction of optimum values by black dashed line.

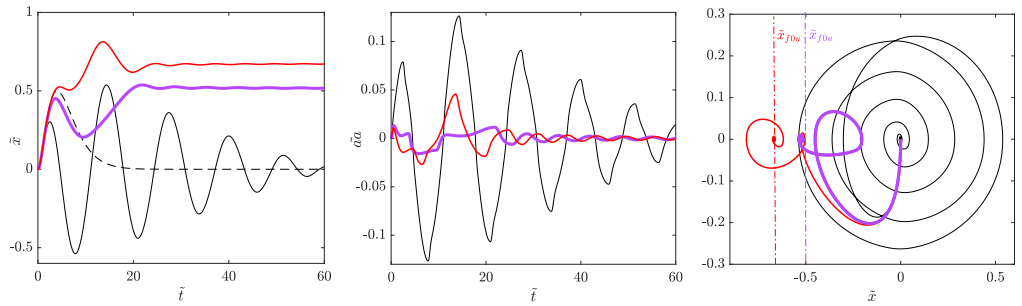

Figure 5.19: Time histories of displacements (left) and accelerations (right) and phase portraits (right) for the uncontrolled, the controlled optimized and the controlled not optimized systems (in black, violet and red line, respectively) under pulse load P2 with $\gamma_p = 0.5$ and $\tilde{A} = 0.5$.

reduction. Also for this type of pulse the most robust configuration in terms of accelerations reduction along the entire pulse amplitudes range is the one optimized for a pulse amplitude $\tilde{A} = 1$ that shows an acceleration reduction up to 10 times.

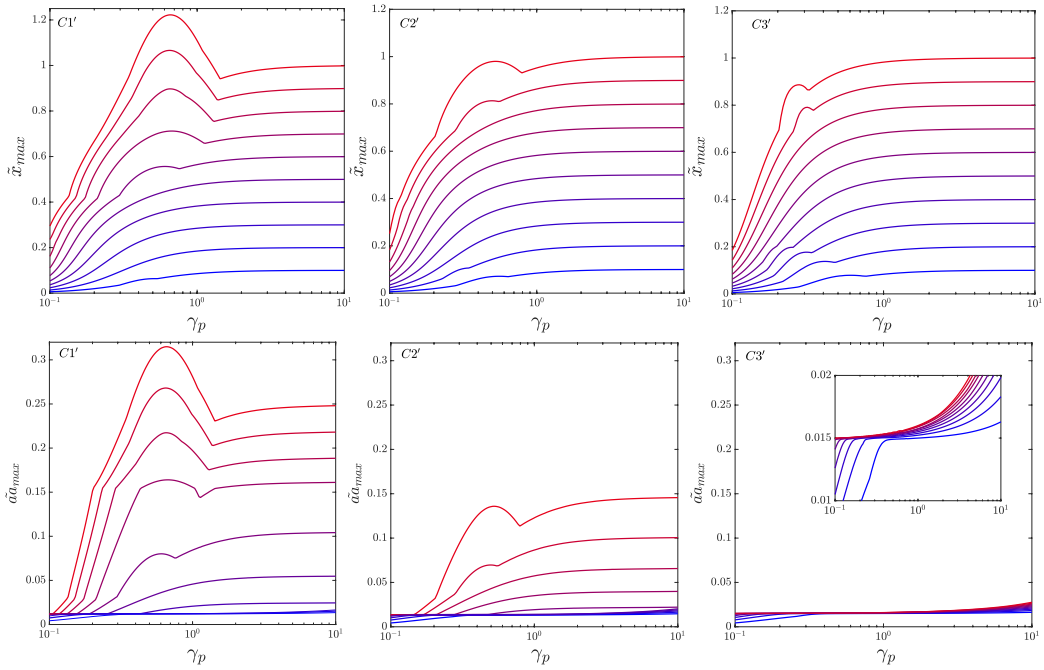

Figure 5.20: DSCs (top) and ASCs (bottom) curves for the optimized configurations $C1'$, $C2'$ and $C3'$, (left, center and right, respectively) under P2 pulse load with amplitudes $\tilde{A} = [0.1 : 0.1 : 1]$.

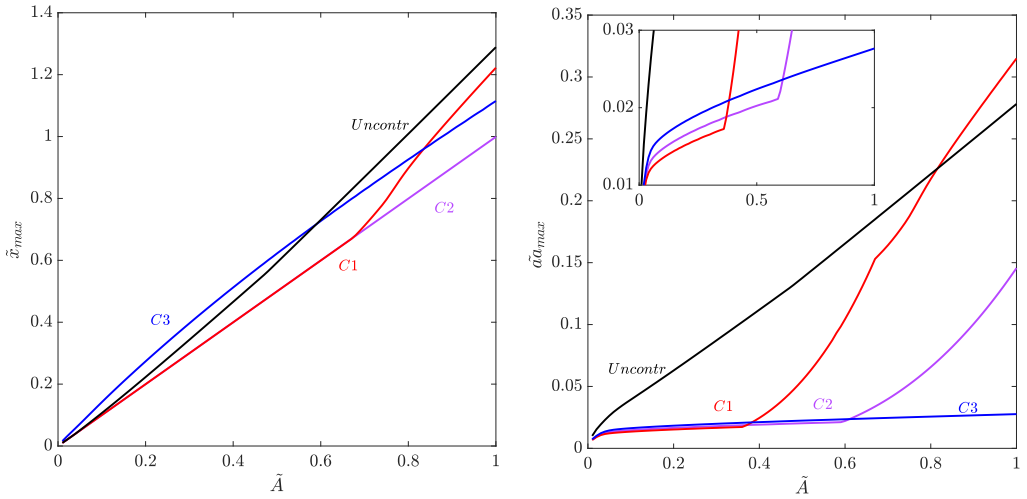

Figure 5.21: Curves of DSCs and ASCs peaks vs. pulse amplitudes for the uncontrolled configuration (black line) and for the systems optimized for $\tilde{A} = (0.3, 0.5, 1)$ (in red, violet and blu line, respectively).

5.4 Response to P3

Finally the third pulse type, oscillatory displacement step, is investigated in the parameters ($\tilde{K}_n$, $\tilde{K}_3$) space. Like the other pulse types, performances of the isolated system under the third pulse type are studied in terms of control of peak and the RMS values of AASCs. As well as under first pulse type, the optimum parameters combinations for the system under the third pulse type are the ones that show $\tilde{x}_{f0u}$, location of the lateral stable equilibrium, equal to the asymptotic ground displacement. Unlike round displacement step, in the oscillatory displacement step the asymptotic ground displacement is not equal to the maximum amplitude of motion $\tilde{A}$, but is equal to $0.858\tilde{A}$, then optimum parameters combinations are the ones that show $\tilde{x}_{f0u} = 0.858\tilde{A}$. In Fig. 5.22 performance contour plots and analytical prediction of optimum parameters combinations are reported for pulse amplitudes $\tilde{A} = (0.3, 0.5, 1)$.

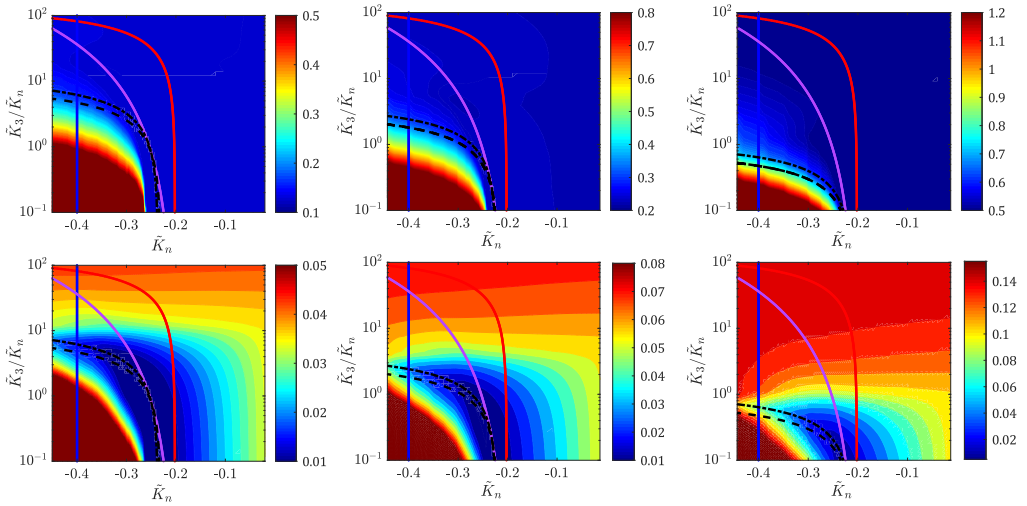

Figure 5.22: Performance maps in terms of RMS of DSCs (top) and ASCs (bottom) in the ($\tilde{K}_n$, $\tilde{K}_3$) space with $\tilde{K}_s = 0.2$ for pulse amplitudes $\tilde{A} = (0.3, 0.5, 1)$ (left, center and right respectively). The transition curves between stability region are denoted by red, violet and blue lines and the analytical prediction of optimum values by black dashed line.

In Fig. 5.23 time histories of the uncontrolled system, of the optimized configuration for $\tilde{A} = 0.5$ and of a controlled but not optimized configuration are reported for a pulse load P2 with $\gamma_p = 0.5$ and $\tilde{A} = 0.5$.
The system with three different configurations associated with the optimum numerical combinations $\tilde{K}_n$, $\tilde{K}_3$ for pulse amplitudes $\tilde{A} = (0.3, 0.5, 1)$ ($C1''$, $C2''$ and $C3''$, respectively) is considered and, for each configuration, the shock curves are obtained for a pulse amplitudes range $\tilde{A} = [0.1 : 0.1 : 1]$ (see Fig. 5.24). About

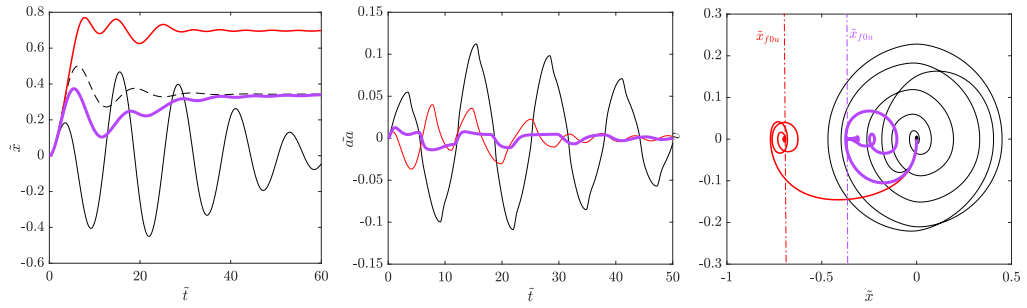

Figure 5.23: Time histories of displacements (left) and accelerations (right) and phase portraits (right) for the uncontrolled, the controlled optimized and the controlled not optimized systems (in black, violet and red line, respectively) under pulse load P3 with $\gamma_p = 0.5$ and $\tilde{A} = 0.5$.

ASCs, the same considerations of the previous pulse types in terms of reduction and robustness are done. Regarding the DSCs, note the existence of a local peak that grow with the increase of optimizing pulse amplitude. Analyzing time his-

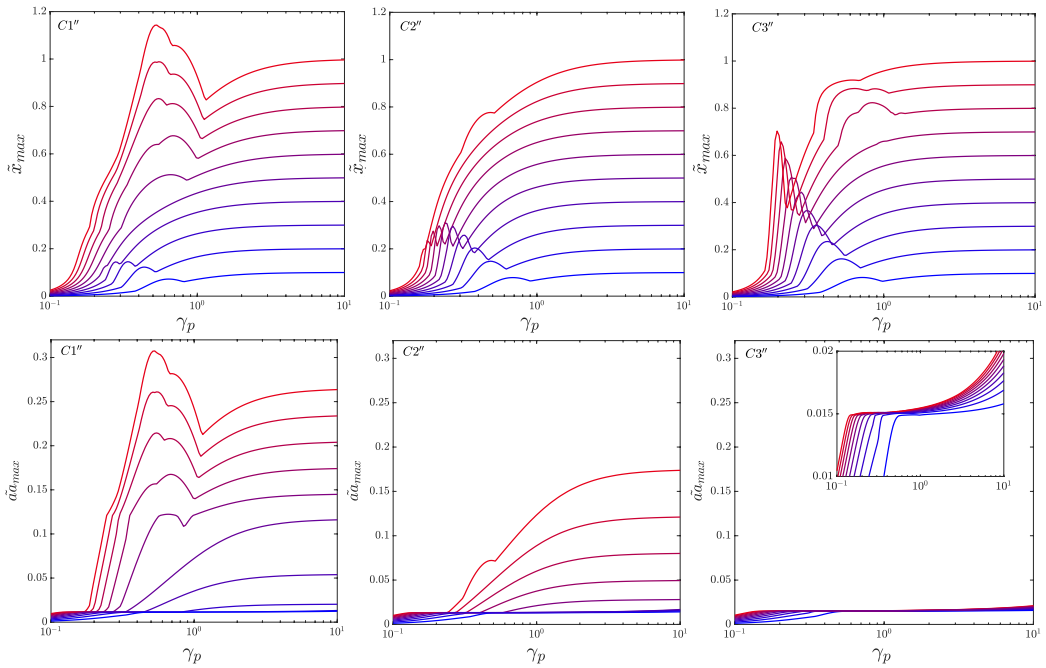

Figure 5.24: DSCs (top) and ASCs (bottom) curves for the optimized configurations $C1''$, $C2''$ and $C3''$, (left, center and right, respectively) under P3 pulse load with amplitudes $\tilde{A} = [0.1 : 0.1 : 1]$.

tories associated with the first peak, to the minimum and to the second peak of

DSCs for pulse amplitude $\tilde{A} = 1$ with the system in the $C3''$ configuration (see Fig. 5.25), is seen that these peaks are due to mass trapping by the lateral positive stable, positive unstable and negative stable equilibrium, respectively. Despite this alternating attraction strongly modulates DSCs, it does not affect the ASCs.

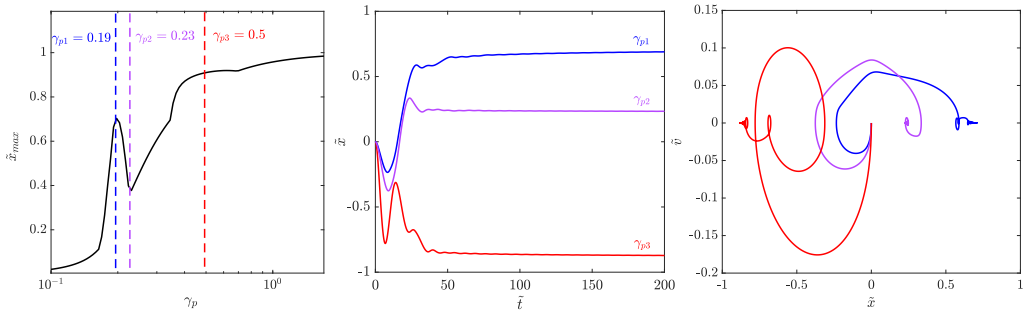

Figure 5.25: DSCs curve of the $C3''$ configuration under P3 pulse load with $\tilde{A} = 1$ (left), time histories of displacements (center) and phase portraits (left) associated with $\gamma_p = 0.19, 0.23, 0.5$ in blu, violet and red line, respectively.

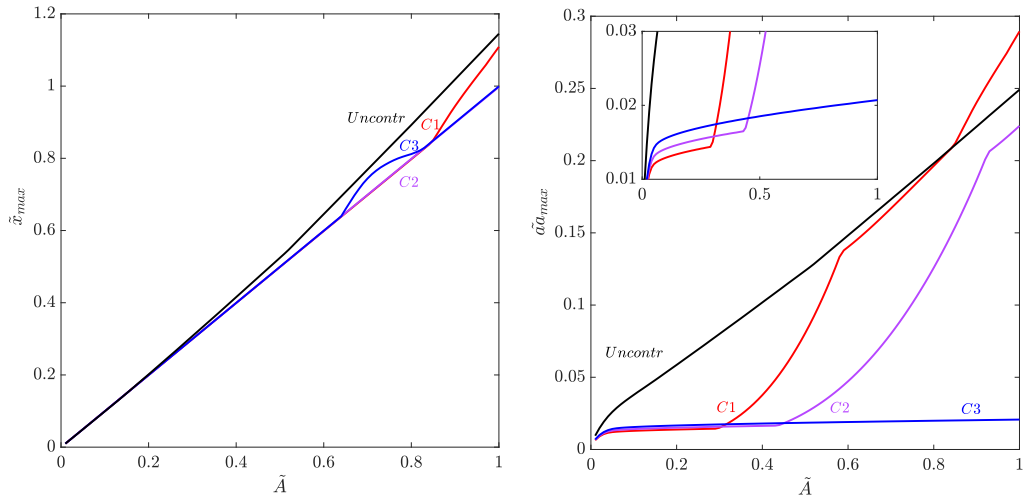

Figure 5.26: Curves of DSCs and ASCs peaks vs. pulse amplitudes for the uncontrolled configuration (black line) and for the systems optimized for $\tilde{A} = (0.3, 0.5, 1)$ (in red, violet and blu line, respectively).

In Fig. 5.26 the curves of ASCs and DSCs peaks vs. the pulse amplitudes are reported for the three systems $C1''$, $C2''$ and $C3''$. Note that all configurations, like second pulse type, show a displacements reduction together to an accelerations

reduction. Most robust configuration in terms of accelerations reduction along the entire pulse amplitudes range is, also for this type of pulse, the one optimized for the pulse amplitude $\tilde{A} = 1$.

5.5 Conclusions

The response of the proposed isolation system under three pulse types of ground motion (P1, P2, P3) is parametrically investigated for different values of design parameters. The well-trapping phenomenon is showed and its beneficial effect on the control of accelerations under shock excitation are demonstrated and exploited. Analytical formula of optimum parameters combination under a specific pulse amplitude are provided imposing the location of the lateral stable equilibrium equal to the pulse amplitude. The analytical predictions on optimum parameters combination are validated by comparison with the minimum of numerical performance maps and with the results of Differential Evolution algorithm. Exploiting Tri-stability and the well-trapping phenomenon, for all pulse types an accelerations reduction up to 10 times is achieved and, except the first pulse type, also displacements result slightly reduced. In addition, it is important to highlight the existence of a zone with high performances in the snap-through region, which allows strong reductions in acceleration (70%) at the same time of self-recentering capacity.

Chapter 6

Investigation on MDOF isolated structure NS-SMA damped under seismic excitation

In order to validate the improvement of isolation performances produced by the proposed system, in this chapter the response of a MDOF structure controlled by a Negative stiffness - Superelastic isolation under seismic excitation is studied.

6.1 Description of MDOF structure and site seismic hazard

The benchmark structure is a common multi-storey building with reinforced concrete frames. The structure is laid out in a grid of 3x3 bays, with a length of 5 meters each, while the height of floors is of 3.3 m. The weight of the standard floor under seismic combination has been assumed equal to $10kN/m^2$, and the columns with a square section with sides of length 0.45 m. Hence, the mass and the stiffness of each storey are respectively equal to $256Ton$ and $365kN/mm$, and the period of the first vibration mode results equal to $0.58s$. By designing the seismic isolation system according to NTC-18 code, it is required an increase in the period of the first mode such that $T_{is} < 3T_{fb}$. Therefore, the isolation system was designed to ensure that the period of the structure is higher than 1.8 seconds and results in 16 elastomeric isolators with an elastic stiffness of $1.05kN/mm$. The building is located in the town of Avezzano (seismic zone I), has a nominal life of 50 years and use class III. The soil class is C, while the topographic category is T1. In Fig. 6.1 planimetric and elevation views of the building are reported. Figure 6.2 shows the elastic response spectra in terms of pseudo accelerations and displacements for the selected site for to the four limit states defined by the NTC-18 code: operativ-

ity limit state, damage limit state, life limit state and collapse limit state, in Italian SLO, SLD, SLV, SLC respectively. These limit states are associated with the following exceedance probabilities: $P_{vr} = 81\%, P_{vr} = 63\%, P_{vr} = 10\%, P_{vr} = 5\%$.

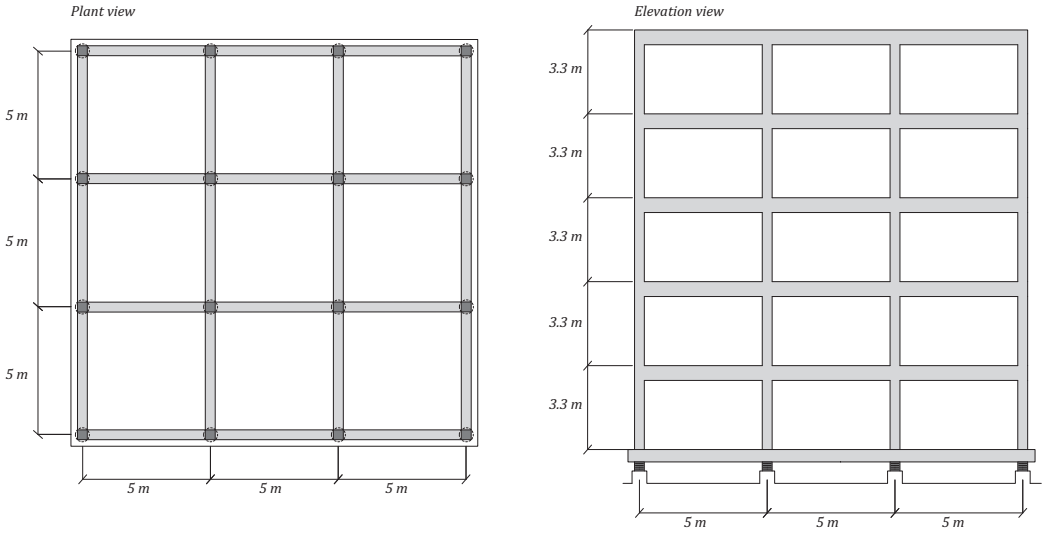

Figure 6.1: Horizontal (right) and frontal (right) schematic view of the benchmark building structure.

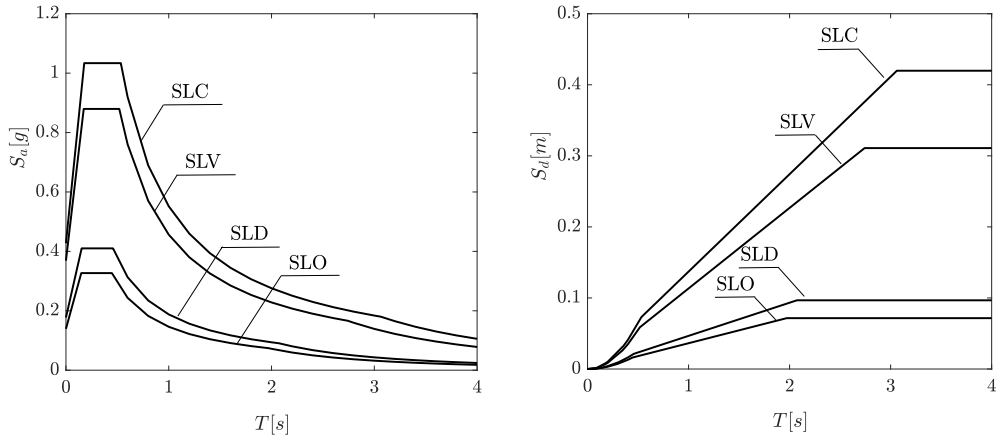

Figure 6.2: Response spectra for limit states SLO, SLD, SLV, SLC in terms of pseudo accelerations (left) and displacements (right).

In the subsequent sections the response of the isolated building subject to groups of spectrum-compatible artificial accelerograms is investigated. The isolated building is modeled as a 6-DOF system composed by the superposition in series of

6 oscillator with floor shear stiffness ($k_f = 365kN/mm$) and translational mass ($m_f = 256Ton$) and with a damping coefficient $c_f = 0.5kNs/mm$ (see Fig. 6.3). The first mass is connected to the ground with the rheological model described in precedent chapters, representative of the elastomeric isolation system (EIS) and of the NS-SMA contribution. The EIS has been modelled via a Bouc-Wen model plus a viscous damping with $K_i = 84, \alpha K_i = 16.4, \gamma = 0.01, \beta = 0.09, n = 1$ and $c = 0.1$.

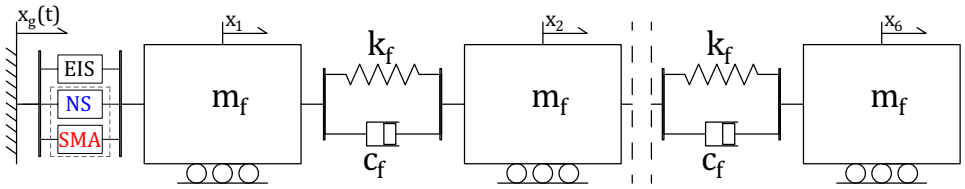

Figure 6.3: 6-DOF dynamic model of the isolated building.

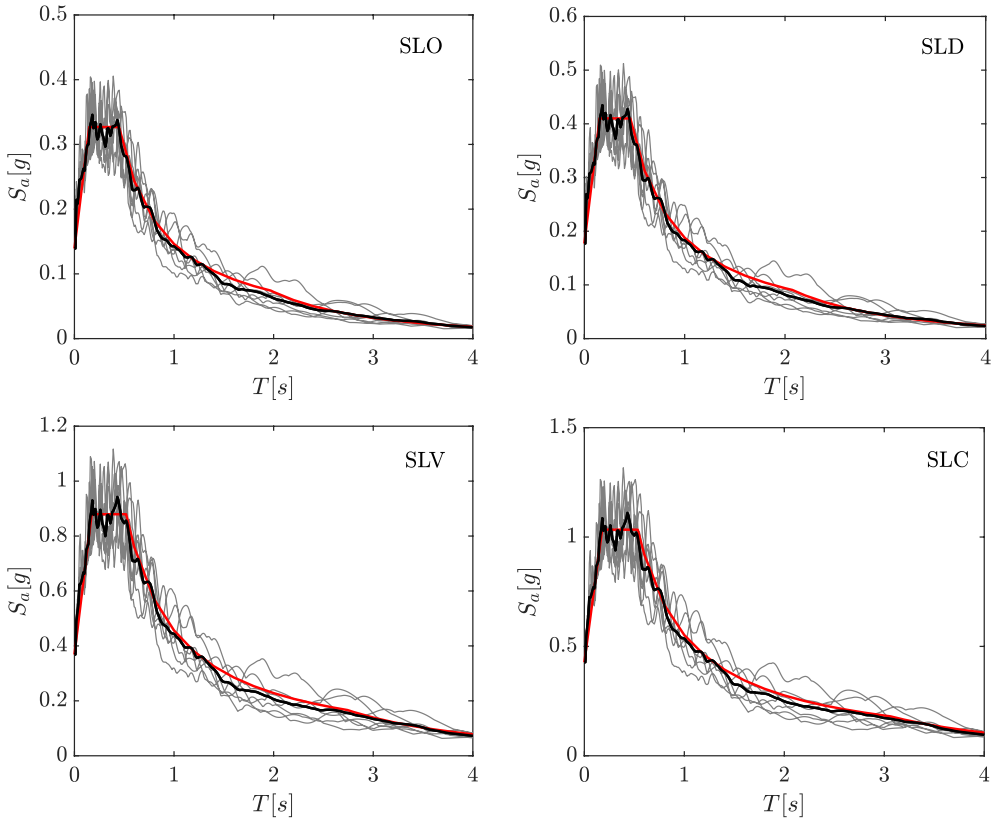

Figure 6.4: Acceleration Response Spectra of the 7 accelerograms (gray lines), mean RS (black lines) and design RS (red lines) for the limit states SLO, SLD, SLV and SLC.

For each limit state, a group of 7 spectrum-compatible accelerograms is generated with SIMQKE software with a tolerance between the mean acceleration response spectra and the design acceleration response spectra of $\pm 10\%$ (see Fig. 6.4). The corresponding 7 ground accelerations time histories are applied to the 6-DOF system.

6.2 Optimization of response at SLC

The optimum NS-SMA configuration in terms of force transmissibility for different maximum displacements threshold is researched by mean of the Differential Evolution Algorithm. The design parameters are the Negative stiffness coefficient K_n, the cubic stiffness coefficient K_3, and the elastic stiffness of the super-elastic term K_s. The gap displacement x_{gap} is set equal to $25mm$ and the hysteresis ratio y_s equal to 0.8. The adopted research spaces for the three design parameters are the following: $-50kN/mm < K_n < 0kN/mm$, $10^{-7}/mm^2 < -K_3/K_n < 10^{-4}/mm^2$ and $0kN/mm < K_S < 70kN/mm$. The size of the population is of 12 members and the number of iterations is 150. The mean value of the base shear peaks (V^j_{max}) exhibited by the isolated building subject to the group of 7 accelerograms associated with the collapse limit state (SLC) (see Fig. 6.5) is assumed as the objective function of the optimization procedure. The constraint on maximum displacement is added by introducing a term in the objective function equal to 0 if the mean of the maximum displacements (D^j_{max}) is smaller than the limit displacement (D_{lim}) and equal to 10^6 if it is greater than the limit displacement.

$$OBJ = \frac{\sum_{j=1}^{n_{acc}} V^j_{max}}{n_{acc}} + \frac{1 + sign\left(\frac{\sum_{j=1}^{n_{acc}} D^j_{max}}{n_{acc}} - D_{lim}\right)}{2} 10^6; \tag{6.1}$$

The displacement threshold can be considered as a design parameter, function of the intention of the designer to minimize more forces or displacements. For the subsequent optimizations, five different displacement thresholds are considered as ratio of the mean of the maximum displacements exhibited by the building isolated with the baseline system (elastomeric isolation). In particular the following values for D_{lim} are adopted: $0.7, 0.8, 0.9, 1, 1.1(\frac{\sum_{j=1}^{n_{acc}} D^j_{max}}{n_{acc}})_{BS}$. The described thresholds correspond to a reduction in the mean of peak displacements of $30, 20, 10, 0\%$, respectively, while the last threshold corresponds to an amplification of 10% and it represent the possible scenario where a larger displacement can be admitted.

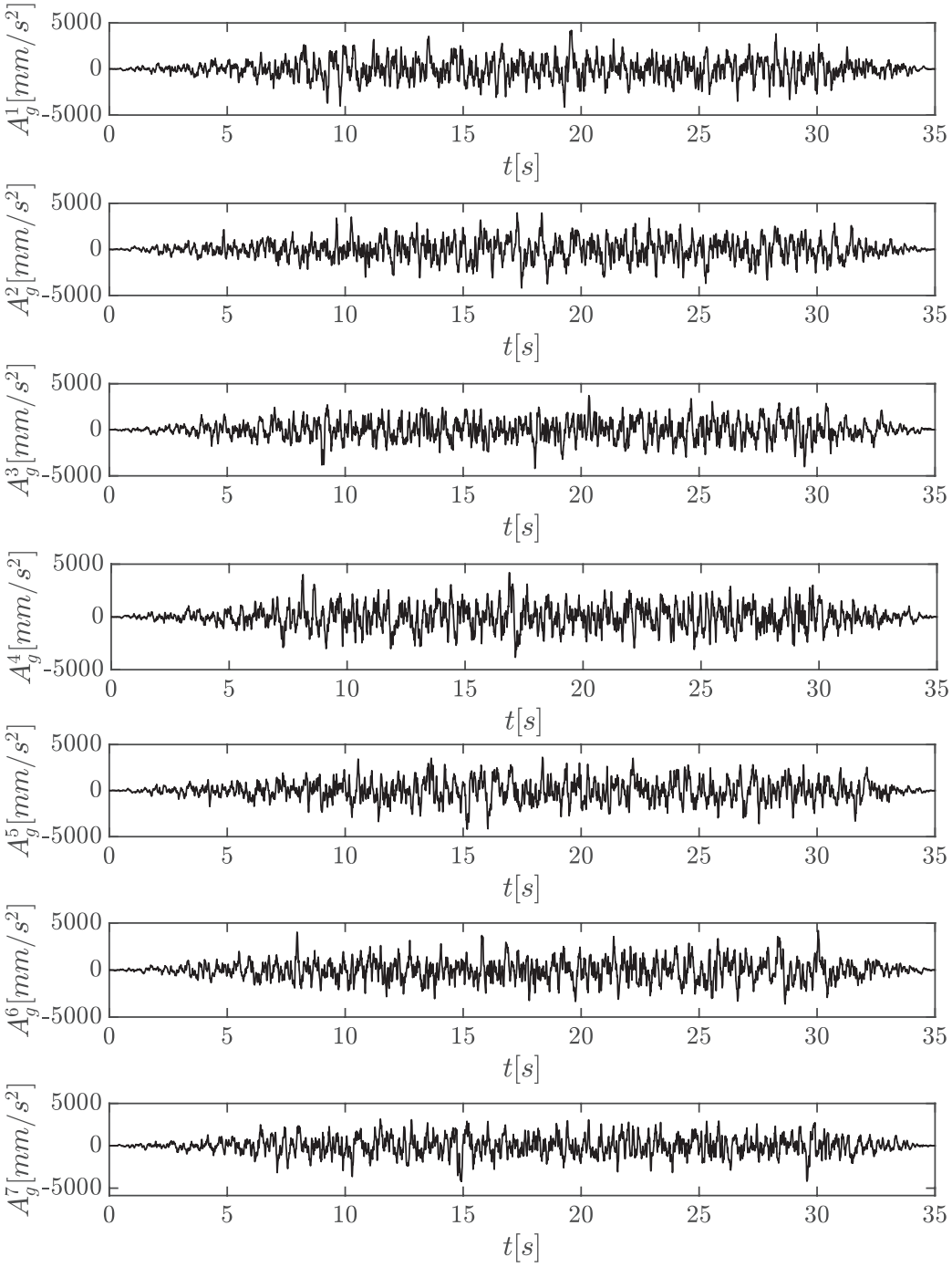

Figure 6.5: Ground acceleration time histories of the 7 accelerograms of SLC group .

6.2.1 Optimal configurations

The optimal configuration for each displacement thresholds are find and reported in Tab.6.1 together with the associated variations with respect to the baseline system in terms of the mean values of V_{max} and D_{max}.

	$K_n \left[\frac{kN}{mm}\right]$	$\frac{K_3}{K_n}\left[\frac{1}{mm^2}\right]$	$K_s \left[\frac{kN}{mm}\right]$	$V_{max,m}[kN]$	$D_{max,m}[mm]$	$\Delta V_{max,m}$ [%]	$\Delta D_{max,m}$ [%]
Baseline system (S1)	0	0	0	2829	200	~	~
NS-SMA damped system (S3)							
D_{lim} = 140 mm	-17.52	1.80E-05	43.32	2012	139	-29%	-31%
D_{lim} = 160 mm	-12.68	1.80E-07	26.09	1589	158	-44%	-21%
D_{lim} = 180 mm	-24.46	9.77E-06	25.61	1257	181	-56%	-10%
D_{lim} = 200 mm	-19.21	5.48E-06	15.89	974	194	-66%	-3%
D_{lim} = 220 mm	-18.6	2.60E-06	12.67	900	210	-68%	5%
SMA damped system (S2)							
D_{lim} = 140 mm	0	0	43.32	3096	137	9%	-32%
D_{lim} = 160 mm	0	0	26.09	2892	159	2%	-21%
D_{lim} = 180 mm	0	0	25.61	2892	160	2%	-20%
D_{lim} = 200 mm	0	0	15.89	2750	160	-3%	-20%
D_{lim} = 220 mm	0	0	12.67	2750	164	-3%	-18%

Table 6.1: Mean V_{max} and D_{max} and variations for the baseline system, for the optimized NS-SMA configurations and for the associated SMA damped system.

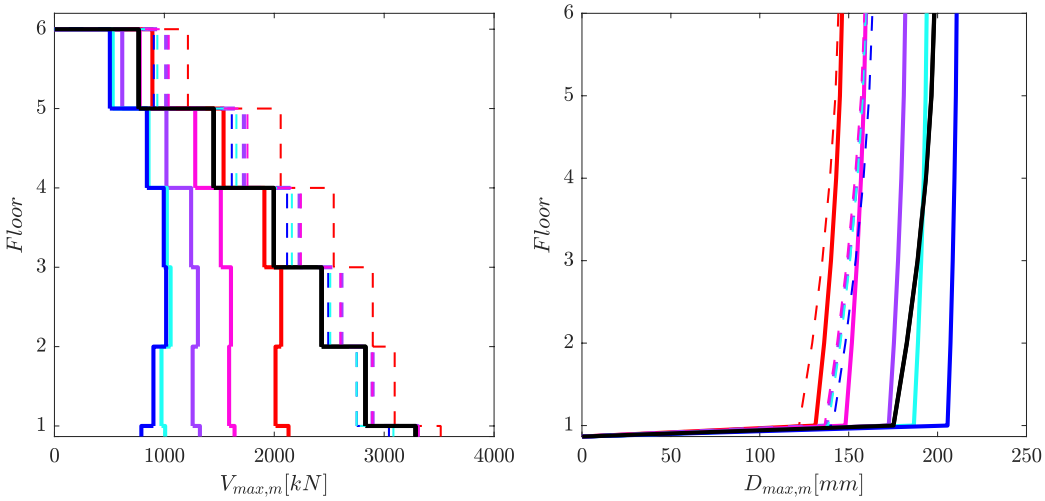

Figure 6.6: Mean of storeys shear (left) and displacement (right) peaks for the baseline system (in black lines), for the NS-SMA damped system optimized for $D_{lim} = 0.7, 0.8, 0.9, 1.0, 1.1 D_{max,m}$ in red, magenta, violet, ciano and blue lines respectively and for the associated SMA damped system in dashed lines.

As can be observed in Tab.6.1 and in Fig. 6.6, the introduction of SMA damping produces an increase of the mean of base shear peaks of 9% and a decrease

of maximum displacements of 31%. On the other hand, with the NS-SMA damping a stronger improvement of performances can be achieved. In fact, in the case $D_{lim} = 1.0, 1.1 D_{max,m}$, the attainable decrease of base shear peaks is respectively of 66% and 68%. In addition, it is interesting to note that these two configurations are able to retain the maximum drift under the threshold $Dr = 0.2\%$, usually considered the start damage drift. For displacement reductions of $10, 20, 30\%$ the base shear reductions achievable are of $56, 44, 29\%$ respectively.

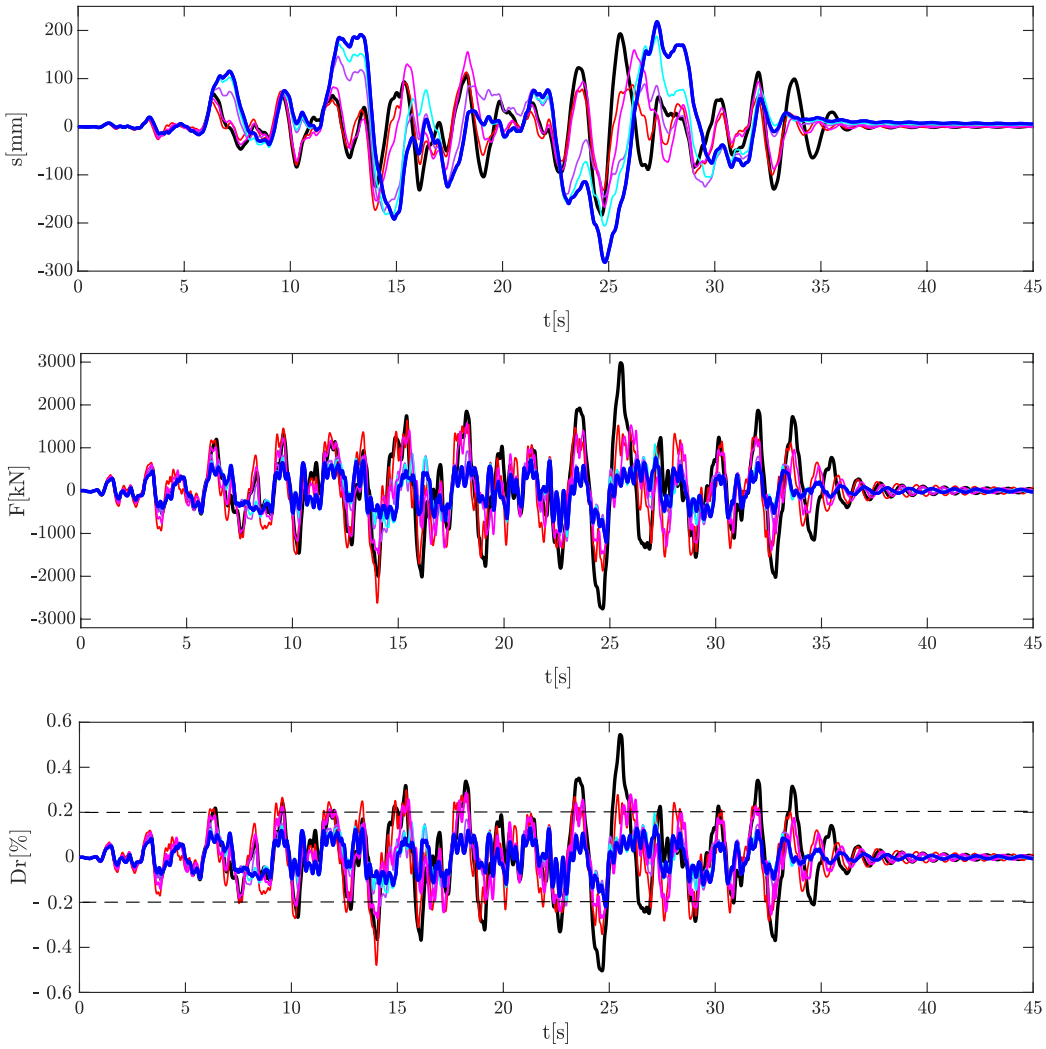

Figure 6.7: Displacement (top), base shear (center) and base drift (bottom) for the baseline system (in black lines), for the NS-SMA damped system optimized for $D_{lim} = 0.7, 0.8, 0.9, 1.0, 1.1 D_{max,m}$ (in red, magenta, violet, ciano and blue lines respectively) subject to the 5^{th} acclerogram of SLC group.

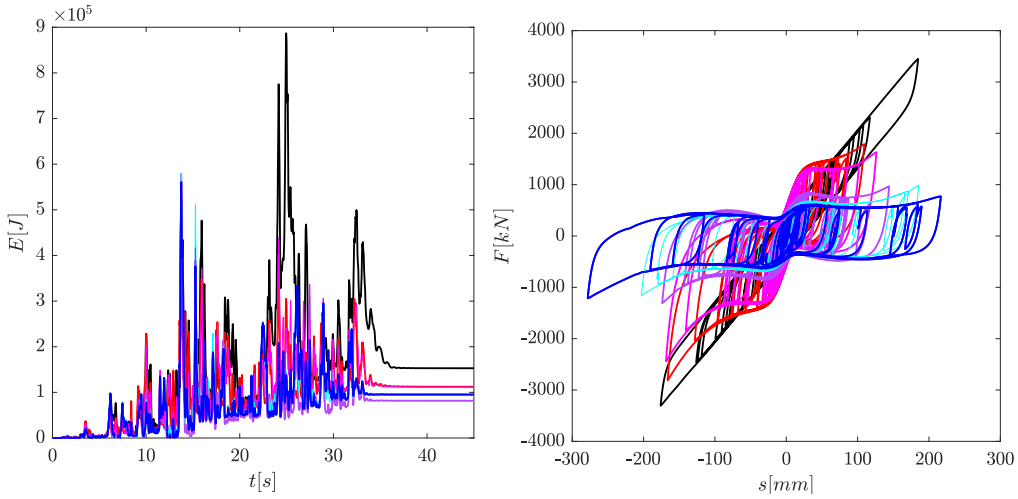

Figure 6.8: Energy (left) and hysteretic cycles (right) for the baseline system (in black lines), for the NS-SMA damped system optimized for $D_{lim} = 0.7, 0.8, 0.9, 1.0, 1.1 D_{max,m}$ (in red, magenta, violet, ciano and blue lines respectively) subject to the 5^{th} acclerogram of SLC group.

These results prove that with NS-SMA damping strong reductions in displacement and shear can be achieved at the same time and reveal the strong tunability of the proposed damping system. In fact, by calibrating the main design parameters the designer can select a configuration that reduces only base shear (-68%) or a configuration that decreases both base shear and maximum displacement (-29% and -31%, respectively). This is a peculiar characteristic of the NS-SMA damping not achievable with other source of damping. Indeed, as can be observed for the SMA damped configuration (S2), by introducing damping devices a decrease in displacement is attained but at the same time of an increase of base shear and acceleration due to the stiffening effect of the inserted damping. Fig. 6.7 and Fig. 6.8 shows displacement, base shear, base drift and energy time histories of the baseline system, of the SMA damped system and of the NS-SMA damped systems ($D_{lim} = 0.7, 0.8, 0.9, 1, 1.1 D_{max,m}$) subject to the 5^{th} SLC accelerogram. The strong base shear and drift reduction achievable can be noted, both in terms of max and of RMS values, as well as the self-recentering nature of the proposed isolation system, denoted by null residual displacements. By dimensionalizing the transition stability surfaces described in previous chapters, the stability regions in the design parameters space are determined and represented in Fig. 6.9 together with the 5 configurations optimized for $D_{lim} = 0.7, 0.8, 0.9, 1, 1.1 D_{max,m}$. As can be observed and according to the findings of previous chapters, all the optimal solutions lie to the Snap-Through region. In particular, the ones optimized for larger amplitudes ($D_{lim} = 0.9, 1, 1.1 D_{max,m}$) strictly follow the Snap Trough - Tri Sta-

ble transition surface ($ST \rightarrow TS$), positioning in the described above intersection between the over damped and the Snap - Trough regions. For smaller displacement limits $D_{lim} = 0.7, 0.8 D_{max,m}$ the system requires more stiffness and damping and this result in a lower negative stiffness K_n and in an higher superelastic stiffness K_s, hence the optimal configurations deviate towards the Mono Stable - Snap Trough transition surface ($MS \rightarrow ST$).

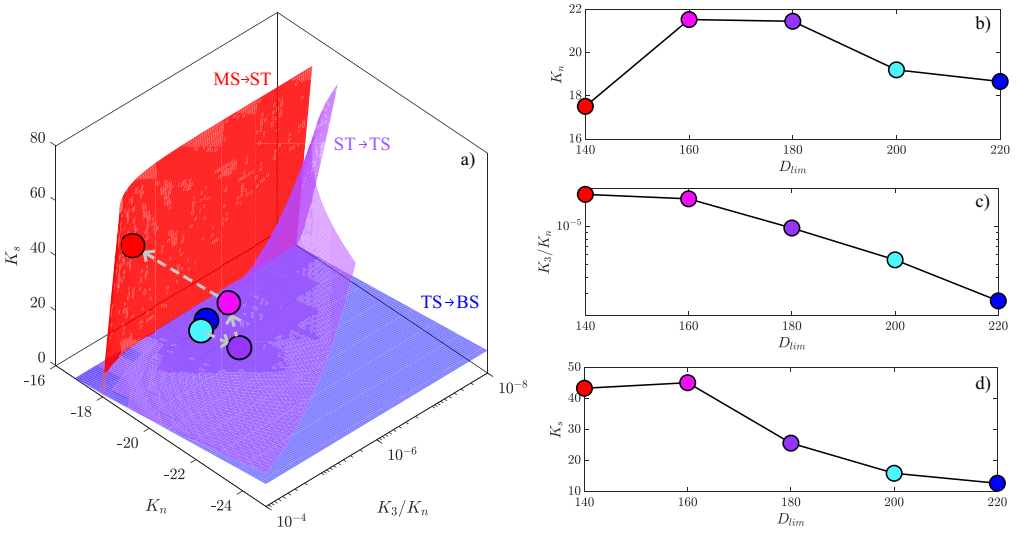

Figure 6.9: Transition surfaces and optimal configurations in 3D design parameters space (a) and trend of optimal parameters vs D_{lim} (b, c and d).

Considering that the elastic stiffness of the elastomeric isolation system is $\alpha K_i = 16.8 kN/mm$, the optimum parameters match the optimum ranges determined in the previous chapters. In fact, the optimal negative stiffness is enclosed in the range between $\alpha K_i < K_n < 1.3 \alpha K_i$, the optimal cubic stiffness between $2E-06 < K_3/K_n < 2E-05$ and the optimal superelastic stiffness in the range between $0.6 \alpha K_i < K_s < 2.5 \alpha K_i$. In Fig. 6.10 the equivalent linear stiffness K_{eq} and the equivalent damping ratio ξ_{eq} are reported in function of the oscillation amplitudes U, together with the performance point of each configuration. The configuration optimized for $D_{lim} = 0.7 D_{max,m}$ is the one with the smallest displacement required and thus the one with the highest superelastic stiffness and the lowest negative stiffness. This results in a small decrease of equivalent stiffness and in a small amplification of damping. On the other hand, by releasing the maximum displacement D_{lim}, more consistent reduction of stiffness and amplification of damping can be achieved for $D_{lim} = 0.8, 0.9, 1.0, 1.1 D_{max,m}$. The equivalent stiffness and damping can be useful to preliminary assess the performances of the NS-SMA damping system. In fact, by using the two equivalent curves of a given configuration and the design seismic demands $S_a(T, \xi)$ and $S_d(T, \xi)$, the perfor-

mance point in terms of maximum base shear and displacement can be obtained via only the static analysis of the system.

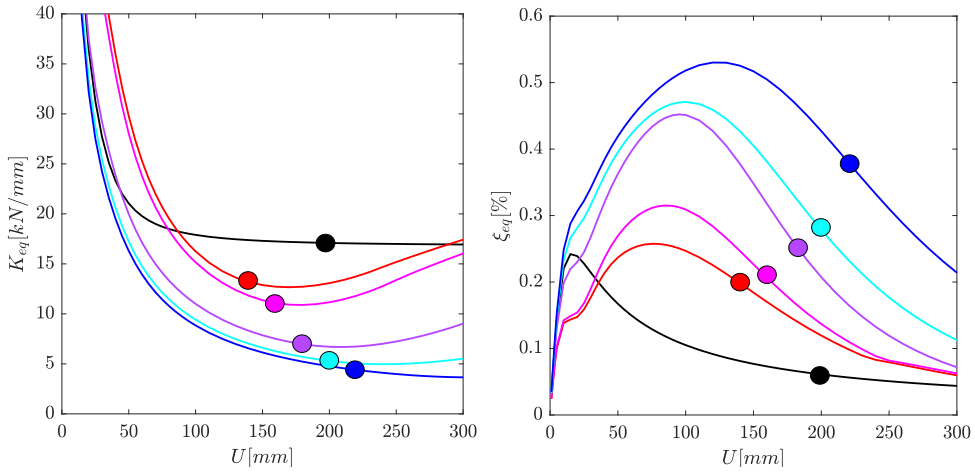

Figure 6.10: Equivalent linear stiffness K_{eq} and the equivalent damping ratio ξ_{eq} in function of the oscillation amplitudes U, together with the performance point of each configuration for the baseline isolation system (black lines) and for the NS-SMA configurations $D_{lim} = 0.7, 0.8, 0.9, 1.0, 1.1 D_{max,m}$ in red, magenta, violet, ciano and blue lines, respectively.

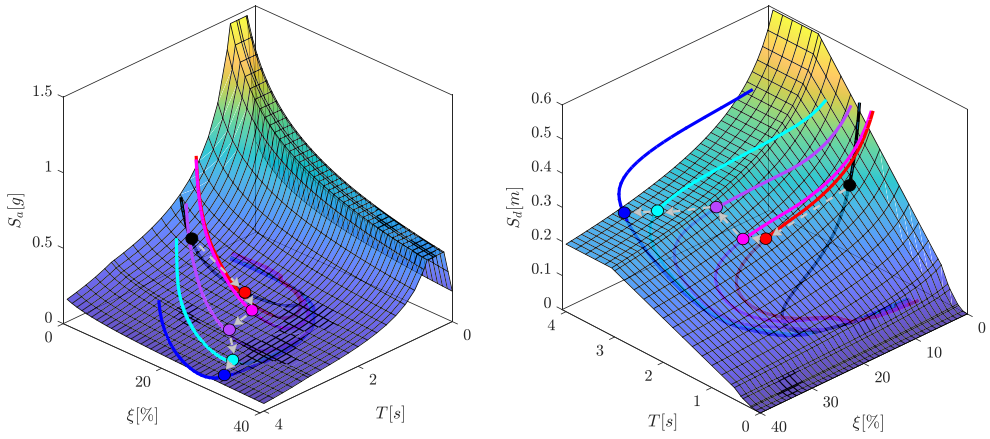

Figure 6.11: Accelerations (left) and displacements (right) seismic demand surface ($S_a(T,\xi)$ and $S_d(T,\xi)$) and C_a, C_d curves for the baseline isolation system (black lines) and for the NS-SMA configurations.

Considering that $T_{eq}(U) = 2\pi\sqrt{\sum_1^6 m_f / K_{eq}(U)}$, two three dimensional curves can be defined, representative of the evolution of maximum pseudo accelerations and displacement in function of the natural period and of the damping of the equivalent oscillator. The first curve C_a is defined by the points with coordinates $(T_{eq}(U), \xi(U), \omega^2 U)$, while the second curve C_d is identified by the points with coordinates $(T_{eq}(U), \xi(U), U)$. The intersections between the two 3D curves C_a, C_d and the demand surfaces $S_a(T,\xi)$, $S_d(T,\xi)$ indicate the performance points of the given configuration $(K_n, K_3/K_n, K_s)$ in terms of maximum pseudo acceleration and displacement (see Fig. 6.11 and Tab.6.2).

	T_{eq} $[s]$	$\xi_{eq}[\%]$	$S_a[g]$	$S_d[m]$
Baseline system (S1)	1.9	5.3	0.29	0.21
NS-SMA damped system (S3)				
$D_{lim} = 140\ mm$	2.17	18.9	0.16	0.15
$D_{lim} = 160\ mm$	2.33	21.2	0.14	0.17
$D_{lim} = 180\ mm$	2.94	24.2	0.11	0.19
$D_{lim} = 200\ mm$	3.49	27.7	0.07	0.21
$D_{lim} = 220\ mm$	3.71	36.8	0.06	0.22

Tab. 6.2: Approximated static performance points for the baseline syste and for the optimized NS-SMA configurations.

6.3 Performances for the SLO, SLD, SLV, SLC limit states

In the subsequent section, the performances of the systems optimized for the collapse limit state (SLC) are investigated under the seismic demand associated with the limit states SLO, SLD and SLV. In Fig. 6.12 the mean of shear, displacement and drift peaks associated with each of the four state limits are reported. It is possible to note as the configurations with small amplitudes required ($D_{lim} = 0.7, 0.8 D_{max,m}$) exhibit an improvement of isolation performances, both in terms of base shear and displacement peaks, for the SLV and SLC, while an increase of base shear is observable for the SLO and SLD. On the other hand, the configurations optimized for $D_{lim} = 0.9, 1.0, 1.1 D_{max,m}$ exhibit a stronger reduction of base shear for the limit states SLV and SLC without amplification of force for state limits SLO and SLD.

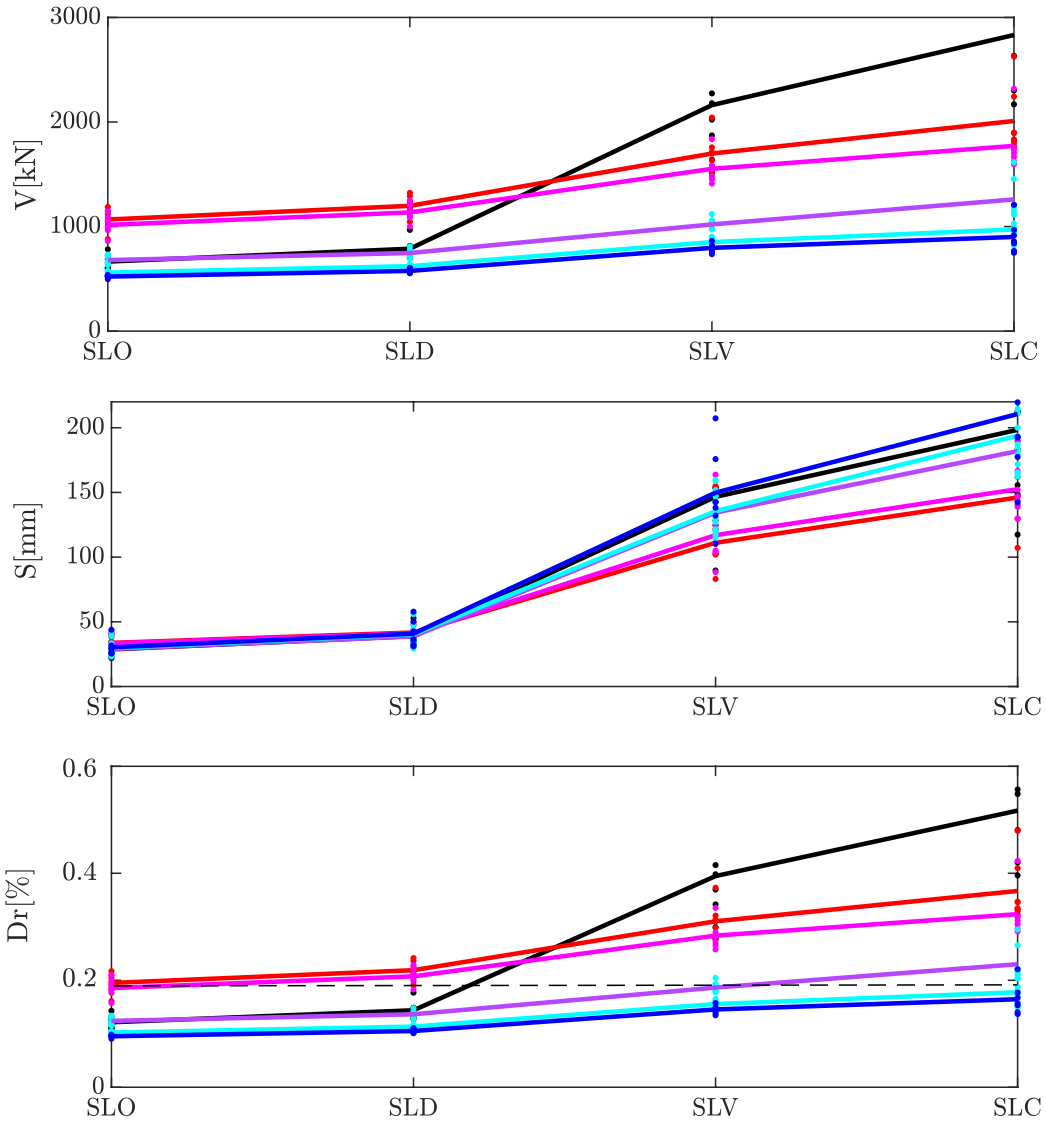

Figure 6.12: Mean of shear forces, displacement and drift peaks associated with each of the four state limits for the baseline isolation system (black lines) and for the NS-SMA configurations $D_{lim} = 0.7, 0.8, 0.9, 1.0, 1.1 D_{max,m}$ in red, magenta, violet, ciano and blue lines, respectively. The horizontal dashed line indicates the start damage drift $Dr = 0.2\%$.

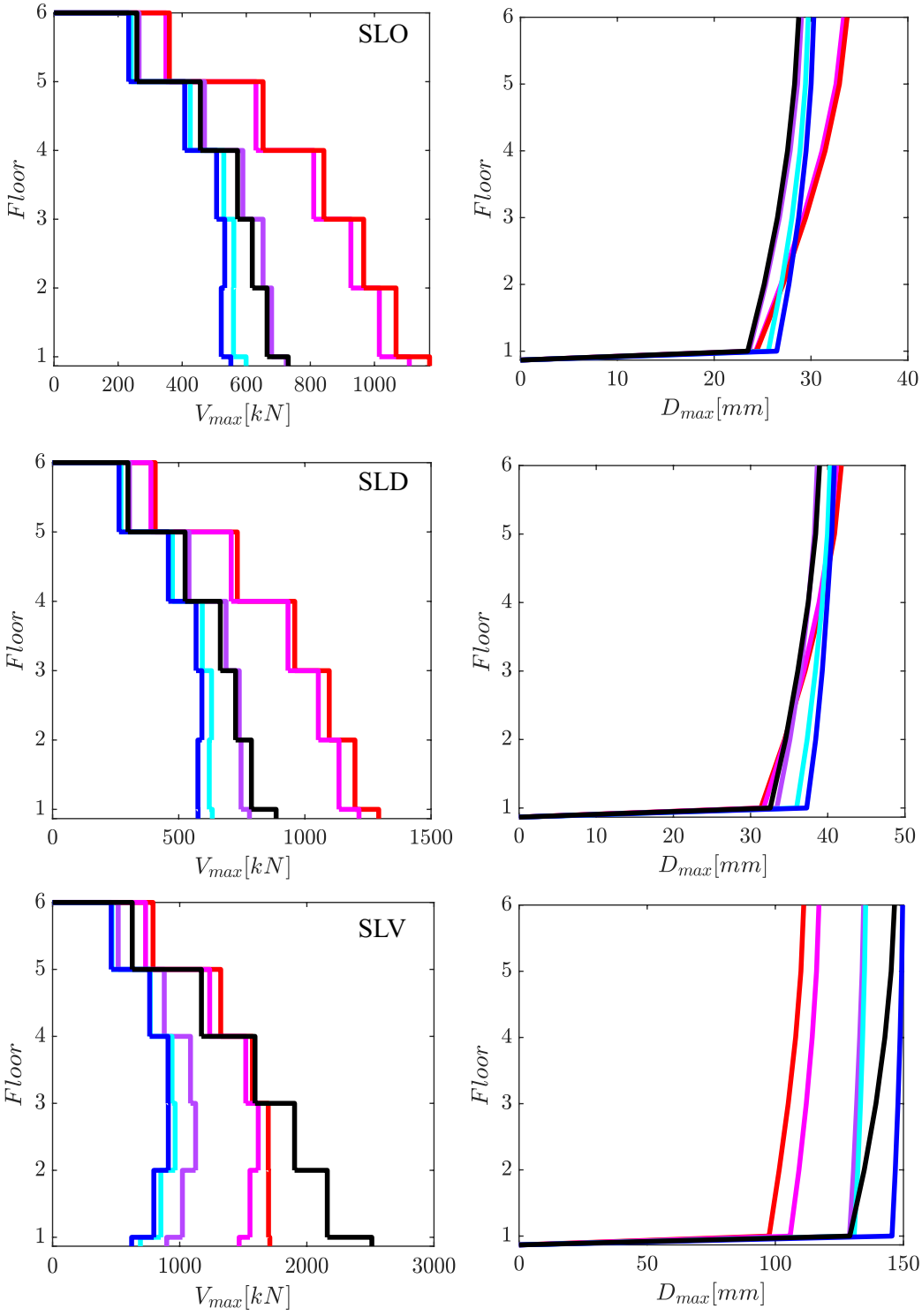

Figure 6.13: Mean of storey shear forces peaks (left) and of storey displacement peaks (right) associated with SLO, SLD and SLV limit states for the baseline isolation system (black lines) and for the NS-SMA configurations $D_{lim} = 0.7, 0.8, 0.9, 1.0, 1.1 D_{max,m}$ in red, magenta, violet, ciano and blue linse, respectively.

6.4 Comparison with other damping techniques

In order to prove the advantages of employing NS-SMA damping (S3) over other types of damping classically used in parallel with the baseline isolation system (S1), the following section reports the results of the optimizations of different auxiliary damping sources. In addition to the SMA damped system (S2), the following damping techniques are investigated:

- Non-linear viscous damping (VD): it has been modelled by adding the following term to the restoring force of the baseline isolation system:

$$f_V = c_v|\dot{x}|^{\alpha} sign(\dot{x}). \tag{6.2}$$

- Hysteretic damping (HD): it has been modelled by adding a pure hysteretic term (f_H) to the restoring force of the baseline isolation system. The evolution of the force is governed by the sequent rule:

$$\dot{f}_H = k_h[1-(\gamma_h+\beta_h \text{sign}(f_H\dot{x})]|\frac{f_H}{fy_h}|\dot{x}, \tag{6.3}$$

  where k_h indicates the initial stiffness of hysteretic devices and fy_h their yielding force. The parameters γ_h and β_h are set equals to 0.1 and 0.9, respectively.

- Friction damping (FD): it has been modelled by adding a Coulomb friction term to the restoring force of the baseline isolation system:

$$f_F = fy_F sign(\dot{x}). \tag{6.4}$$

- hybrid damping (HBD): finally, a configuration including the three types of damping already described (SMA, VD, HD, FD) was considered and modelled by adding the following term to the restoring force of the baseline isolation system:

$$f_{HB} = f_s + f_V + f_H + f_F. \tag{6.5}$$

For the configurations with Friction damping and with Hybrid damping, the four central bearings are assumed to be planar sliding device and, in order to take into account the presence of 12 elastomeric isolators instead 16, the stiffness of elastomeric isolation is reduced from $K_i = 84$ to $K_i = 63kN/mm$. The design parameters of the illustrated damping devices are optimized using D.E. algorithm and by minimizing the mean value of the base shear peaks exhibited by the isolated building forced by the SLC accelerograms.
In Tab.6.3 the value of optimized parameters and the associated performances are

	Optimized parameters	$V_{max,m}[kN]$	$D_{max,m}[mm]$	$\Delta V_{max,m}$ [%]	$\Delta D_{max,m}$ [%]
Baseline system (S1)		2829	200	~	~
(S3) $D_{lim} = 220\ mm$		900	210	-68%	5%
SMA	$k_s = 12\ kN/mm$	2740	165	-3%	-18%
VD	$c_v = 10.8\ kN(s/mm)^{\alpha}$, $\alpha_v = 0.73$	1975	106	-30%	-47%
HD	$k_h = 45\ kN/mm$, $fy_h = 468\ kN$	2316	121	-18%	-40%
FD	$f_f = 402\ kN$	1885	132	-33%	-34%
HBD	$k_s = 0$, $c_v = 6.2$, $\alpha_v = 1$ $k_h = 13$, $fy_h = 166$, $f_f = 424$	1829	110	-35%	-45%

Table 6.3: Value of optimized parameters and associated performances for damping techniques SMAD, VD, HD, FD, HBD.

reported for each described configurations and in Fig. 6.14 the mean of shear, displacement and drift peaks associated with each of the four state limits are reported for the different damping methods investigated. It can be seen that all classical damping techniques produce a substantial reduction in displacements but are not able to effectively reduce shear forces. This is because in all classical sources of damping the dissipating mechanism always introduces a stiffening contribution. Even the hybrid configuration, in which large amounts of hysteretic, viscous and frictional damping are present, with obvious economic implications, cannot reduce shear as much as NS-SMA damping.Moreover, unlike the latter, for both SLV and SLC limit states the optimal hybrid configuration exhibits a maximum drift larger than 0.2%, hence structural and non-structural elements experience damages. Therefore, given a maximum displacement limit, NS-SMA results to be the damping technique most able to reduce the forces and accelerations affecting the structure, and at the same time ensure a self-recentring capacity.

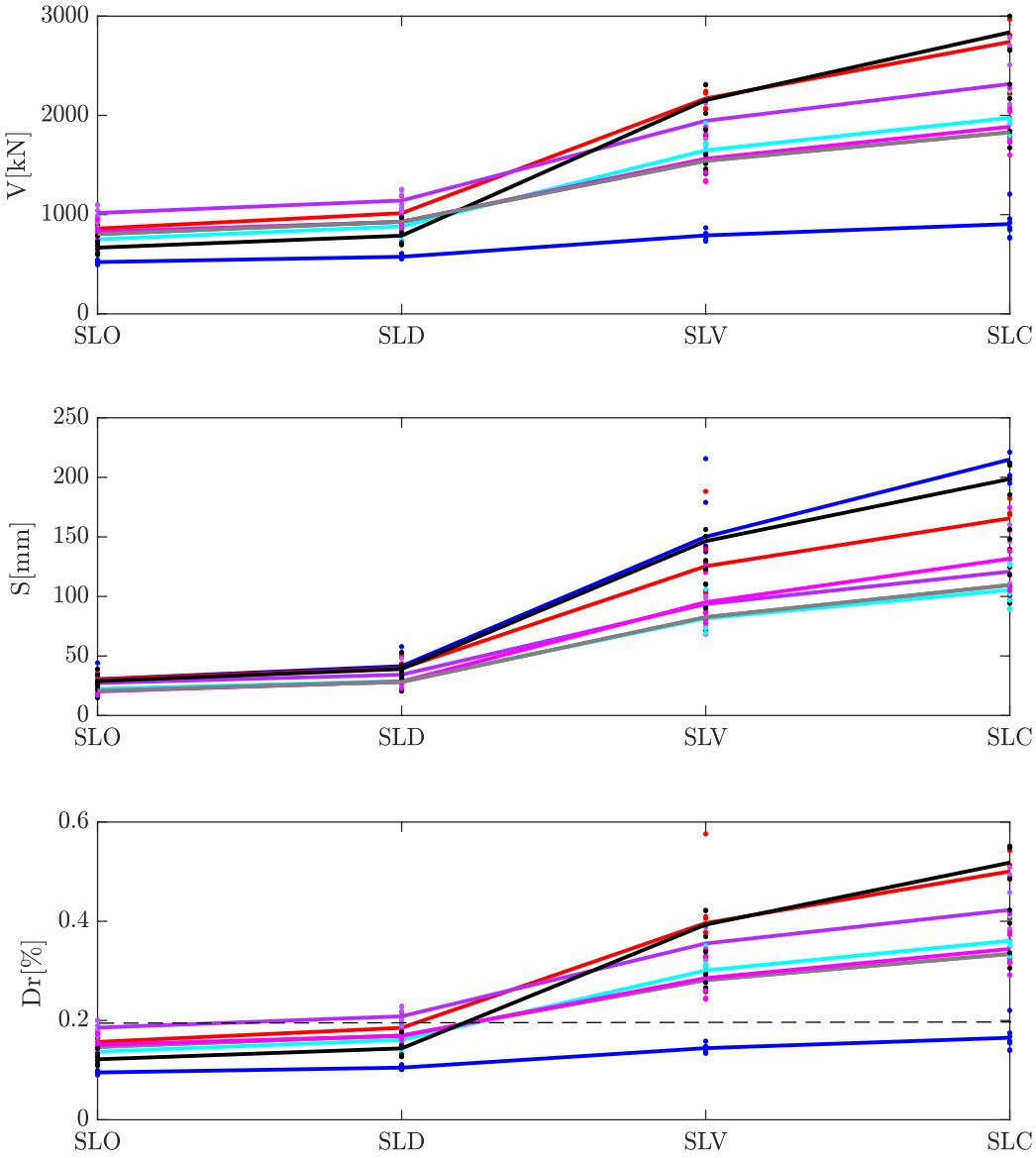

Figure 6.14: Mean of shear forces, displacement and drift peaks associated with each of the four state limits for the baseline isolation system (black lines), for the NS-SMA configurations $D_{lim} = 1.1D_{max,m}$ in blue lines and for the optimized SMAD, VD, HD, FD, HBD configurations in red, ciano, violet, magenta and gray lines, respectively. The horizontal dashed line indicates the start damage drift $Dr = 0.2\%$.

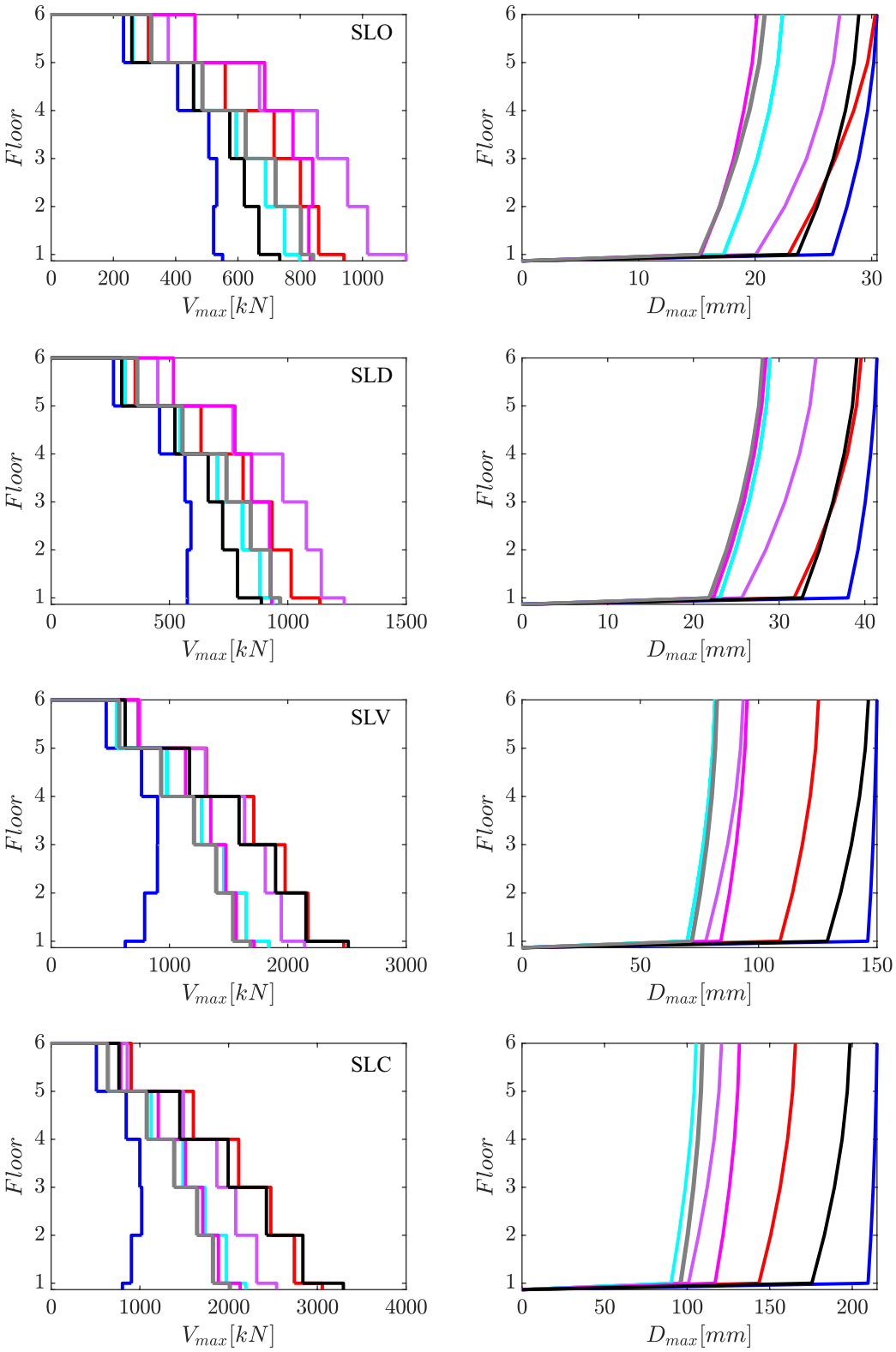

Figure 6.15: Mean of storey shear forces peaks (left) and of storey displacement peaks (right) associated with SLO, SLD, SLV and SLC limit states for the baseline isolation system (black lines), for the NS-SMA configurations $D_{lim} = 1.1D_{max,m}$ in blue lines and for the optimized SMAD, VD, HD, FD, HBD configurations in red, ciano, violet, magenta and gray lines, respectively.

6.5 Conclusions

The study of the dynamic response of a MDOF system, representative of a seismic isolated building, under seismic forcing showed the improvements in isolation performances achievable with the introduction of NS-SMA damping and its strong flexibility. In fact, by tuning the design parameters, it is possible to achieve a strong reduction in shear forces (70%) with the same maximum displacements of the baseline system, or a significant reduction in shear forces (30%) together with a reduction in displacements (30%).The optimization of response validate the optimum regions identified in previous chapters and provides useful design hints. The optimized NS-SMA configurations are able to prevents the start of structural damaging retaining the maximum drift values under the limit threshold $Dr = 0.2\%$ for all the limit states investigated (SLO, SLD, SLV, and SLC). This feature results to be not achievable from classic damping techniques studied (SMAD, HD, VD, FRD, HBD) despite the introduction of large amounts of damping devices and the consequent increase in costs. The illustrated performances, together with the self-recentering capacity of the proposed isolation system, effectively eliminate any potential economic losses induced by seismic risk, thereby confirming the possibility of obtaining a new generation of ideal high-performance seismic isolation systems.

Chapter 7

Design of a novel NS-SMA damper

Regarding negative stiffness mechanisms exploiting initial precompression, the initial deformation of the prestressed organ is of key importance for the functioning of the mechanism in terms of developable negative force and of displacement range with negative stiffness. These types of mechanisms are usually realized with prestressed springs which, in order to develop negative force levels that can effectively control the structure, assume relevant dimensions. Moreover, the systems proposed in the literature exhibit monodirectional behaviour. In the light of the above, a novel type of negative stiffness device showing:

- Higher control force in smaller size;
- Multidirectional response;
- Superelastic hysteresis;
- Versatility of functioning;

is designed and studied. The force-displacement law of the proposed device was first determined analytically and then numerically validated.

7.1 Description of mechanism

Figure 7.1 shows a three-dimensional view of the prototype and a schematic section to support the description. The device consists of two steel caps, one upper and one lower, (1,2) which are predisposed respectively for the connection of the device to the structure and to the ground. The connection to the structure consists of a male (device)-female (structure) connection by means of vertical bars (3) which can slide inside Teflon bushings in order to allow a mutual exchange of forces only in the horizontal plane. The two caps are connected together by means

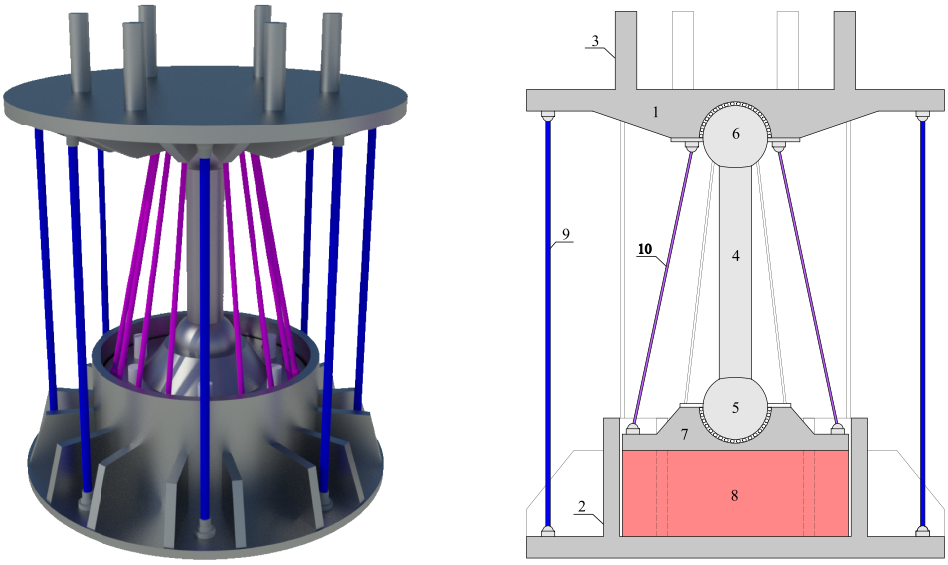

Figure 7.1: Tridimensional and section view of the designed device.

of a vertical rod (4) with low-friction spherical hinges (5,6) arranged in series with a polyurethane spring (8). The assembly described is pre-compressed by means of a group of pre-stressed ropes arranged externally (9) in fibre-reinforced polymers (with glass or carbon fibres). Finally, the upper head of the vertical rod is joined to the connecting plate (7) with the polyurethane spring by a group of inclined steel or memory alloy wires (10). The initial pre-compression of the device by pre-tensioning of the external ropes (9) causes instability of the vertical rod (4) in its initial equilibrium position and thus the presence of a negative stiffness response branch. In fact, the device, if loaded in any direction in the horizontal plane, will exert, for a given tunable displacement range, a force in the same direction of the displacement (i.e. negative stiffness). In the presence of a relative displacement between the two ends of the device in the horizontal plane, the connecting vertical rod rigidly rotates around the lower hinge, sweeping, due to its shorter length, a greater angle with respect to the pretensioned ropes. This difference in the angle described by the ropes and the connecting rod causes that the horizontal component of the contrast force exerted by the rod on the upper cap is higher than the horizontal component of the traction force exerted by the ropes, thus producing a resultant in the direction of displacement. When the relative displacement between the ends of the device increases, the tension of the ropes and therefore the level of pre-compression of the rod decreases until a limit displacement is reached, after which the device is decompressed. This progressive decompression produces

a cubic stiffness term in the rheological response of the device. The polyurethane spring (8) at the base of the rod is also pre-compressed and, during the rigid motion of the rod, it expands, thus causing an upward translation of the lower hinge of the rod. This translation results in a greater angle swept by the rod hence produces an amplification of the negative stiffness and a delay in the decompression of the device, i.e., greater ultimate displacements. The introduction of the group of oblique wires (10) allows to restore stability in the initial equilibrium position delaying the negative stiffness and, at the same time, allows to introduce high levels of hysteretic damping without loss of performance due to the increase of initial stiffness, since this increase is cancelled by the negative stiffness properly calibrated. In fact, assuming an elastic stiffness of the wires equal to the negative stiffness, for levels of displacement lower than the displacement corresponding to the yielding (steel wires) or to the phase transformation (shape memory alloy wires) of the wires (9), a null force will be exerted by the device and then the total restoring force of the system will coincide with that of the structure. On the other hand, for larger displacements, the negative stiffness is not balanced anymore by the horizontal stiffness of the wires, and a reduction of the total force and of the global stiffness (accelerations) is obtained. For large displacements, approaching the maximum allowed displacement, the cubic stiffness term produced by the geometric non-linearities cancels the negative one, and the total response coincides again with the one of the controlled structure.

7.1.1 Novelty of the proposed damper

Le principali caratteristiche innovative sono tre:

- A COMPACTNESS OF THE DEVICE: the negative stiffness dampers present in the literature are bistable mechanisms where the prestressing is provided by prestressed deformable elements inserted in the contrasting frame. These elements, which are subject to compression and therefore to possible local instability phenomena, are usually realised with steel helical springs and their dimensions are relevant compared with the control force exerted. With the proposed device, on the other hand, it is possible to obtain high control forces with small damper sizes by exploiting two aspects:
  - The pre-compression is achieved through the pre-tensioning of the external ropes and the compressed elements, i.e. the rigid rod and the polyurethane spring, are not susceptible to buckling phenomena due to the shape of the elements and the nature of the applied restraints.
  - The use of high performance materials such as Fiber Reinforced Polymer (FRP) for the prestressed ropes and polyurethane for the expansion spring allows to achieve high levels of initial pretension.

The compactness of the damper is of crucial importance in terms of design and installation simplicity in existing and new structures.

- B MULTIDIRECTIONALITY OF THE RESPONSE: Most of the negative stiffness dampers found in the literature are plane mechanisms able to exert the control force only in a specific direction. In most vibration control applications the load direction can be any direction in the horizontal plane, so a "cylindrical" type of damper response is required.
- C VERSATILITY OF THE RESPONSE: By designing the pretension and the number of the external ropes, the relative dimensions between the connecting rod and the ropes, and the layout and the material of the damper ropes, it is possible to obtain different rheological behaviours according to the application field of the damper.

7.2 Analytic force displacement law

By imposing the force equilibrium in the device deformed configuration (see Fig. 7.2), the analytical equations governing the force-displacement response as a function of the geometrical and mechanical parameters of the different parts constituting the damper are obtained.

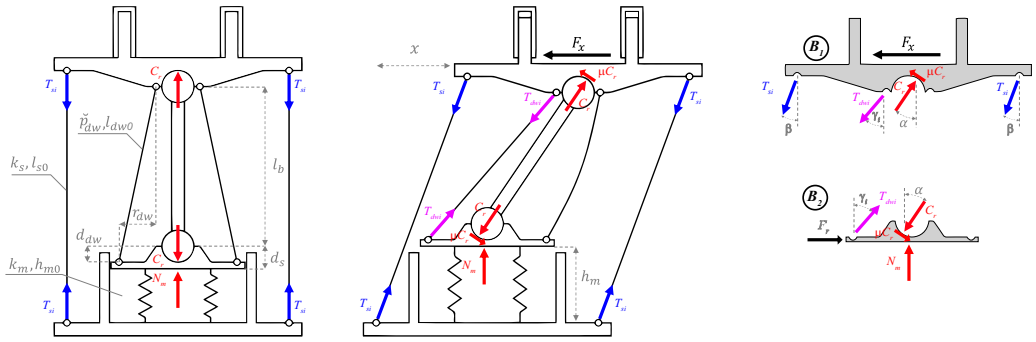

Figure 7.2: Scheme of mechanism and forces in the undeformed (left) and in the deformed configurations (center) and free body diagram of the superior head (1) and of the plate (7)(right).

In particular, the equilibrium equations for the translation along the x and y directions, a generic direction belonging to the horizontal plane and the vertical direction respectively, of the superior head (1) and of the plate (7) between the rod

and the poliurethanic spring are wrote:

$$\sum_j F_{\mathrm{xB1}} : C\mathrm{Sin}(\alpha) - \mu C\mathrm{Cos}(\alpha) - T_s\mathrm{Sin}(\beta) - Tx_{dw} = F_x; \tag{7.1}$$

$$\sum_j F_{\mathrm{yB1}} : C\mathrm{Cos}(\alpha) + \mu C\mathrm{Sin}(\alpha) - Ty_{dw} - T_s\mathrm{Cos}(\beta) = 0; \tag{7.2}$$

$$\sum_j F_{\mathrm{xB2}} : Tx_{dw} - C\mathrm{Sin}(\alpha) + \mu C\mathrm{Cos}(\alpha) = F_r; \tag{7.3}$$

$$\sum_j F_{\mathrm{yB2}} : N_m + Ty_{dw} - C\mathrm{Cos}(\alpha) - \mu C\mathrm{Sin}(\alpha) = 0; \tag{7.4}$$

where C is the compression force of the rigid rod, T_s is the traction force of the external strands, Tx_{dw} and Ty_{dw} denotes respectively the horizontal and vertical component of the damper wires forces, N_m is the compression force of the spring and μ represents the friction coefficient of the sliding surfaces of the rod spherical hinges. The angles α and β are the angles between the vertical direction and the rod or the external strands respectively. Substituting the eq. 7.4 in the equations relative to B1, the subsequent equations are obtained:

$$\sum_j F_{\mathrm{xB1}} : N_m \left(\frac{\mathrm{Sin}(\alpha) - \mu\mathrm{Cos}(\alpha)}{\mathrm{Cos}(\alpha) + \mu\mathrm{Sin}(\alpha)} \right) - T_s\mathrm{Sin}(\beta) - Fx_{dw} = F_x; \tag{7.5}$$

$$\sum_j F_{\mathrm{yB1}} : N_m - T_s\mathrm{Cos}(\beta) = 0. \tag{7.6}$$

The forces of the poliurethanic spring and of the external strands are described by:

$$N_m = k_m(h_m - h_{m0}); \tag{7.7}$$

$$T_s = k_s(l_s - l_{s0}); \tag{7.8}$$

where k_m and k_s denote respectively the spring and the strands stiffness, h_m and l_s the deformed lengths of the spring and the strands respectively and, finally, h_{m0} and l_{s0} are the undeformed length of the spring and of the strands. The deformed length of the strands l_s, the sine and cosine of the angle β read:

$$l_s = \sqrt{(d_s + h_m + l_b\mathrm{Cos}(\alpha))^2 + (l_b\mathrm{Sin}(\alpha))^2}; \tag{7.9}$$

$$\mathrm{Sin}(\beta) = \frac{l_b\mathrm{Sin}(\alpha)}{l_s}; \tag{7.10}$$

$$\mathrm{Cos}(\beta) = \frac{d_s + h_m + l_b\mathrm{Cos}(\alpha)}{l_s}; \tag{7.11}$$

where d_s is the vertical distance between the center of the lower spherical hinge and the upper face of the spring and l_b is the rod lenght. In the undeformed

configuration of the device ($\alpha = u = 0$) the equilibrium equation 7.6, the length of the strands and of the spring read:

$$\sum_j F_{\mathrm{yB1}} : N_m = T_s = N_0; \tag{7.12}$$

$$l_s(\alpha = u = 0) = l_{s1} = d_s + h_{m1} + l_b; \tag{7.13}$$

$$h_m(\alpha = u = 0) = h_{m1} = \frac{k_s(d_s + l_b - l_{s0}) + k_m h_{m0}}{k_m - k_s}; \tag{7.14}$$

where N_0 is the pretension force of the device. Can be useful in order to understand the role of pretension level to express the lengths l_{s1} and h_{m1} in function of the initial pretension force N_0 as:

$$k_m\,(h_{m1} - h_{\mathrm{m0}}) = k_s\,(l_{s1} - l_{\mathrm{s0}}) = N_0; \tag{7.15}$$

$$l_{s1} = \frac{N_0 + k_s l_{s0}}{k_s}; \tag{7.16}$$

$$h_{m1} = \frac{N_0 + k_m h_{m0}}{k_m}. \tag{7.17}$$

The overall force exerted in the horizontal plane by the group of damper wires Fx_{dw} is:

$$Fx_{dw} = Tx_{dw} - Ty_{dw}\left(\frac{\mathrm{Sin}(\alpha) - \mu\mathrm{Cos}(\alpha)}{\mathrm{Cos}(\alpha) + \mu\mathrm{Sin}(\alpha)}\right) \tag{7.18}$$

where Tx_{dw} and Ty_{dw} are the sum of horizontal and vertical components of each damper wires forces, and are given by:

$$Tx_{dw} = \sum_1^{n_{\mathrm{dw}}} T_{dwi}\mathrm{Sin}\,(\gamma_i)\,\mathrm{Cos}\,(\delta_i)\,; \tag{7.19}$$

$$Ty_{dw} = \sum_1^{n_{\mathrm{dw}}} T_{dwi}\mathrm{Cos}\,(\gamma_i)\,. \tag{7.20}$$

The force of each damper wires T_{dwi} is given by ad hoc hysteretic model in function of the wires elongation and its ratio:

$$T_{dwi} = \sigma_i\,(\varepsilon_i, \dot{\varepsilon}_i) A_{\mathrm{dw}}; \tag{7.21}$$

$$\varepsilon_i = \frac{l_{\mathrm{dwi}} - l_{\mathrm{dw0}}}{l_{\mathrm{dw0}}}; \tag{7.22}$$

$$l_{\mathrm{dwi}} = \sqrt{(r\mathrm{Sin}\,(\delta_{0i}))^{\,2} + (r\mathrm{Cos}\,(\delta_{0i}) + l_b\mathrm{Cos}(\alpha))^{\,2} + (d_{\mathrm{dw}} + l_b\mathrm{Cos}(\alpha))^{\,2}}; \tag{7.23}$$

where r is the length of the horizontal projection of the damper wires and d_{dw} is the vertical distance between the lower node of the damper wires and the upper face of the spring. The initial angle δ_{0i} and the angle δ_i in the deformed configuration between each wire and the motion direction in the horizontal plane read:

$$\delta_{0i} = \frac{\pi(i-1)}{2\,(n_{\rm dw})-1}; \tag{7.24}$$

$$\mathrm{Cos}\,(\delta_i) = \frac{r\mathrm{Cos}\,(\delta_{0i}) + l_b\mathrm{Cos}(\alpha)}{\sqrt{(r\mathrm{Sin}\,(\delta_{0i}))^2 + (r\mathrm{Cos}\,(\delta_{0i}) + l_b\mathrm{Cos}(\alpha))^2}}; \tag{7.25}$$

while the seno and coseno of the angle γ_i of each wire respect the vertical direction in the vertical plane belonging to the direction of the motion are given by:

$$\mathrm{Sin}\,(\gamma_i) = \frac{\sqrt{(r\mathrm{Sin}\,(\delta_{0i}))^2 + (r\mathrm{Cos}\,(\delta_{0i}) + l_b\mathrm{Cos}(\alpha))^2}}{l_{\rm dwi}}; \tag{7.26}$$

$$\mathrm{Cos}\,(\gamma_i) = \frac{\sqrt{d_{\rm dw} + l_b\mathrm{Cos}(\alpha)}}{l_{\rm dwi}}. \tag{7.27}$$

Substituting all the described contributes in the equilibrium equation of the body 1 gives:

$$\sum_j F_{\rm xB1} : F_x = k_m\,(h_m - h_{\rm m0})\left(\frac{\mathrm{Sin}(\alpha) - \mu\mathrm{Cos}(\alpha)}{\mathrm{Cos}(\alpha) + \mu\mathrm{Sin}(\alpha)}\right) + \tag{7.28}$$
$$- k_s\frac{l_b\mathrm{Sin}(\alpha)\left(\sqrt{(d_s + h_m + l_b\mathrm{Cos}(\alpha))^2 + (l_b\mathrm{Sin}(\alpha))^2} - l_{\rm s0}\right)}{\sqrt{(d_s + h_m + l_b\mathrm{Cos}(\alpha))^2 + (l_b\mathrm{Sin}(\alpha))^2}} - \mathrm{Fx}_{\rm dw};$$

$$\mathrm{Fx}_{\rm dw} = \sum_1^{n_{\rm dw}} \sigma_i\,(\varepsilon_i, \dot{\varepsilon}_i) A_{\rm dw} \tag{7.29}$$
$$\frac{r\mathrm{Cos}\,(\delta_{0i}) + l_b\mathrm{Cos}(\alpha) - \sqrt{d_{\rm dw} + l_b\mathrm{Cos}(\alpha)}\left(\frac{\mathrm{Sin}(\alpha) - \mu\mathrm{Cos}(\alpha)}{\mathrm{Cos}(\alpha) + \mu\mathrm{Sin}(\alpha)}\right)}{\sqrt{(r\mathrm{Sin}\,(\delta_{0i}))^2 + (r\mathrm{Cos}\,(\delta_{0i}) + l_b\mathrm{Cos}(\alpha))^2 + (d_{\rm dw} + l_b\mathrm{Cos}(\alpha))^2}};$$

$$\sum_j F_{\rm yB1} : k_m\,(h_m - h_{\rm m0}) + \tag{7.30}$$
$$- k_s\frac{\left(\sqrt{(d_s + h_m + l_b\mathrm{Cos}(\alpha))^2 + (l_b\mathrm{Sin}(\alpha))^2} - l_{\rm s0}\right)(d_s + h_m + l_b\mathrm{Cos}(\alpha))}{\sqrt{(d_s + h_m + l_b\mathrm{Cos}(\alpha))^2 + (l_b\mathrm{Sin}(\alpha))^2}} = 0.$$

The first equation is the constitutive law of the device force in function of all the geometric and mechanical device parameters, of the independent variable α and of the length of spring h_m. This can be obtained as the positive solution of the fourth

order polynomial given by the equilibrium equation in the vertical direction. The coefficients of the polynomial are:

$$a_p = -\left(k_m + k_s\right)^2; \tag{7.31}$$

$$b_p = -2\left(k_m + k_s\right)\left(l_b \mathrm{Cos}(\alpha)\left(k_m + 2k_s\right) + d_s\left(k_m + 2k_s\right) - h_{\mathrm{m0}} k_m\right); \tag{7.32}$$

$$\begin{aligned} c_p = {} & -2l_b \mathrm{Cos}(\alpha)\left(d_s\left(6k_m k_s + k_m^2 + 6k_s^2\right) - h_{\mathrm{m0}} k_m\left(2k_m + 3k_s\right)\right) + \\ & - k_m^2\left(l_b^2 + h_{\mathrm{m0}}^2\right) - \frac{1}{2} l_b^2 \mathrm{Cos}(2\alpha) k_s\left(4k_m + 5k_s\right) 4 l_b^2 k_m k_s - \frac{7}{2} l_b^2 k_s^2 + \\ & + 2d_s h_{\mathrm{m0}} k_m\left(2k_m + 3k_s\right) - d_s^2\left(6k_m k_s + k_m^2 + 6k_s^2\right) + k_s^2 l_{\mathrm{s0}}^2; \end{aligned} \tag{7.33}$$

$$\begin{aligned} d_p = {} & \frac{1}{2}\left(l_b^2 k_s\left(-l_b \mathrm{Cos}(3\alpha) k_s - 2\mathrm{Cos}(2\alpha)\left(2d_s k_m + 5d_s k_s - 2h_{\mathrm{m0}} k_m\right)\right)\right. \\ & - l_b \mathrm{Cos}(\alpha)\left(4l_b^2 k_m k_s + k_s^2\left(7l_b^2 - 4l_{\mathrm{s0}}^2\right) - 8d_s h_{\mathrm{m0}} k_m\left(k_m + 3k_s\right) + 12 d_s^2 k_s\left(k_m + 2k_s\right) + \right. \\ & \left. 4h_{\mathrm{m0}}^2 k_m^2\right) - 2d_s\left(4l_b^2 k_m k_s + k_s^2\left(7l_b^2 - 2l_{\mathrm{s0}}^2\right) + 2h_{\mathrm{m0}}^2 k_m^2\right) + 4l_b^2 h_{\mathrm{m0}} k_m\left(k_m + 2k_s\right) + \\ & \left. + 4d_s^2 h_{\mathrm{m0}} k_m\left(k_m + 3k_s\right) - 4d_s^3 k_s\left(k_m + 2k_s\right)\right); \end{aligned} \tag{7.34}$$

$$\begin{aligned} e_p = {} & \frac{1}{2}\left(l_b^2 k_s\left(\mathrm{Cos}(2\alpha)\left(-l_b^2 k_s + 4d_s h_{\mathrm{m0}} k_m - 5d_s^2 k_s + k_s l_{\mathrm{s0}}^2\right) + \right.\right. \\ & \left. - l_b \mathrm{Cos}(3\alpha) d_s k_s\right) + l_b \mathrm{Cos}(\alpha)\left(d_s k_s^2\left(4l_{\mathrm{s0}}^2 - 7l_b^2\right) + 4l_b^2 h_{\mathrm{m0}} k_m k_s + 12 d_s^2 h_{\mathrm{m0}} k_m k_s + \right. \\ & \left. - 4d_s h_{\mathrm{m0}}^2 k_m^2 - 8d_s^3 k_s^2\right) + d_s^2\left(k_s^2\left(2l_{\mathrm{s0}}^2 - 7l_b^2\right) - 2h_{\mathrm{m0}}^2 k_m^2\right) + 8 l_b^2 d_s h_{\mathrm{m0}} k_m k_s + \\ & \left. + l_b^2\left(k_s^2\left(l_{\mathrm{s0}}^2 - l_b^2\right) - 2h_{\mathrm{m0}}^2 k_m^2\right) + 4d_s^3 h_{\mathrm{m0}} k_m k_s - 2d_s^4 k_s^2\right). \end{aligned} \tag{7.35}$$

The force of damper wires and the length of spring h_m are independent from each other.

7.2.1 Elastic force displacement law

Focusing on the force expressed by the device without damper wires and assuming the friction coefficient null, the solution of the polynomial remains the same and the force identified is the elastic backbone (F_{xel}) of the device hysteretic response. This can be expressed as:

$$\begin{aligned} F_{xel} = {} & k_m\left(h_m - h_{\mathrm{m0}}\right)\mathrm{Tan}(\alpha) + \\ & - k_s \frac{l_b \mathrm{Sin}(\alpha)\left(\sqrt{\left(d_s + h_m + l_b \mathrm{Cos}(\alpha)\right)^2 + \left(l_b \mathrm{Sin}(\alpha)\right)^2} - l_{\mathrm{s0}}\right)}{\sqrt{\left(d_s + h_m + l_b \mathrm{Cos}(\alpha)\right)^2 + \left(l_b \mathrm{Sin}(\alpha)\right)^2}}; \end{aligned} \tag{7.36}$$

whereas the horizontal displacement can be expressed in function of the angle α as $u = Sin(\alpha)/l_b$. In Fig. 7.3 the horizontal elastic force of the device vs the

horizontal displacement is represented together with the evolution of the traction of the external strand and of the compression of the spring for a given set of geometric and mechanical parameters.

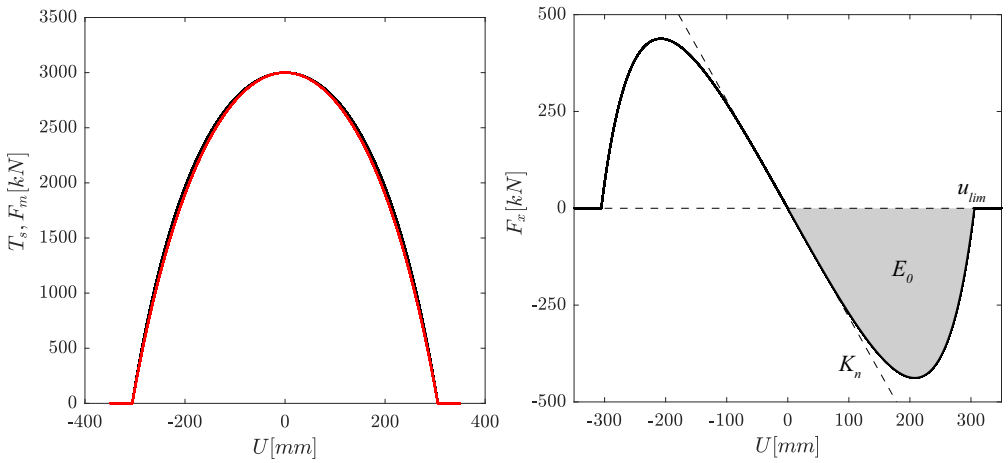

Figure 7.3: (left) Evolution of force in external strands and spring, in black and red lines respectively, and (right) total force in horizontal plane (F_x).

As can be observed, the efficiency and global performances of the device response can be expressed by three macro quantity: the initial negative stiffness (K_n), the displacement corresponding to the decompression of the device hence to a null force (u_{lim}) and the area enclosed by the negative branch of the response, coinciding with the mechanical energy released by the device and subtracted from the motion (E_0). This three quantities descriptive of the response and useful from a design point of view are obtained in a compact way. The first, the initial negative stiffness (K_n), can be obtained simplifying the law of the elastic response (eq. 7.36) with the assumption of small angle (α, β and γ). With this assumption the subsequent are obtained $l_s = l_{s1}$, $h_m = h_{m1}$ and the elastic force-displacement law becomes:

$$F'_{xel} = k_m\,(h_{m1} - h_{\mathrm{m0}})\,\mathrm{Tan}(\alpha) - k_s\frac{(l_{s1} - l_{s0})}{l_{s1}}l_b\mathrm{Sin}(\alpha); \tag{7.37}$$

$$F'_{xel} = N_0\frac{(l_{s1} - l_b)}{l_b l_{s1}}u; \tag{7.38}$$

$$K_n = N_0\frac{(l_{s1} - l_b)}{l_b l_{s1}}. \tag{7.39}$$

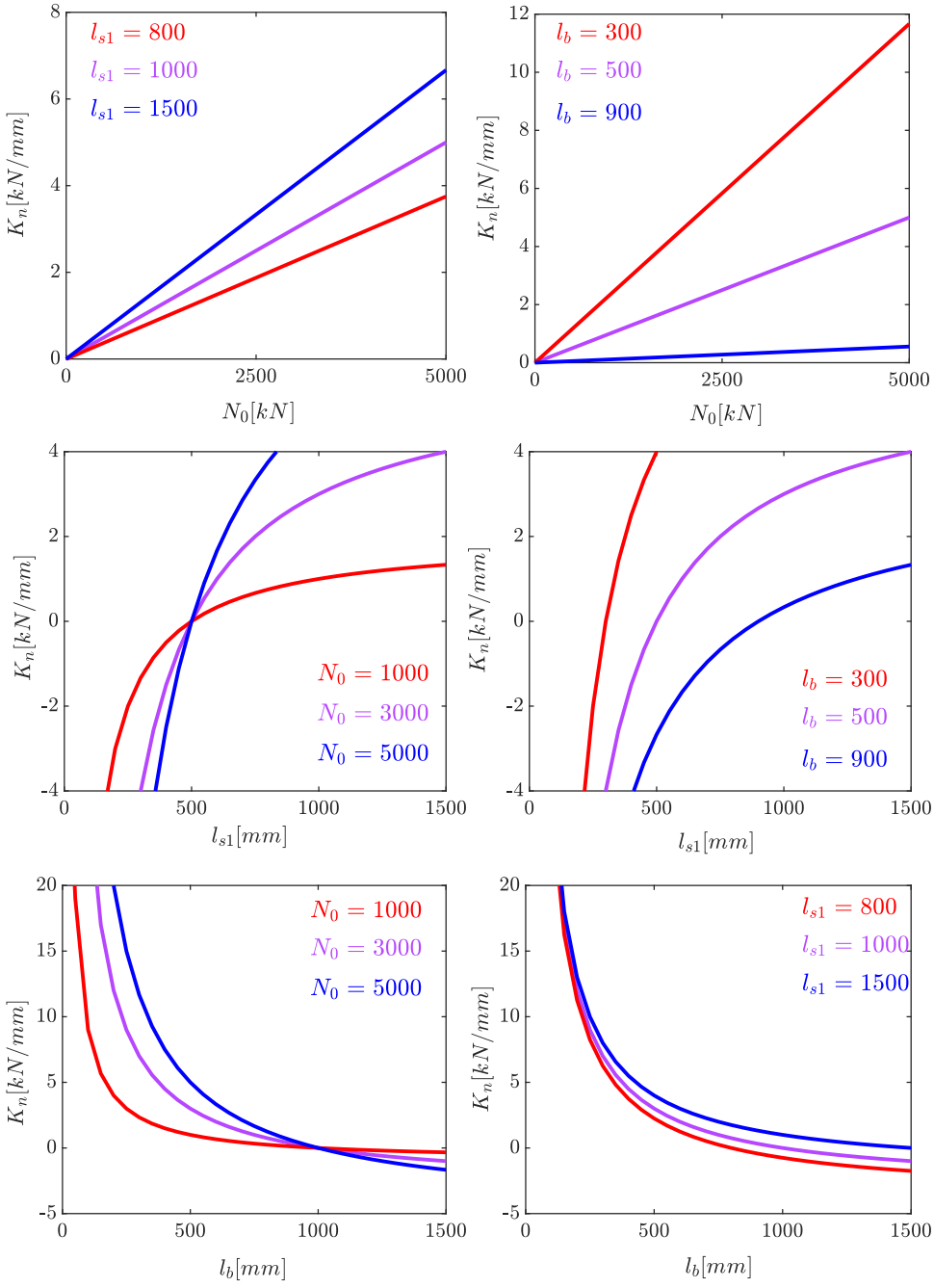

Figure 7.4: Initial negative stiffness by device (K_n) vs the pretension force (N_0) (top), vs the strands stiffness (k_s) (center) and vs the spring stiffness (k_m).

As revealed, the initial negative stiffness depends mainly from the pretension force (N_0) and from the difference in length between the strands and the rigid rod. Major is the lengths difference and major is the difference between the angles covered by the strands and the rod, the real source of the negative stiffness. Is interesting to note that the initial stiffness is independent from the mechanical and geometric properties of the polyurethane spring. Fig. 7.4 shows how the initial negative stiffness of the device (K_n) varies according to the pretension force (N_0), to the strands length (l_{s1}) and to the rod length (l_b). It can be observed a linear dependence between the negative stiffness K_n and the pretension force N_0, while for the strands and rod length it can be noted that to longer strands or shorter lever corresponds higher negative stiffness.
The displacement corresponding to the decompression of the device (u_{lim}) can be obtained writing the length of strands and considering that $l_s = l_{s0}$ and $h_m = h_{m0}$:

$$l_{s0} = \sqrt{(d_s + h_{m0} + l_b \mathrm{Cos}(\alpha))^2 + (l_b \mathrm{Sin}(\alpha))^2}; \tag{7.40}$$

$$u_{lim} = \sqrt{l_b^2 - \left(\frac{l_{s0}^2 - l_b^2 - (d_s + h_{m0})^2}{2(d_s + h_{m0})}\right)^2}. \tag{7.41}$$

The last parameter is the area enclosed by the negative branch of the response. This quantity coincide with the maximum mechanical energy released by the device (E_0) and can be obtained integrating the force-displacement law from $u = 0$ to $u = u_{lim}$. Another simpler way to obtain E_0 is to consider that the maximum mechanical energy deliverable by the device is is the energy stored through the initial pre-deformation of deformable parts. These are the strands and the spring, hence;

$$E_0 = \frac{1}{2} k_s (l_{s1} - l_{s0})^2 + \frac{1}{2} k_m (h_{m1} - h_{m0})^2; \tag{7.42}$$

$$E_0 = \frac{1}{2} N_0^2 \left(\frac{1}{k_s} + \frac{1}{k_m}\right). \tag{7.43}$$

From the two last obtained laws (u_{lim} and E_0) it can be observed that for the same pretension force N_0 the limit displacement and the total mechanical energy of device are higher when the parts are more deformable, hence the initial elongations $l_{s1} - l_{s0}$ and $h_{m1} - h_{m0}$ are higher. Fig. 7.5 shows how the mechanical energy released by the device (E_0) varies according to the pretension force (N_0), to the strands stiffness (k_s) and to the spring stiffness (k_m). It can be observed that to an higher pretension force corresponds an higher stored energy, hence an higher released energy. On the other hand, at equal pretension force, an higher strands or spring stiffness implies a lower pretension deformation, hence a lower stored energy. In Fig. 7.6 are reported the variations in the force-displacement response induced by a variation in N_0, k_s or k_m.

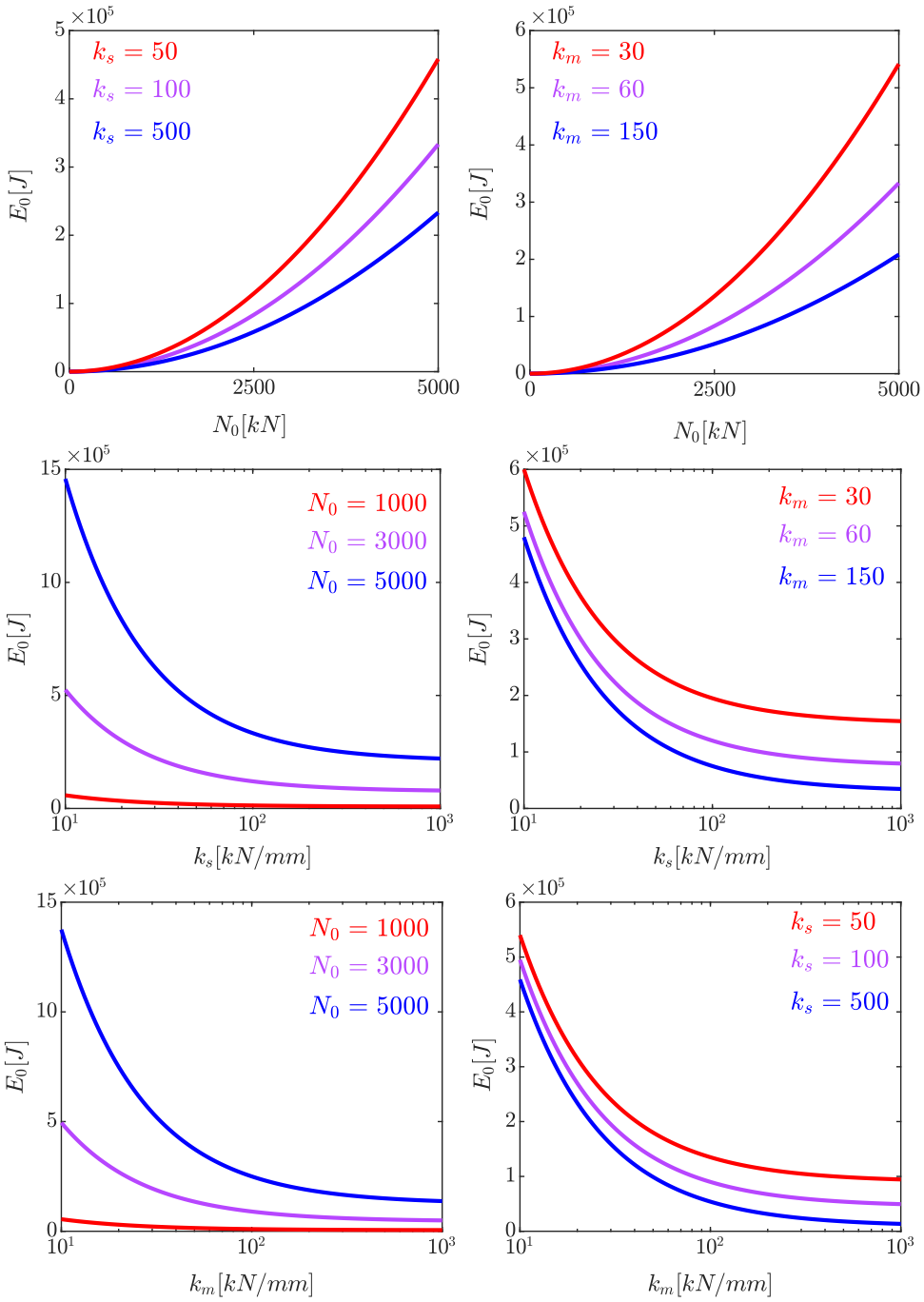

Figure 7.5: Total energy released by device (E_0) vs the pretension force (N_0) (top), vs the strands stiffness (k_s) (center) and vs the spring stiffness (k_m) (bottom).

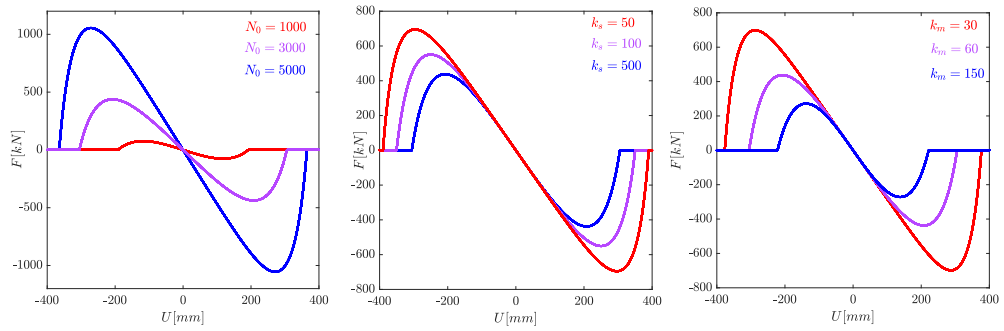

Figure 7.6: Elastic force displacement response of device for different pretension forces (N_0) (left), strands stiffnesses (k_s) (center) spring stiffnesses (k_m) (right).

This proves the importance of adopting resistant and deformable materials (such as fiber reinforced polymer) for the strands and the spring and of introducing more of one deformable part in order to obtain, for the same pretension force, a higher stored mechanical energy. An interesting limit case is the one where the spring is rigid, hence the only deformable parts are the strands. The force-displacement law reads:

$$F_{xel} = k_s(d_s + h_{m0})\left(\frac{\sqrt{(d_s + h_{m0} + l_b Cos(\alpha))^2 + (l_b Sin(\alpha))^2} - ls0}{\sqrt{(d_s + h_{m0} + l_b Cos(\alpha))^2 + (l_b Sin(\alpha))^2}}\right) Tan(\alpha). \quad (7.44)$$

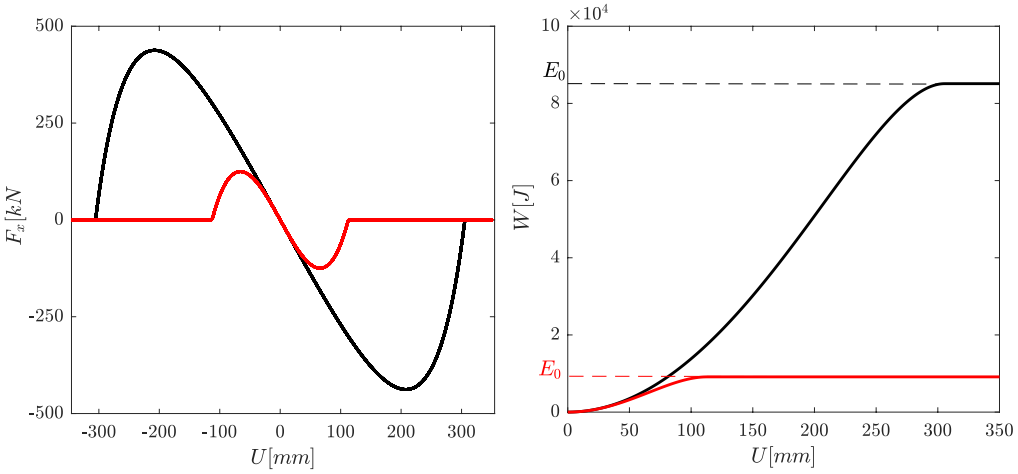

Figure 7.7: Force vs displacement response (left) and mechanical energy released vs displacement (right) for the device with and without the deformable spring in black and red lines respectively.

As can be seen in Fig. 7.7 the initial stiffness is the same of the device with the spring deformable, but the energy released and the limit displacement are strongly lower, due to the lower stored energy.

7.2.2 Hysteretic response

By considering the effect of friction on the sliding surfaces of spherical hinges at the rod joints, the force displacement law becomes:

$$F_x = k_m\,(h_m - h_{\mathrm{m0}})\left(\frac{\mathrm{Sin}(\alpha)-\mu\mathrm{Cos}(\alpha)}{\mathrm{Cos}(\alpha)+\mu\mathrm{Sin}(\alpha)}\right)+ \\ -k_s\frac{l_b\mathrm{Sin}(\alpha)\left(\sqrt{(d_s+h_m+l_b\mathrm{Cos}(\alpha))^2+(l_b\mathrm{Sin}(\alpha))^2}-l_{\mathrm{s0}}\right)}{\sqrt{(d_s+h_m+l_b\mathrm{Cos}(\alpha))^2+(l_b\mathrm{Sin}(\alpha))^2}}. \tag{7.45}$$

In Fig. 7.8 are shown the elastic backbone of response, the friction force on the horizontal plane and the hysteretic response of the device for differents friction ratios (μ). The choose of the sliding surfaces material is, as shown, of high importance for the overall response of device. If the objective is to obtain a recentering system, the friction must be kept to low values trough the insertion of lubricated surfaces or PTFE film. On the other hand, if the main goal is to dissipate incoming energy, the friction can be exploited.

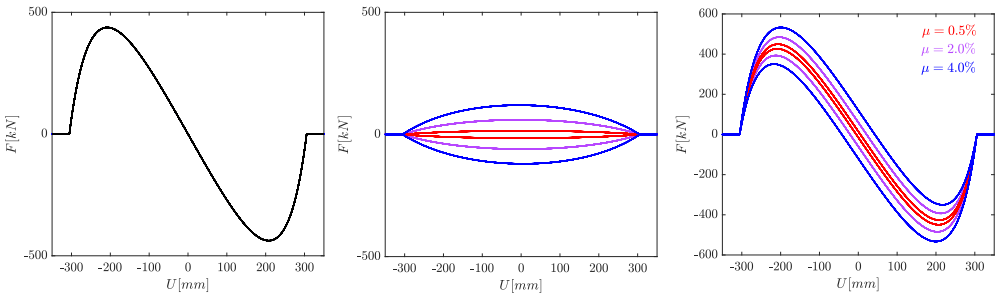

Figure 7.8: (left) Elastic backbone of response, (center) friction force on the horizontal plane and (right) hysteretic response of the device for $\mu = 0.5\%, 2\% and 4\%$ in red, violet and blue lines respectively.

Another source of hysteretic damping, as explained above, are the damper wires. These can be in steel or in NiTiNol alloy.The type of material of damper wires can be emulated choosing ad hoc constitutive law that describes the relation $\sigma = f(\varepsilon, \dot{\varepsilon})$ of wires. For the steel wires the Bouc-Wen model is used in order to describe the plastic response of the wires, while for the NiTiNol wires the above described Charalampakis model is used to represent the superelastic hysteresis of the wires. By using Eq.7.29 the force exerted by damper wires in the horizontal

plane can be computed and added to the force of device (Eq. 7.28). In Fig. 7.9 the overall response of device with damper wires of steel is reported for different values of the parameters r, that denotes the distance between the inferior joints of wires and the center of their radial distribution, of the number of damper wires n_{dw} and for different diameter of damper wires ϕ_{dw}.

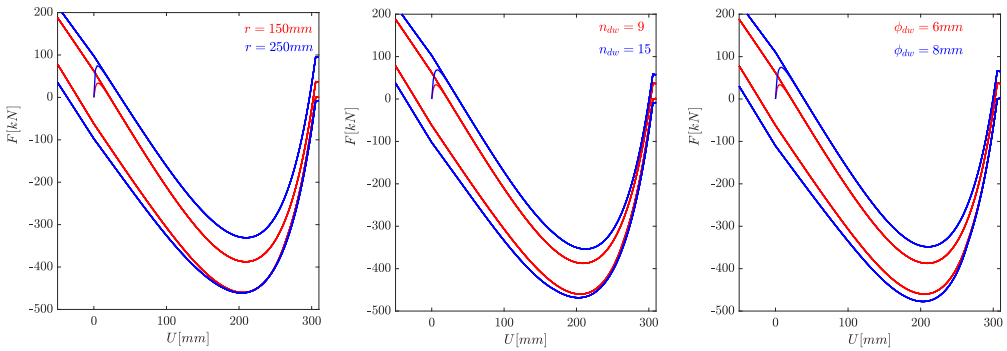

Figure 7.9: Force vs displacement for different r (left), for different number of damper wires n_{dw} (center) and for different diameter of damper wires ϕ_{dw} (right) in the case with steel damper wires.

The introduction of steel damper provides consistent hysteretic damping and an increase in initial stiffness until the yielding of wires. On the other hand, the adoption of damper wires in NiTiNol allows to exploit the superelastic hysteresis provided by the phase transition of the alloy hence to introduce an initial tunable gap region governed by the elastic stiffness of NiTiNol wires.

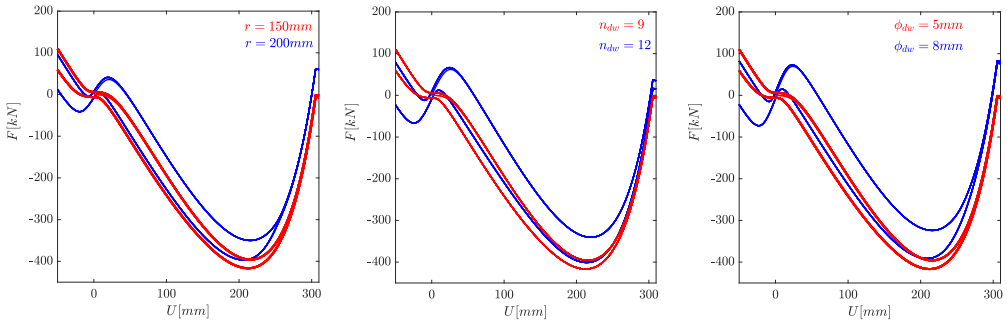

Figure 7.10: Force vs displacement for different r (left), for different number of damper wires n_{dw} (center) and for different diameter of damper wires ϕ_{dw} (right) in the case with steel NiTiNol wires.

In fact, as can be observed in Fig. 7.10, the elastic stiffness of NiTiNol wires balances the negative stiffness until the phase transformation, producing an initial

region where the stiffness of the controlled structure can be maintained unaltered. This can be useful in order to obtain an high stiffness for low displacement and a low stiffness for displacement higher than a threshold value. This initial stiffness, as well as the energy damped by the wires, can be tuned by varying the radial distance of damper wires (r), the number of wires (n_{dw}) and their diameter (ϕ_{dw}).

7.3 Configurations and applications

Depending on the presence or absence of the group of oblique wires (9) and the material constituting these wires, 3 distinct configurations of the device can be identified:

- C1 Wireless configuration;
- C2 Configuration with steel wires;
- C3 Configuration with shape memory alloy wires, i.e. Nickel and Titanium based (NiTiNol), with super-elastic behaviour.

The use of the different configurations makes it possible to achieve different performance requirements depending on the application area of the device. In the C1 configuration the negative stiffness produced by the rod is not balanced by the elastic stiffness of the wires, therefore the global response results with zero stiffness in zero and subsequent increase of the stiffness. This configuration therefore makes it possible to cut the forces entering the system for small and large levels of excitation (Low Static, Low Dynamic stiffness) and also to slow down the structure near the final displacement by calibrating the cubic term of the stiffness (High End Run stiffness). With the C2 and C3 configuration it is possible to obtain a further modulation of the global stiffness thanks to the initial elastic stiffness of the wires. In fact, the global stiffness can be modulated in order to obtain small displacements for small displacement levels and small forces for larger displacements (High Static, Low Dynamic stiffness). In addition, the damper wires assembly provides an additional source of hysteretic damping. The C3 configuration differs from C2 in the use of NiTiNol wires rather than steel and allows an overall Self-Recentering capacity due to the superelastic hysteresis produced by the austenitic-martensitic phase transformation in the wires. The table summarises the performance requirements achievable with the three configurations together with potential applications in mechanical vibration mitigation.

Configuration	Requirements	Applications
C1: wireless	LSs, LDs, HERs	No Constraint for small displacement: Vibration isolation of telescopes, machinery and hospital equipment; vibration damping of flexible structures.
C2: steel wires	HSs, LDs, HERs	Constraint for small displacement: energy damping; seismic isolation of buildings.
C3: NiTiNol wires	HSs, LDs, HERs, SRc	Constraint for small displacement: energy damping; seismic isolation of buildings with re-centering capacity.

Tab.7.1: Requirements achievable and potential applications for the configurations C1, C2 and C3.

7.3.1 Numerical validation on Abaqus

The reliability of the analytical formulation was validated by comparison with the numerical response provided by the three-dimensional nonlinear numerical model of the device developed in the finite element code ABAQUS.

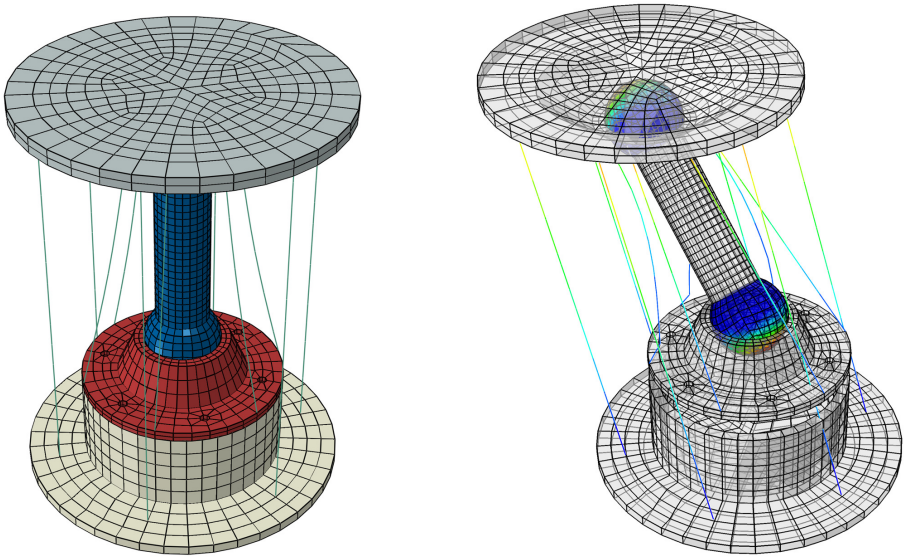

Figure 7.11: Views of the numerical model implemented on ABAQUS.

Figure 7.11 shows a three-dimensional view of the numerical model in the un-

deformed and in the deformed configuration. Since the device is an articulated mechanism and the rheological response is governed by geometric nonlinearities (large displacements) and the behavior of the deformable parts (external ropes, polyurethane spring and damper wires), the two steel caps (1,2) , the rigid rod (4) and the connection plate between rod and spring (7) are modeled as rigid bodies trough the Rigid body constraint. The external ropes (9) and the damper wires (10) are modeled by mean of the T3D2H finite element, that is a 2 node linear 3-D truss with hybrid formulation. The material used for strands is elastic material with steel elastic modulus, while, for the damper wires, the Auricchio model for superelasticity is used for NiTiNol wires and a plastic model is used for steel wires. The spring (8) is modeled as an axial elastic link between the inferior cap (2) and the rod-spring connection plate (7) with stiffness equal to the axial stiffness of the polyurethane spring. The strands are connected to the two rigid caps and the damper wires to the superior cap and the rod-spring connection plate through a translational constraint. The rigid rod interacts with the superior head and with the rod-spring connection plate via a surface to surface contact interaction, where tangential behavior is governed by friction with a Penalty formulation and the normal behavior by a ”hard” contact type of pressure-overclosure rule with allowed separation. The rod-spring connection plate (7) is constrained to move vertically by the presence of linear guides, hence the horizontal translational and the rotational degree of freedom are constrained. Finally, the inferior cap, or the base of device, is fixed to the ground.

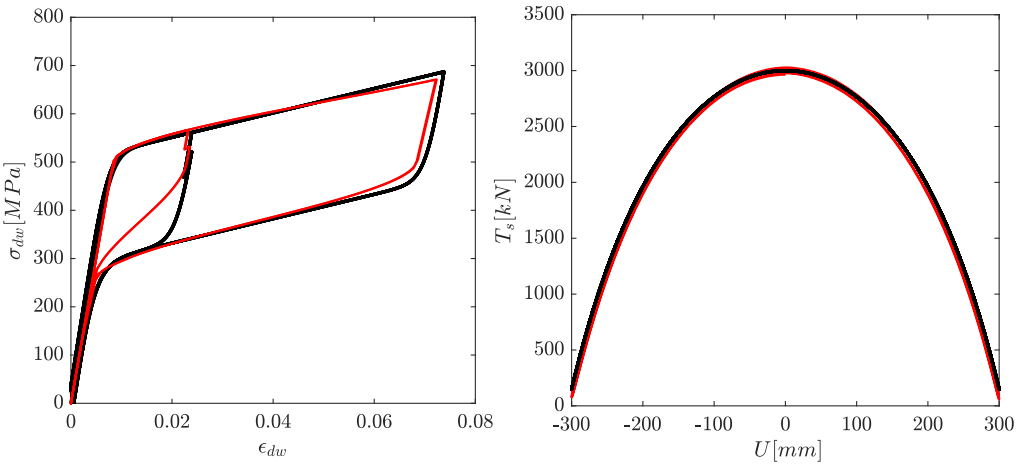

Figure 7.12: Comparison between analytical (black lines) and numerical (red lines) stress-strain response of NiTiNol damper wire (left) and tension force (right) of external strands vs displacement amplitude for the damper subject to static cyclic displacement.

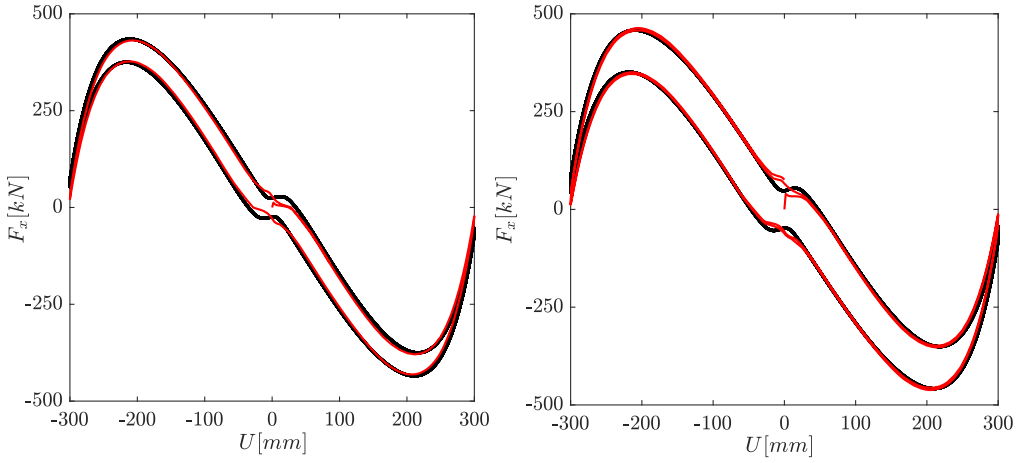

Figure 7.13: Comparison between analytical (black lines) and numerical (red lines) horizontal force-displacement response of the damper subject to static cyclic displacement with friction ratio of the hinges surfaces (μ) set equal to 0.02 (left) and to 0.04 (right).

The pretension of external strands is simulated introducing an initial field in the axial tension of each wires equal to $N_0/(n_s A_s)$, where n_s is the number of external strands and A_s is the cross section area of each strand. In order to obtain the force-displacements cycles of the device a quasi-static sinusoidal displacement history is applied to the superior cap of device, simulating the motion of the controlled structure. Figure 7.12 shows a comparison between the analytical and the numerical response in terms of axial tension in damper wires and axial force in external strands, while in Fig. 7.13 analytical and numerical force-displacement cycles are reported for different friction ratio of the hinges surfaces. From the comparison a fulfilling match between the response predicted with the analytical formulation and the numerical model on Abaqus can be observed and this validates the accuracy of the analytical formulation.

7.4 Conclusions

Starting from the main weaknesses of the existing negative stiffness dampers, i.e. the large size given by the prestressed element, the monodirectional response or the dependence of the response on the weight of the mass to be isolated, a new compact multidirectional damper with super-elastic hysteresis has been designed. The functioning of the mechanism, based not on precompression but on pretensioning of the prestressed element, and the selection of deformable and resistant

materials such as fibre reinforced polymer and polyurethane, allowed the reduction of the size of the device and its multidirectional behaviour. Depending from the material and the presence of the damper wires it is possible to achieve different responses and requirements useful for different applications. The analytical equations of the force-displacement law are derived in function of the geometrical and of the mechanical characteristics of the designed device. Simple laws of the principal features of damper response (K_n, U_{lim} and E_0), useful for design, are obtained and discussed. Finally, analytical derived formulas are validated by comparison with the response provided by a three-dimensional numerical model developed on the software Abaqus.

Chapter 8

Conclusions

A novel high performances vibration isolation system featuring a negative stiffness mechanism and superelastic damping arranged in parallel with classical elastomeric isolation devices is proposed and investigated.
The static characterization of the response of the dimensionless system in terms of stability, stiffness and equivalent damping, has revealed the presence of different types of stability in the ($\tilde{K}_n$, $\tilde{K}_3$, $\tilde{K}_s$) design parameters space and the possibility of obtaining almost zero stiffness together with amplifications of the damping up to over-damped responses.
In order to understand the effects produced by the introduction of NS-SMA damping and its limits an extensive parametric investigation was conducted on the dynamic response of a SDOF isolated mass with NS-SMA damping under harmonic and impulsive excitations. For both excitations, by accurately tuning the negative stiffness with the superelastic damping, a remarkable reduction of displacement and acceleration amplitudes can be achieved, while preserving a self-recentering capability and without incurring an increase of acceleration transmissibility for low excitations.
The study of the nonlinear dynamic response under harmonic excitation and its bifurcations revealed extremely rich bifurcation scenarios with detached resonances and unusual interactions between the primary resonance and superharmonic resonances, or between superharmonic resonances of various orders, featuring multiplicity of coexisiting attractors. The well-trapping phenomenon under impulsive ground motion is showed and its beneficial effect on the control of accelerations under shock excitation are demonstrated and exploited. Analytical formula of optimum parameters combination under a specific pulse amplitude are provided imposing the location of the lateral stable equilibrium equal to the pulse amplitude.
For both types of dynamic excitation, the optimum regions in design parameters space are found using D.E. optimization alghoritm and useful design criteria

for NS-SMA damping are obtaied and illustrated. The optimization of response validate the optimum regions identified in previous chapters and provides useful design hints.
These design criteria have been validated through the study of an example application case, where the dynamic response of a MDOF system, representative of a seismic isolated building, is investigated under seismic excitation. Optimal parameters are found for the NS-SMA damping and for other classic damping techniques (SMAD, HD, VD, FRD, HBD). With the optimized NS-SMA configurations it is possible to achieve a strong reduction in shear forces (70%) with the same maximum displacements of the baseline system, or a significant reduction in shear forces (30%) together with a reduction in displacements (30%). In addition is shown that NS-SMA damping is able to prevents the start of structural damaging retaining the maximum drift values under the limit threshold $Dr = 0.2\%$ for all the limit states investigated (SLO, SLD, SLV, and SLC). This feature results to be not achievable from classic damping techniques studied despite the introduction of large amounts of damping devices and the consequent increase in costs. The illustrated performances, together with the self-recentering capacity of the proposed isolation system, effectively eliminate any potential economic losses induced by seismic risk, thereby confirming the possibility of obtaining a new generation of ideal high-performance seismic isolation systems.
Finally, in order to enable the achievement of the proposed and described rheological response, and starting from the main weaknesses of the existing negative stiffness dampers, i.e. the large size given by the prestressed element, the monodirectional response or the dependence of the response on the weight of the mass to be isolated, a new compact multidirectional damper with negative stiffnes and super-elastic hysteresis has been designed. The functioning of the mechanism and the selection of deformable and resistant materials allowed the reduction of the size of the device and its multidirectional behaviour. Depending from the material and the presence of the damper wires it is possible to achieve different responses and requirements useful for different applications. The analytical equations of the force-displacement law are derived in function of the geometrical and of the mechanical characteristics of the designed device. Simple laws of the principal features of damper response (K_n, U_{lim} and E_0), useful for design, are obtained and discussed. Lastly, the reliability of analytical formulas is validated by comparison with the response provided by a three-dimensional numerical model developed on the software Abaqus.

Bibliography

[1] Soong TT, Spencer BF (2002) Supplemental energy dissipation: State-of-the-art and state-of-the-practice. Eng Struct 24:243–259. https://doi.org/10.1016/S0141-0296(01)00092-X

[2] Weber F, Feltrin G, Huth O (2006) Guidelines for structural control. Struct Eng Res Lab Swiss Fed Lab Mater Test Res Dubendorf, Switz 1–155

[3] Cheng (2008) Smart structures (passive,semi-active and active control). https://doi.org/10.1201/9781420008173

[4] Chopra I (2012) Review of state of art of smart structures and integrated systems. AIAA J 40:2145–2187. https://doi.org/10.2514/3.15309

[5] Lu Z, Wang Z, Zhou Y, Lu X (2018) Nonlinear dissipative devices in structural vibration control: A review. J Sound Vib 423:18–49. https://doi.org/10.1016/j.jsv.2018.02.052

[6] Li Z, Adeli H (2018) Control methodologies for vibration control of smart civil and mechanical structures. Expert Syst 35:1–20. https://doi.org/10.1111/exsy.12354

[7] Constantinou MC (1986) Optimum characteristics of isolated structures. J Struct Eng 111:12 https://doi.org/10.1061/(ASCE)0733-9445(1985)111:12(2733)

[8] Kelly JM (1990) Base Isolation Linear theory and design. https://doi.org/10.1193/1.1585566

[9] Inaudi JA, Kelly JM (1993) Optimum damping in linear isolation systems. Earthq Eng Struct Dyn 22:583–598. https://doi.org/10.1002/eqe.4290220704

[10] Jangid RS (1996) Optimum damping in a non-linear base isolation system. J Sound Vib 189:477–487. https://doi.org/10.1006/jsvi.1996.0030

[11] Nayfeh TA, Emaci E, Vakakis AF (1997) Application of nonlinear localization to the optimization of a vibration isolation system. AIAA J 35:1378–1386. https://doi.org/10.2514/2.247

[12] Jangid RS (1998) Effects of isolation damping on Stochastic Response of Structure. Earthq Spectra 14:1. https://doi.org/10.1193/1.1585990

[13] Makris N, Chang SP (2000) Effect of viscous, viscoplastic and friction damping on the response of seismic isolated structures. Earthq Eng Struct Dyn 29:85–107. https://doi.org/10.1002/(SICI)1096-9845(200001)29

[14] Jangid RS, Kelly JM (2001) Base isolation for near-fault motions. Earthq Eng Struct Dyn 30:691–707. https://doi.org/10.1002/eqe.31

[15] Jangid RS (2002) Parametric Study of Base-Isolated Structures. Adv STruct Eng 5:113–122. https://doi.org/10.1260/1369433021502605

[16] Ramallo JC, Johnson EA, Spencer BF (2002) "Smart" base isolation systems. J Eng Mech 128:1088–1100. https://doi.org/10.1061/(ASCE)0733-9399(2002)128:10(1088)

[17] Matsagar VA, Jangid RS (2004) Influence of isolator characteristics on the response of base-isolated structures. Eng Struct 26:1735–1749. https://doi.org/10.1016/j.engstruct.2004.060.011

[18] Alhan C, Gavin H (2004) A parametric study of linear and non-linear passively damped seismic isolation systems for buildings. Eng Struct 26:485–497. https://doi.org/10.1016/j.engstruct.2003.11.004

[19] Baratta A, Corbi I (2004) Optimal design of base-isolators in multi-storey buildings. Comput Struct 82:2199–2209. https://doi.org/10.1016/j.compstruc.2004.03.061

[20] Jangid RS (2007) Optimum lead-rubber isolation bearings for near-fault motions. Eng Struct 29:2503–2513. https://doi.org/10.1016/j.engstruct.2006.12.010

[21] Ibrahim R.a. (2008) Recent advances in nonlinear passive vibration isolators. J Sound Vib 314:371–452. https://doi.org/10.1016/j.jsv.2008.01.014

[22] Bucher C (2009) Probability-based optimal design of friction-based seismic isolation devices. Struct Saf 31:500–507. https://doi.org/10.1016/j.strusafe.2009.06.009

[23] Mazza F, Vulcano A (2009) Nonlinear response of RC framed buildings with isolation and supplemental damping at the base subjected to near-fault earthquakes. J Earthq Eng 13:690–715. https://doi.org/10.1080/13632460802632302

[24] Fallah N, Zamiri G (2013) Multi-objective optimal design of sliding base isolation using genetic algorithm. Sci Iran 20:87–96. https://doi.org/10.1016/j.scient.2012.11.004

[25] Nigdeli SM, Bekdaş G, Alhan C (2014) Optimization of seismic isolation systems via harmony search. Eng Optim 46:1553–1569. https://doi.org/10.1080/0305215X.2013.854352

[26] Barakat SA, Alhamaydeh MH, Nassif OM, et al (2015) Optimization of seismic isolation systems with viscous fluid dampers using genetic algorithms. COMPDYN 2015

[27] Roy BK, Chakraborty S (2015) Robust optimum design of base isolation system in seismic vibration control of structures under random system parameters. Struct Saf 55:49–59. https://doi.org/10.1016/j.strusafe.2015.02.005

[28] Greco R, Marano GC (2016) Robust optimization of base isolation devices under uncertain parameters. JVC/Journal Vib Control 22:853–868. https://doi.org/10.1177/1077546314532670

[29] Yazhou X, Jian Z (2017) Optimal Design of Seismic Protective Devices for Highway Bridges Using Performance-Based Methodology and Multiobjective Genetic Optimization. J Bridg Eng 22:4016129. https://doi.org/10.1061/(ASCE)BE.1943-5592.0001009

[30] Tsai HC (1995) The effect of tuned-mass dampers on the seismic response of base-isolated structures. Int J Solids Struct 32:1195–1210. https://doi.org/10.1016/0020-7683(94)00150-U

[31] Zhang Y, Iwan WD (2002) Protecting base-isolated structures from near-field ground motion by tuned interaction damper. J Eng Mech 128:287–295. https://doi.org/10.1061/(ASCE)0733-9399(2002)128:3(287)

[32] Smith MC (2002) Synthesis of mechanical networks: The inerter. Proc IEEE Conf Decis Control 2:1657–1662. https://doi.org/10.1109/TAC.2002.803532

[33] Saito K, Yogo K, Sugimura Y, et al (2004) Application of Rotary Inertia To Displacement Reduction for Vibration Control System. 13th World Conf Earthq Eng

[34] Georgiadis F, Vakakis AF, McFarland DM, Bergman LA (2005) Shock Isolation Through Passive Energy Pumping Caused By Nonsmooth Nonlinearities. Int J Bifurc Chaos 15:1989–2001. https://doi.org/10.1142/s0218127405013101

[35] Nucera F, Vakakis AF, McFarland DM, et al (2007) Targeted energy transfers in vibro-impact oscillators for seismic mitigation. Nonlinear Dyn 50:651–677. https://doi.org/10.1007/s11071-006-9189-7

[36] Gourdon E, Alexander NA, Taylor CA, et al (2007) Nonlinear energy pumping under transient forcing with strongly nonlinear coupling: Theoretical and experimental results. J Sound Vib 300:522–551. https://doi.org/10.1016/j.jsv.2006.06.074

[37] Taniguchi T, Der Kiureghian A, Melkumyan M (2008) Effect of tuned mass damper on displacement demand of base-isolated structures. Eng Struct 30:3478–3488. https://doi.org/10.1016/j.engstruct.2008.05.027

[38] Quinn DD, Gendelman O V., Kerschen G, et al (2008) Efficiency of targeted energy transfers in coupled nonlinear oscillators associated with 1:1 resonance captures: Part I. J Sound Vib 311:1228–1248. https://doi.org/10.1016/j.jsv.2007.10.026

[39] Sapsis TP, Vakakis AF, Gendelman O V., et al (2009) Efficiency of targeted energy transfers in coupled nonlinear oscillators associated with 1:1 resonance captures: Part II, analyti

[40] Lee YS, Nucera F, Vakakis AF, et al (2009) Periodic orbits, damped transitions and targeted energy transfers in oscillators with vibro-impact attachments. Phys D Nonlinear Phenom 23 cal study. J Sound Vib 325:297–320. https://doi.org/10.1016/j.jsv.2009.03.0048:1868–1896. https://doi.org/10.1016/j.physd.2009.06.013

[41] Wierschem NE, Spencer Jr BF, Bergman LA, Vakakis AF (2011) Numerical study of nonlinear energy sinks for seismic response reduction. Proc 6th Int Work Adv Smart Mater Smart Struct Technol

[42] Sigalov G, Gendelman O V., AL-Shudeifat MA, et al (2012) Resonance captures and targeted energy transfers in an inertially-coupled rotational nonlinear energy sink. Nonlinear Dyn 69:1693–1704. https://doi.org/10.1007/s11071-012-0379-1

[43] AL-Shudeifat MA (2014) Highly efficient nonlinear energy sink. Nonlinear Dyn. 76:1905–1920. https://doi.org/10.1007/s11071-014-1256-x

[44] Chen Z, Junya K, Masahiro I, et al (2016) Viscoelastically Supported Viscous Mass Damper Incorporated into a Seismic Isolation System. Earthq Tsunami 10:1–15. https://doi.org/10.1142/S1793431116400091

[45] Boroson E, Missoum S, Mattei PO, Vergez C (2017) Optimization under uncertainty of parallel nonlinear energy sinks. J Sound Vib 394:451–464. https://doi.org/10.1016/j.jsv.2016.12.043

[46] De Domenico D, Ricciardi G (2018) An enhanced base isolation system equipped with optimal tuned mass damper inerter (TMDI). Earthq Eng Struct Dyn 47:1169–1192. https://doi.org/10.1002/eqe.3011

[47] Tsiatas GC, Charalampakis AE (2018) A new Hysteretic Nonlinear Energy Sink (HNES). Commun Nonlinear Sci Numer Simul 60:1–11. https://doi.org/10.1016/j.cnsns.2017.12.014

[48] Qian F, Luo Y, Sun H, et al (2019) Optimal tuned inerter dampers for performance enhancement of vibration isolation. Eng Struct 198:109464. https://doi.org/10.1016/j.engstruct.2019.109464

[49] De Angelis M, Giaralis A, Petrini F, Pietrosanti D (2019) Optimal tuning and assessment of inertial dampers with grounded inerter for vibration control of seismically excited base-isolated systems. Eng Struct 196. https://doi.org/10.1016/j.engstruct.2019.05.091

[50] Kam WY, Pampanin S, Carr AJ (2007) Advanced Flag-Shape Systems for High Seismic Performance including Near-fault Effects. 2007 NZSEE Conf 1–9

[51] Kam WY, Pampanin S, Palermo A, Carr AJ (2008) Design procedure and behaviour of Advanced Flag-Shape (AFS) MDOF systems. 2008 NZSEE 1–18

[52] Whittaker A, Krumme R, Sweeney SC, Hayes JR (1995) Structural control of building response using shape memory alloy. doi:10.13140/RG.2.1.3814.6168

[53] Dolce M, Cardone D, Marnetto R (2000) Implementation and testing of passive control devices based on shape memory alloys. Earthq Eng Struct Dyn 29:945–968. https://doi.org/10.1002/1096-9845(200007)29:7<945: AID-EQE958>3.0.CO

[54] Saadat S, Salichs J, Noori M, et al (2002) An overview of vibration and seismic applications of NiTi shape memory alloy. Smart Mater Struct 11:218–229. https://doi.org/10.1088/0964-1726/11/2/305

[55] Desroches R, Smith B (2004) Shape memory alloys in seismic resistant design and retrofit: A critical review of their potential and limitations. J Earthq Eng 8:415–429. https://doi.org/10.1142/S1363246904001298

[56] Desroches R (2004) Cyclic Properties of Superelastic Shape Memory Alloy Wires and Bars. J Struct Eng https://doi.org/10.1061/(ASCE)0733-9445(2004)130

[57] Zuo XB, Chang W, Li AQ, Chen QF (2006) Design and experimental investigation of a superelastic SMA damper. Mater Sci Eng A 438–440:1150–1153. https://doi.org/10.1016/j.msea.2006.02.147

[58] Song G, Ma N, Li HN (2006) Applications of shape memory alloys in civil structures. Eng Struct 28:1266–1274. https://doi.org/10.1016/j.engstruct.2005.12.010

[59] Cardone D, Dolce M, Ponzo F (2006) The behaviour of sma isolation systems based on a full-scale release test. J Earthq Eng 10:815–842. https://doi.org/10.1080/13632460609350619

[60] Speicher M, Hodgson DE, Desroches R, Leon RT (2009) Shape memory alloy tension/compression device for seismic retrofit of buildings. J Mater Eng Perform 18:746–753

[61] Ozbulut O, Hurlebaus S (2010) Optimal design of superelastic-friction base isolators for seismic protection of highway bridges against near-field earthquakes. Earthq Eng Struct Dyn 679–698. https://doi.org/10.1002/eqe

[62] Filiatrault A (2010) Performance evaluation of Friction Spring seismic Damper. J Earthq Eng 2:64–73 https://doi.org/10.1061/(ASCE)0733-9445(2000)126:4(491)

[63] Ozbulut OE, Hurlebaus S, Desroches R (2011) Seismic response control using shape memory alloys: A review. J Intell Mater Syst Struct 22:1531–1549

[64] Jalali A, Cardone D, Narjabadifam P (2011) Smart restorable sliding base isolation system. Bull Earthq Eng 9:657–673. https://doi.org/10.1007/s10518-010-9213-7

[65] Cardone D (2012) Re-centring capability of flag-shaped seismic isolation systems. Bull Earthq Eng 10:1267–1284

[66] Alvandi S, Ghassemieh M (2014) Application of Shape Memory Alloys in Seismic Isolation: A Review Application of Shape Memory Alloys in Seismic Isolation: A Review. Civ Eng J https://doi.org/10.7508/ceij.2014.02.001

[67] Gur S, Mishra S (2014) Stochastic optimization of shape-memory-alloy rubber bearing (SMARB) for isolating buildings against random earthquake. Struct Health Monit 10.7508/CEIJ.2014.02.001

[68] Soul H, Yawny A (2015) Self-centering and damping capabilities of a tension-compression device equipped with superelastic NiTi wires. Smart Mater Struct 24: https://doi.org/10.1088/0964-1726/24/7/075005

[69] Ozbulut O, Silwal B (2016) Performance assessment of buildings isolated with S-FBI system under near-fault earthquakes. Smart Struct Syst 17:709–724. https://doi.org/10.12989/sss.2016.17.5.709

[70] Soul H, Yawny A (2017) Applicability of superelastic materials in seismic protection systems: A parametric study of performance in isolation of structures. Smart Mater Struct 26: https://doi.org/10.1088/1361-665X/aa7caf

[71] Wang J quan, Li S, Hedayati Dezfuli F, Alam MS (2019) Sensitivity analysis and multi-criteria optimization of SMA cable restrainers for longitudinal seismic protection of isolated simply supported highway bridges. Eng Struct 189:509–522. https://doi.org/10.1016/j.engstruct.2019.03.091

[72] Platus DL (1992) Negative stiffness mechanism vibration isolation systems. 1619:44–54 SPIE TECHNICAL: OPTCON '91/1-30 NOVEMBER 1991 https://doi.org/10.1117/12.56823

[73] Platus DL (1999) Negative stiffness mechanism vibration isolation systems I. 3786:98–105. https://doi.org/10.1117/12.363841

[74] Wang Y-C, Lakes R (2004) Stability of negative stiffness viscoelastic systems. Q Appl Math 63:34–55. https://doi.org/10.1090/s0033-569x-04-00938-6

[75] Park S, Luu T (2007) Techniques for optimizing parameters of negative stiffness. 221:505–512. https://doi.org/10.1243/0954406JMES390

[76] DeSalvo R (2007) Passive, Nonlinear, Mechanical Structures for Seismic Attenuation. J Comput Nonlinear Dyn 2:290. https://doi.org/10.1115/1.2754305

[77] Dyskin A V., Pasternak E (2014) Negative stiffness: Is thermodynamics defeated? In: 8th Australasian Congress on Applied Mechanics, ACAM 2014. pp 897–903

[78] Antoniadis I, Chronopoulos D, Spitas V, Koulocheris D (2015) Hyper-damping properties of a stiff and stable linear oscillator with a negative stiffness element. J Sound Vib 346:37–52. https://doi.org/10.1016/j.jsv.2015.02.028

[79] Mathew GM, Qureshi A, Jangid RS (2016) Optimal Placement of Negative Stiffness Damping System. ASME 2015. https://doi.org/10.1115/SMASIS2015-9002

[80] Charalampakis AE, Tsiatas GC (2018) Effects of Hysteresis and Negative Stiffness on Seismic Response Reduction: A Case Study Based on the 1999 Athens, Greece Earthquake. Front Built Environ 4: https://doi.org/10.3389/fbuil.2018.00023

[81] Wang M, Sun F fei, Yang J qi, Nagarajaiah S (2019) Seismic protection of SDOF systems with a negative stiffness amplifying damper. Eng Struct 190:128–141. https://doi.org/10.1016/j.engstruct.2019.03.110

[82] Iemura H (2003) Application of pseudo-negative stiffness control to the benchmark bridge. J Struct Contr 10:187-203. https://doi.org/10.1002/stc.25

[83] Iemura H (2006) Negative stiffness friction damping for seismically. SCHM 13:775-791. https://doi.org/10.1002/stc.111

[84] Iemura H, Kouchiyama O, Toyooka A, Shimoda I (2008) Development of the Friction-Based Passive Negative Stiffness Damper and Its Verification Tests Using Shaking Table. Proc 14th World Conf Earthq Eng 12:01–0219

[85] Iemura H, Pradono MH (2010) Advances in the development of pseudo-negative-stiffness dampers for seismic response control. Struct Control Heal Monit 742–760. https://doi.org/10.1002/stc

[86] Pradono MH, Iemura H (2010) Passively controlled MR damper in the benchmark structural control problem for seismically excited highway bridge. Struct Control Heal Monit 742–760. https://doi.org/10.1002/stc

[87] Madhekar SN, Jangid RS (2012) Use of pseudo-negative stiffness dampers for reducing the seismic response of bridges: A benchmark study. Bull Earthq Eng 10:1561–1583. https://doi.org/10.1007/s10518-012-9357-8

[88] Tan X, Wang B, Chen S, et al (2019) A novel cylindrical negative stiffness structure for shock isolation. Compos Struct 214:397–405. https://doi.org/10.1016/j.compstruct.2019.02.030

[89] Reinhorn AM, Viti S, Cimellaro G (2005) Retrofit of Structures: Strength Reduction with Damping Enhancement. In: 37th UJNR panel meeting on wind and seismic effects. pp 16–21

[90] Pasala DTR, Sarlis AA, Nagarajaiah S, et al (2012) Negative stiffness device for seismic response control of multistory buildings. In: 20th Analysis and Computation Specialty Conference - Proceedings of the Conference. pp 83–96

[91] Taylor D, Nagarajaiah S, Reinhorn AM, et al (2013) Adaptive negative stiffness: A new structural modification approach for seismic protection. J Struct Eng 139:1–15. https://doi.org/10.1061/(ASCE)ST.1943-541X.0000615

[92] Sarlis AA, Pasala DTR, Constantinou MC, et al (2013) Negative stiffness device for seismic protection of structures. J Struct Eng 139:1124–1133. https://doi.org/10.1061/(ASCE)ST.1943-541X.0000616

[93] Pasala DTR, Sarlis AA, Reinhorn AM, et al (2014) Simulated bilinear-elastic behavior in a SDOF elastic structure using negative stiffness device: Experimental and analytical study. J Struct Eng 140:1–13. https://doi.org/10.1061/(ASCE)ST.1943-541X.0000830

[94] Attary N, Symans M, Nagarajaiah S, et al (2015) Experimental shake table testing of an adaptive passive negative stiffness device within a highway bridge model. Earthq Spectra 31:2163–2194. https://doi.org/10.1193/101913EQS273M

[95] Sarlis AA, Pasala DTR, Constantinou MC, et al (2016) Negative Stiffness Device for Seismic Protection of Structures: Shake Table Testing of a Seismically Isolated Structure. J Struct Eng 142:1–13. https://doi.org/10.1061/(ASCE)ST.1943-541X.0001455

[96] Attary N, Symans M, Nagarajaiah S (2017) Development of a rotation-based negative stiffness device for seismic protection of structures. J Vib Control 23:853–867. https://doi.org/10.1177/1077546315585435

[97] Sun T, Lai Z, Zhang Y, Li H (2018) Application of a negative stiffness device in the benchmark problem for a highway bridge. Structures18)

[98] Winterflood J, Blair DG, Slagmolen B (2002) High performance vibration isolation using springs in Euler column buckling mode. Phy Letter 300:122–130. https://doi.org/10.1016/S0375-9601(02)00258-X

[99] Alhan C, Gavin HP, Aldemir U (2006) Optimal control: Basis for performance comparison of passive and semiactive isolation systems. J Eng Mech 132:705–713. https://doi.org/10.1061/(ASCE)0733-9399(2006)132:7(705)

[100] Carrella A, Brennan MJ, Waters TP (2007) Static analysis of a passive vibration isolator with quasi-zero-stiffness characteristic. J Sound Vib 301:678-689. https://doi.org/10.1016/j.jsv.2006.10.011

[101] Kovacic I, Brennan MJ, Waters TP (2008) A study of a nonlinear vibration isolator with a quasi-zero stiffness characteristic. J Sound Vib 315:700-711. https://doi.org/10.1016/j.jsv.2007.12.019

[102] Zhou N, Liu K (2010) A tunable high-static-low-dynamic stiffness vibration isolator. J Sound Vib 329:1254-1273. doi: 10.1016/j.jsv.2009.11.001

[103] Le TD, Ahn KK (2011) A vibration isolation system in low frequency excitation region using negative stiffness structure for vehicle seat. J Sound Vib 330:6311-6335. https://doi.org/10.1016/j.jsv.2011.07.039

[104] Carrella A, Brennan MJ, Waters TP, Lopes V (2012) Force and displacement transmissibility of a nonlinear isolator with high-static-low-dynamic-stiffness. Int J Mech Sciences 55: 22-29. https://doi.org/10.1016/j.ijmecsci.2011.11.012

[105] Yang J, Xiong YP, Xing JT (2013) Dynamics and power flow behaviour of a nonlinear vibration isolation system with a negative stiffness mechanism. J Sound Vib 332: 167-183. https://doi.org/10.1016/j.jsv.2012.08.010

[106] Huang X, Liu X, Sun J, et al (2014) Vibration isolation characteristics of a nonlinear isolator using euler buckled beam as negative stiffness corrector: A theoretical and experimental study. J Sound Vib 333: 1132-1148. https://doi.org/10.1016/j.jsv.2013.10.026

[107] Hao Z, Cao Q (2015) The isolation characteristics of an archetypal dynamical model with stable-quasi-zero-stiffness. J Sound Vib 340:61-79. https://doi.org/10.1016/j.jsv.2014.11.038

[108] Zheng Y, Zhang X, Luo Y, et al (2016) Design and experiment of a high-static-low-dynamic stiffness isolator using a negative stiffness magnetic spring. J Sound Vib 360:31-52. https://doi.org/10.1016/j.jsv.2015.09.019

[109] Lu ZQ, Brennan M, Ding H, Chen LQ (2018) High-static-low-dynamic-stiffness vibration isolation enhanced by damping nonlinearity. Science China Technological Sciences 62: 1103-1110. https://doi.org/10.1007/s11431-017-9281-9

[110] Cimellaro GP, Domaneschi M, Warn G (2018) Three-Dimensional Base Isolation Using Vertical Negative Stiffness Devices. J Earthq Eng 24:2004-2032. https://doi.org/10.1080/13632469.2018.1493004

[111] Wang X, Liu H, Chen Y, Gao P (2018) Beneficial stiffness design of a high-static-low-dynamic-stiffness vibration isolator based on

static and dynamic analysis. Int J Mech Sciences 142: 235-244. https://doi.org/10.1016/j.ijmecsci.2018.04.053

[112] Zhou Y, Chen P, Mosqueda G (2019) Analytical and Numerical Investigation of Quasi-Zero Stiffness Vertical Isolation System. J Eng Mech 145. https://doi.org/10.1061/(ASCE)EM.1943-7889.0001611

[113] Sun M, Song G, Li Y, Huang Z (2019) Effect of negative stiffness mechanism in a vibration isolator with asymmetric and high-static-low-dynamic stiffness. Mech Syst Sign Processing 124:388-407. https://ui.adsabs.harvard.edu/abs/2019MSSP..124..388S

[114] Shi X, Zhu S (2019) A comparative study of vibration isolation performance using negative stiffness and inerter dampers. J Franklin Inst 356:7922-7946. https://doi.org/10.1016/j.jfranklin.2019.02.040

[115] Yan B, Ma H, Jian B, Wang K, Wu C (2019) Nonlinear dynamics analysis of a bi-state nonlinear vibration isolator with symmetric permanent magnets. Non Dyn 97:2499-2519. https://doi.org/10.1007/s11071-019-05144-w

[116] Bian J, Jing X (2020) Analysis and design of a novel and compact X-structured vibration isolation mount (X-Mount) with wider quasi-zero-stiffness range. Non Dyn 101:2195-2222. https://doi.org/10.1007/s11071-020-05878-y

[117] Gao X, Teng HD (2020) Dynamics and isolation properties for a pneumatic near-zero frequency vibration isolator with nonlinear stiffness and damping. Non Dyn 102: 2205-2227. https://doi.org/10.1007/s11071-020-06063-x

[118] Liu C, Yu K (2020) Accurate modeling and analysis of a typical nonlinear vibration isolator with quasi-zero stiffness. Non Dyn 100:2141-2165. https://doi.org/10.1007/s11071-020-05642-2

[119] Sonfack Bouna H, Nana Nbendjo BR, Woafo P (2020) Isolation performance of a quasi-zero stiffness isolator in vibration isolation of a multi-span continuous beam bridge under pier base vibrating excitation. Non Dyn 100:1125-1141. https://doi.org/10.1007/s11071-020-05580-z

[120] Wang K, Zhou J, Chang Y, Ouyang H, Xu D (2020) A nonlinear ultra-low-frequency vibration isolator with dual quasi-zero-stiffness mechanism. Non Dyn 101:755-773. https://doi.org/10.1007/s11071-020-05806-0

[121] Donmez A, Cigeroglu E, Ozgen OG (2020) An improved quasi-zero stiffness vibration isolation system utilizing dry friction damping. Non Dyn 101:107-121. https://doi.org/10.1007/s11071-020-05685-5

[122] Liu M, Zhou P, Li H (2018) Novel Self-Centering Negative Stiffness Damper Based on Combination of Shape Memory Alloy and Prepressed Springs. J Aerospace Eng 31. https://doi.org/10.1061/(ASCE)AS.1943-5525.0000926

[123] Platus, D. L. (1993). Vibration isolation system. US5310157A

[124] Avshalom Suissa (2013). Method and apparatus for suspension damping including negative stiffness.

[125] Zhou Peng (2017). The adjustable passive negative stiffness damper of series mechanism. China CN106836543A.

[126] Ma Yuhong (2020). Shape memory alloy negative stiffness damping device. China CN111119366A

[127] Michael Constantinou (2012). Negative stiffness device and method. United States US8857110B2

[128] Hanoi Sanxiu (2006). Negative rigid device and vibration isolation structure having the negative rigid device. China CN101351601B.

[129] Hirozaki Iemura (2013). Negative rigidity damper. Japan JP6304933B2.

[130] Cao Sa Sa (2019). A kind of SMA negative stiffness damping device. China CN110397175A

[131] Bouc R (1967) Forced vibration of mechanical systems with hysteresis. Materials Science.

[132] Wen Y (1976) Method for random vibration of hysteretic Systems. J Eng Mech Div 102:249-263.

[133] Charalampakis AE, Tsiatas GC (2018) A Simple Rate-Independent Uniaxial Shape Memory Alloy (SMA) Model. Frontiers in Built Environment 4. https://doi.org/10.3389/fbuil.2018.00046

[134] Lacarbonara W, Vestroni F, and Capecchi D (1999) Poincarè map-based continuation of periodic orbits in dynamic discontinuous and hysteretic systems. 17th Biennial ASME Conference on Mechanical Vibration and Noise. Poincarè map-based continuation of periodic orbits in dynamic discontinuous and hysteretic systems

[135] Habib G, Cirillo GI, Kerschenc G (2017) Uncovering detached resonance curves in single-degree-of-freedom systems. Procedia Engineering 199:649-656. https://doi.org/10.1016/j.proeng.2017.09.116

[136] Gatti G, Brennan MJ, Kovacic I (2016) On the interaction of the responses at the resonance frequencies of a nonlinear two degrees-of-freedom system. Physica D: Nonlinear Phenomena 239:591-599. https://doi.org/10.1016/j.physd.2010.01.006

[137] Formica G, Lacarbonara W (2020) Asymptotic dynamic modeling and response of hysteretic nanostructured beams. Non Dyn 99:227-248. https://doi.org/10.1007/s11071-019-05386-8

List of Figures